Experimental Investigation of the flow over macroscopic hexagonal structured surfaces

Von der Fakultät für Maschinenbau, Elektrotechnik und Wirtschaftsingenieurwesen
der Brandenburgischen Technischen Universität Cottbus-Senftenberg zur Erlangung
des akademischen Grades eines Doktor-Ingenieurs
genehmigte Dissertation

vorgelegt von

M.Sc.
Usman Butt

Geboren am 10.02.1985 in Lahore, Pakistan

Vorsitzender: Prof. Dr.-Ing. Vesselin Michailov

Gutachter: Prof. Dr.-Ing. Christoph Egbers

Gutachter: Prof. Dr.-Ing. Ennes Sarradj

Tag der mündlichen Prüfung: 09. April 2014

TABLE OF CONTENTS

Abstract

The flow over macroscopic patterned/structured surfaces was investigated in a subsonic wind tunnel over Reynolds numbers ranging from 3.14 x 10^4 to 2.77 x 10^5 for cylinders and from 5.34 x 10^5 to 11.27 x 10^6 for plates. The investigations were accomplished by measuring local and global drag, velocity profiles and by visualization of the flow above the surface. The investigations on structured cylinders revealed that a cylinder with outwardly curved structures has a drag coefficient of about 0.65 times of a smooth one. Flow visualization was carried out by using oil-film technique and velocity profile measurements to elucidate the observed effect, and hence present the mechanism responsible for the observed drag reduction. The near-wall velocity profiles above the surface revealed that a hexagonal bump induces local separation generating large turbulence intensity along the separating shear layer. Due to this increased turbulence, the flow reattaches to the surface with a higher momentum and become able to withstand the pressure gradient delaying the main separation significantly. Besides that, the separation does not appear to occur in a straight line along the length of the cylinder, but follow the curved path forming a wave with its crest at 115° and trough at 110°, in contrast to the laminar separation line at 85° on a smooth cylinder. Investigations on structured plates were performed with the help of hot wire anemometry and oil film interferometry. The main concern of the experiments on structured plates was to examine the effect of hexagonal structures on local and global drag of a structured plate. It was accomplished by determining and analyzing the boundary layer quantities like shear stress velocities, shear stress coefficients and momentum thicknesses over a selected Reynolds number range and various locations in streamwise direction. The results indicate that the values of shear stress coefficients measured by the conventional Clauser chart method are up to 13% higher than the ones deduced by the Oil film Interferometry. Additionally, a maximum of 19% reduction in shear stress coefficient behind the inwardly curved structured plate was observed. On the other hand, a dramatic increase of about 120% in global drag coefficient supersedes the observed reduction in shear stresses at rear of the test plates. Investigations on individual hexagonal structures by measuring the shear stresses and the pressure distribution above the surface revealed that an uneven pressure distribution contributing in total drag force is responsible for a huge increase in global skin drag coefficient. Finally, a number of configurations of a wind turbine made of smooth and structured blades were investigated to compare their efficiencies at various flow velocities. No significant deviation in the efficiencies was observed.

Key words: Aerodynamics, Oil film Interferometry, Drag reduction, Hot wire Anemometry

Kurzfassung

Im Rahmen dieser Arbeit, wurde die Strömung über makroskopisch strukturierten Oberflächen in einem Unterschall-Windkanal untersucht. Die Untersuchungen erfolgten bei Reynolds-Zahlen von 3.14×10^4 bis 2.77×10^5 für Zylinder und von 5.34×10^5 bis 11.27×10^6 für Platten. Weiterhin wurden Messungen lokaler und globaler Widerstände, von Strömungsvisualisierungen und Geschwindigkeitsprofilen durchgeführt. Das Ziel der Untersuchungen an Zylindern war, den Einfluss dieser Strukturen auf die Strömungsgrössen wie Druckwiderstand und Wirbelablösefrequenzen zu ermitteln. Die Untersuchungen zeigten, dass der strukturierte Zylinder mit nach außen gewölbten Strukturen einen Widerstandkoeffizient mit einem Faktor von 0,65 dem eines glatten Zylinders aufweist. Messungen wurden durchgeführt mit der Öl-film Methode und der Hitzdraht Anemometrie. Die Geschwindigkeitsprofile in der Nähe der Wand zeigten, dass eine Hexagonal Struktur eine lokale Ablösung verursacht und dadurch die Turbulenz in der Grenzschicht erhöht. Aufgrund des erhöhten Turbulenzgrades legt sich die Strömung mit einem höheren Impuls an die Oberfläche an und ist somit fähig einen negativen Druckgradienten zu überstehen. Als Folge ist die Hauptablösung deutlich verzögert. Außerdem findet die Ablösung nicht linear und senkrecht zur Strömung statt, sondern in Form einer Welle mit ihrem Maximum bei 115° und Minimum bei 110°. Dies steht im Gegensatz zu der laminaren Ablöselinie bei 85° für glatte Zylinder. Die strukturierten Platten wurden ebenfalls mit der Hitzdraht Anemometrie und der Öl-Film Interferometry untersucht. Das Ziel bei diesen Untersuchungen war es den Einfluss von hexagonalen Strukturen auf den lokalen und globalen Widerstand einer strukturierten Platte zu ermitteln. Über die Clauser-Chart methode bestimmte Scherspannungen sind etwa 13% höher als die mit der Öl-Film Interferometry ermittelten Werte. Zudem wurde eine Minderung von ca. 19% der Scherspannung hinter einer strukturierten Platte festgestellt. Der globale Widerstand der gesamten Platte steigt gleichzeitig dramatisch um 120%. Durch Messen der Scherspannung und der Druckverteilung über den individuellen Strukturen ist festgestellt worden, dass die unregelmäßige Druckverteilung einen zusätzlichen Druckwiderstand erzeugt und für die enorme Vergrößerung des globalen Widerstandes verantwortlich ist. Letztendlich, wurde eine Vielzahl an Konfigurationen einer aus flachen als auch strukturierten Schaufeln gefertigten Windturbine bei unterschiedlichen Strömungsgeschwindigkeiten untersucht. Es konnte keine deutliche Änderung im Wirkungsgrad der Turbine aus strukturierten Schaufeln festgestellt werden.

Schlagwörter: Aerodynamik, Öl film Interferometrie, Widerstandsreduzierung, Hitz-draht Anemometrie

Symbols & Abbreviations

τ_w	Shear stress
u_τ	shear stress velocity
κ	Von Ka’rma’n constant
ρ	Density of the fluid
B	logarithmic law constant
ν	Kinematic viscosity
y	Vertical distance
u	Instantaneous velocity
U_∞	Free stream Velocity
C_f	Shear stress coefficient (local skin drag coefficient)
R	Drag force
C_F	Global drag coefficient of a plate
C_d	Drag coefficient of a cylinder
p	Local pressure
p_0	Pressure in undisturbed medium
b	Width of the plate
l	length of the plate
δ	Boundary layer thickness
δ_1	Displacement thickness
δ_2	Momentum thickness
x	Horizontal distance
Re	Diameter based Reynolds number
D	Diameter of the cylinder
y^+	Dimensionless vertical distance
u^+	Dimensionless velocity
Re_δ	Reynolds number based on boundary layer thickness
v	Instantaneous velocity
θ	Angle of incidence of the turbine blade
v_r	relative velocity
v_f	flow velocity
r	radius
O0	Configuration with outwardly curved structures at 0°
O90	Configuration with outwardly curved structures at 90°

I0	Configuration with inwardly curved structures at 0°
I90	Configuration with inwardly curved structures at 90°
U_{max}	Maximum velocity
S	Configuration with smooth surface
k	Depth of the hexagonal structures
d	Equivelent diameter of the hexagonal structures
u', u_{rms}	Fluctuating velocity
u_{eff}	Effective velocity
φ	Incident angle of the camera with vertical
r.m.s	Root mean square

Investigation and Optimization of the flow over macroscopic hexagonal structured surfaces

1. Introduction

1.1 Motivation

The structured pre-products carry a huge potential to serve as raw material for the building blocks, especially in automotive industry, Railways and Aerospace due to their known advantages like high quality functional properties and light weight. For an efficient economic use of structured sheets, development of a comprehensive database of technological properties, processing techniques, design criteria's and mastering of production and logistic processes is required. Currently, this data is not available due to lack of trained engineers in this field. To achieve the above mentioned goal, a state financed Graduate class named 'Destrukt' was established. The graduate class was divided into 9 different disciplines to investigate the various aspects of structured sheets as following.

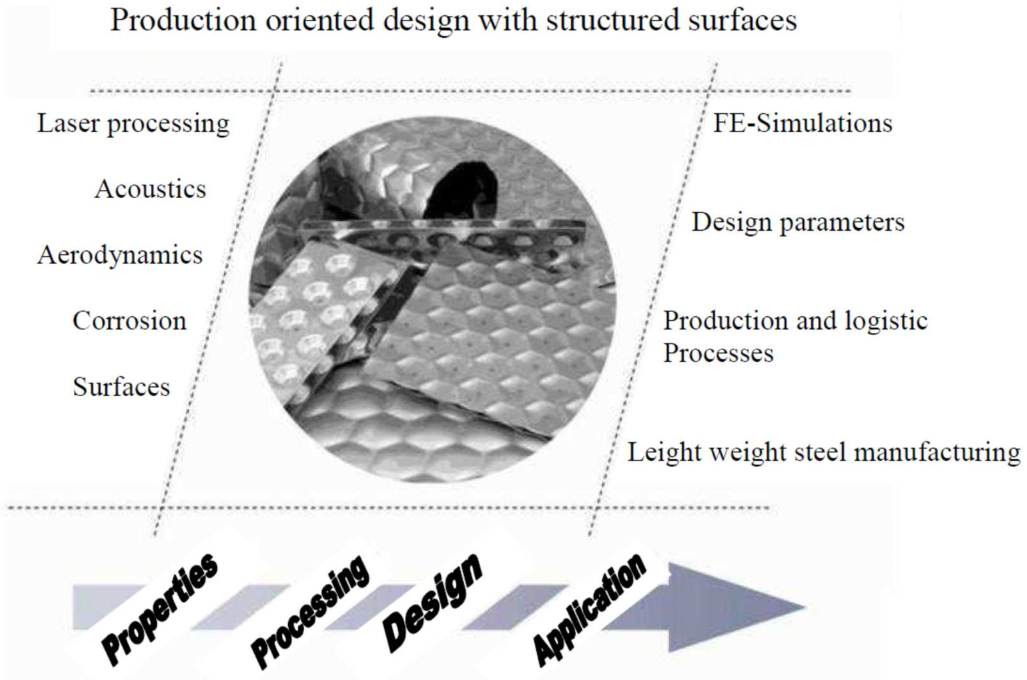

Fig 1: Various aspects and areas of investigations on a way to their application

To examine the possible application of structured sheets in aerospace industry, aerodynamic properties of structured plates must be investigated. This dissertation deals with the various aspects of such investigations such as the pressure drag, skin drag, vortex shedding and boundary layer. One of the crucial and most important concerns of aerospace industry is the drag. A significant drag reduction results in a reduced fuel consumption and hence a lower operating cost and a higher efficiency. Numerous ways have been developed by the researchers and the designers in last decades to reduce the drag of flying bodies. The very first ways were to streamline the bodies as much as possible. The essence of this approach is to prolong the laminar flow regime on the surface. However, for very high Reynolds numbers such as in a flight of a conventional transport aircraft, in order of 10^8, it seems doubtful that an economical method for maintaining the laminar flow regime can be developed under these conditions. Similarly, drag reduction for bluff bodies, which is of great importance especially in sports and automotive industry, requires other ways to achieve the desired goals as these are not to be streamlined. The major drag reduction methods for a bluff body can be segmented into four different categories (Fig. 2). It should be noted that all the methods considered here assume that the boundary layer be attached up to the rear separation point occurring at the contour of the body base. This obviously implies that the shape of the front part of the body be such that no global boundary layer separations occur (no sharp edges);

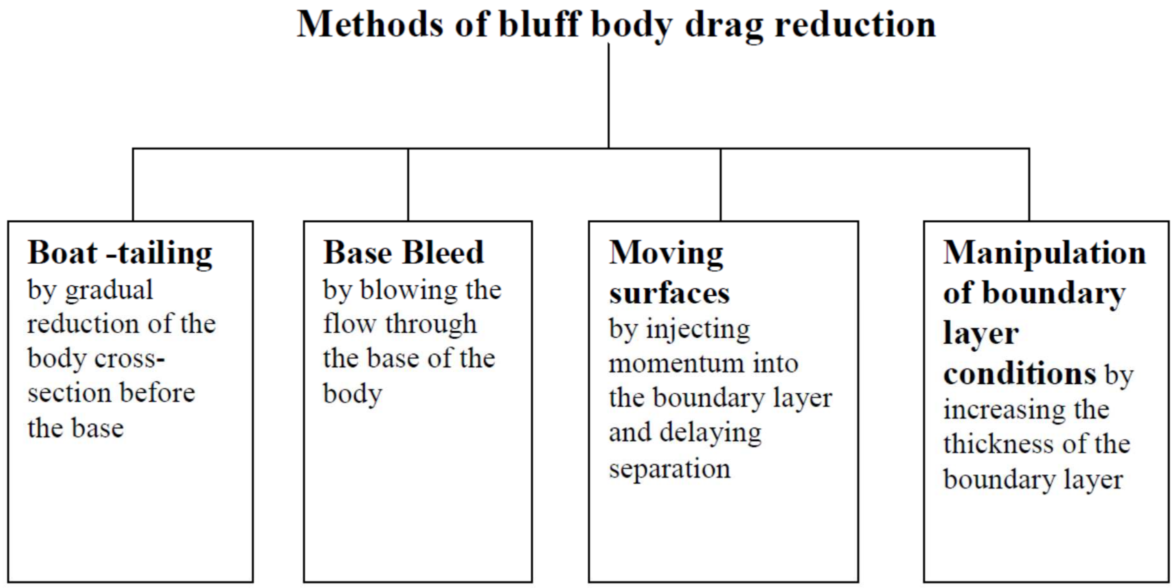

Fig 2: Classification of methods of bluff-body drag reduction

Applying Dimples on a golf ball, first investigated by Davis [1], is a practical example of manipulation of boundary layer conditions. The dimples on the surface of the ball turn the laminar boundary layer into turbulent, increase its thickness and delay the separation of the flow from the surface. This reduces the pressure difference in the upstream and the downstream direction and hence the drag acting on the ball (Fig. 3).

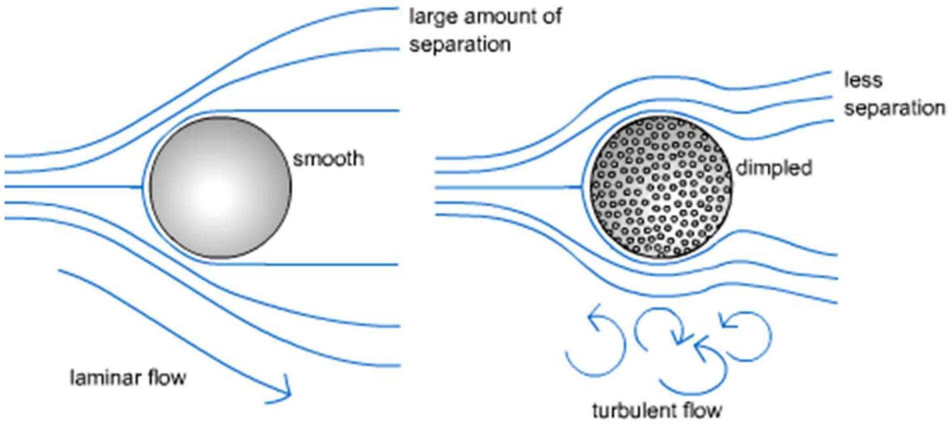

Fig 3: Flow over a smooth and a golf ball

Several other methods, which mostly fall in the same category, have also been developed to control the flow either in an active or in a passive way. Active ways involve periodic blowing and suction on the surface [2], placing smaller bodies in the upstream direction [3], application of electromagnetic field during the flow of electrically conducting fluids [4], placing a control plate upstream of the body **[5]** and a moving surface boundary layer [6]. Several passive ways have also been adopted which follow a similar mechanism of drag reduction as the dimples such as the roughened surfaces [7], dimples [8], grooves [9], seeps [10], circular rings placed at regular intervals along the length of a cylinder [11].

The total drag acting on a body moving in a medium is mainly composed of pressure drag and skin drag. Skin drag constitutes very little in the drag of bluff bodies. Whereas, the major source of drag for a streamlined body such as the wing of a transport aircraft is skin drag, about 50 % (Fig. 4). Again, several active and passive flow control strategies have been improvised. Complaint walls [12], Riblets [13] and vertical sub-layer elements called as vertical large eddy break-up devices (LEBU) [14] are classified as passive techniques. Synthetic jets [15], loudspeakers [16], air micro blowing [17], MEMS [18] and periodic blowing/suction [19] affect the structure of near-wall turbulence in an active way. A more detailed classification of Skin drag reduction methods is presented in figure 5.

Riblets have proven to be the most promising and practical tool of reducing the skin friction. Various hypotheses have been presented by Alving & Freeberg [20] to explain the mechanism of skin drag reduction by using riblets. One thing can

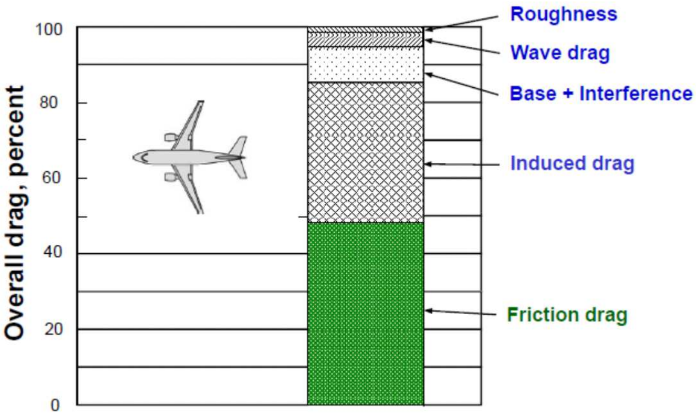

Fig 4: Distribution of drag on an aircraft wing, from Ref [14], used by permission

confidently be said that the turbulent momentum exchange near the wall is reduced using riblets with an optimum geometry. The counter-rotating longitudinal vortices are the major flow structures in the puffer layer and can be identified by the propagation of near wall horse-shoe vortices. These are produced by the instabilities near the wall and self-replication of existing horse-shoe vortices.

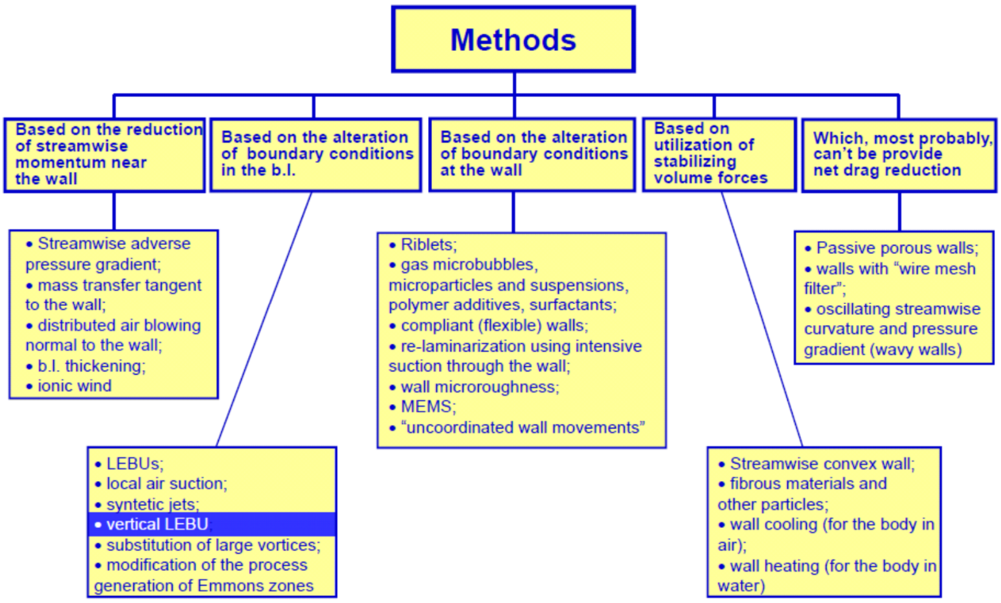

Fig 5: Classification of methods of reducing Skin-drag, from Ref [14], used by permission

Due to the rotational motion of the vortices, the fluid is transported towards or away from the wall depending on the direction of rotation. Low energy regions are found among the vortices in longitudinal direction in the viscous sub layer. The side of these vortices, which is turning away from the surface, transports the energy away from the wall into the boundary layer. The counter rotating side enables the transfer of energy from the boundary layer to the wall. This contributes to the production of significant amount of energy besides blowing out the vortices. The longitudinal vortices, which create shear stress in the viscous sub-layer, have more or less similar strength. By obstructing the lateral movement of longitudinal vortices, the riblets weaken the three dimensional vortex structures reducing the vortex intensity near the wall. The wall shear stress is proportional to the gradient of the mean flow velocity above the wall. Due to reduction in surface friction caused by the riblets, the flow velocity near the wall is consequently reduced [21].

Some controversial results regarding the investigations of flow over dimpled plates exist in literature. According to some researchers such as the famous study by DLR Spiegel [22], a significant amount of skin drag reduction could be achieved for a dimpled surface, although no explanation is yet available for the observed effect. On the other hand Leinhart [23] proved with the help of experimental and numerical investigations that the drag of a dimpled plate rather increases slightly.

No such investigations on hexagonal structured surfaces are known yet. The main concern of this dissertation is to investigate the flow over hexagonal structured surfaces and assess their capability of affecting the drag of the body. Following fundamental questions are dealt in this dissertation, which were planned to be addressed by conducting a series of experiments in a Wind tunnel:

- Investigation of the fundamental effects of hexagonal structures on the flow
- Is Pressure or Skin drag reduction possible?
- Mechanism responsible for any alteration in Pressure/Skin drag
- Flow behavior/Visualization within/around the hexagonal structures
- Examination of the validity of the scaling laws in a turbulent boundary layer
- Optimization of classical measurement techniques to perform measurements on structured plates (considering measurement accuracies)

1.2 Aims and Approaches

In the present dissertation, the influence of hexagonal structured surfaces and their orientations to the flow on aerodynamic quantities such as Pressure and Skin drag, Vortex shedding and boundary layers, is investigated. Examination of each quantity requires a separate indigenous experimental setup. Hence, the experiments were divided into three categories i.e. experiments on bluff bodies (structured circular cylinders), streamlined bodies (structured plates) and finally a wind turbine. These were conducted in the laboratories of fluid mechanics at the institute of Fluid mechanics & Aerodynamics and the institute of Combustion and Aero engines at the Technical University of Cottbus. A constant mass flow rate was ensured during experiments by the use of a large nozzle and governing the angular speed of the impeller. Based on the diameter of the cylinder and the mean flow velocity, the investigations on cylinders were performed for Reynolds numbers $Re = 3.14 \times 10^4$ to 2.77×10^5. Whereas, the Reynolds numbers ranged from $Re_x = 3.4 \times 10^5$ to 11×10^6 for structured plates based on the length of the test plate and the mean flow velocity. The investigations on wind turbine took place for flow velocities from 3 m/s to 18 m/s. The objective of these experiments was to quantify the effects of hexagonal structures on the flow over the structured objects as well as examine their applications. Subsequently, the results of direct drag measurements, velocity profiles, flow visualizations and shear stress measurements were obtained for structured as well as for smooth surfaces to perform a comparison between flow control methods in the literature and the present structures.

Various structured surfaces with identical hexagonal structures but different orientations along with a smooth surface were investigated during experiments. To perform a comparison of the results of present structures with other structures in literature, a depth to diameter ratio (k/D) for circular cylinders, where D is the diameter of cylinder and k/d for plates, where d is equivalent diameter of a hexagonal structure, was defined. The experimental setup and the measurement techniques are explained in detail in fourth and fifth chapter.

The sixth chapter deals with the results of measurements on structured cylinders. Drag measurements predicted a direct effect of hexagonal structured surfaces on the pressure drag of a cylinder, i.e. a significant reduction in pressure drag. Velocity measurements in the wake of cylinders and smoke flow visualization vindicated the observed effect. Ultimately, a mechanism of the observed reduction in the drag of a cylinder is presented with the help of measured velocity profiles near the surface. A detailed comparison of the effect of various structured surfaces on Vortex-shedding behind a cylinder is also present in this chapter.

Second section of the sixth chapter presents the results of the experiments performed on structured plates and discusses the reproducibility of a fully turbulent flow. By using the velocity profiles measured above the surface of smooth and structured plates, several boundary layer quantities were determined and subsequently analyzed. These quantities predicted again some dramatic effects of hexagonal structures on the mean stream flow, i.e. fall in local skin drag and a rise in total drag. To comprehend these effects, shear stress and pressure measurements on individual hexagonal structures were performed. Besides that, r.m.s velocity profiles at various locations and power spectrum of the flow above individual hexagonal structures was obtained to resolve any turbulent structures present in the flow. Quantitative flow visualization using oil film interferometry helped to articulate the near wall flow.

The third section of the sixth chapter describes the results of the experiments conducted on a wind turbine configurations made of structured as well as smooth blades. The results are compared, analyzed and discussed briefly.

Finally, the findings and conclusions are summarized in seventh chapter. Some still open questions and future prospects based on experimental results are identified. Some suggestions for further investigations are also presented in this chapter.

2. Theoretical background

Total drag is formally defined as the force corresponding to the rate of decrease in momentum in the direction of undisturbed external flow around the body, this decrease being calculated between stations at infinite distances upstream and downstream of the body. Thus it is the total force or drag in the direction of undisturbed flow. It is also the total force resisting the motion of the body through the surrounding fluid. There are number of separate contributions to total drag:

2.1 Pressure drag

This is the drag that is generated by the resolved components of the forces due to the pressure acting normal to the surface at all points. It may itself be considered as consisting of several distinct contributions:

I. Induced drag (sometimes Vortex drag)
II. Wave drag
III. Form drag

In case of bluff bodies such as circular cylinders only some 5% of the drag is skin-friction drag, the remaining 95% being from pressure drag, although these proportions depend on the Reynolds number. Bluff bodies are characterized by more or less premature separation of the boundary layer from the surface, and by wakes having significant lateral dimensions and usually unsteady velocity fields. Considering bluff bodies with fixed separation points, significantly different flow fields characterize the wakes of 2-D bodies perpendicular to the flow, and 3-D bodies that are elongated in the direction of the flow. Indeed, even if in both cases the wake velocity field is unsteady, the fluctuations are much higher in the first case, in which the wake flow is dominated by the alternate shedding of strongly and highly concentrated vortices, producing the well-known Ka´rma´n vortex street. The shedding of vortical structures is still present in the wake of axis-symmetric bodies with a rounded leading edge (and thus with attached boundary layer up to the rear separation line), but structures are weaker, less concentrated and less organized. The latter are directly connected with the magnitude of the fluctuating forces acting on the body.

Consider the case for example, the pier of a bridge in a river. The water speeds up around the leading edges and the boundary layer quickly breaks away from the surface. Water is sucked in from behind the pier in the opposite direction. The total effect is to produce eddy currents that are shed in the wake. There is a buildup of positive pressure on the front and negative pressure at the back. The pressure force results in form drag. When the breakaway or separation point is at the front corner, the drag is almost entirely due to this effect but if the separation point moves along the side towards the back, than a boundary layer forms and skin friction drag is also produced. A bluff body has high velocity, low pressure regions on the upper surface. The closer streamlines represent a faster velocity (Fig. 6). At the back of the body, this high speed, low-pressure flow has to return to the free stream conditions.

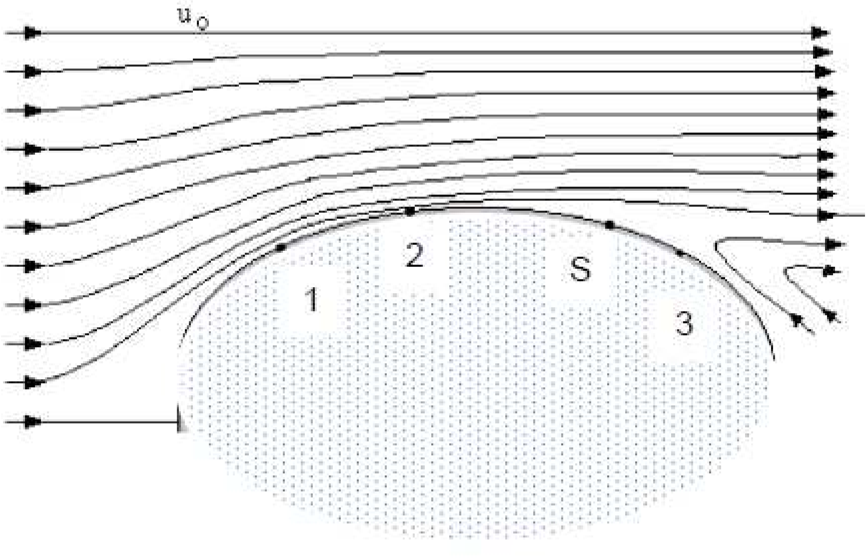

Fig 6: Flow around a bluff body

Thus, there is an adverse pressure gradient acting on the fluid particles. Particles closest to the body lose kinetic energy due to viscous losses. They come to a halt when they lose all their kinetic energy and lack sufficient kinetic energy to overcome the adverse pressure gradient (S_2 in Fig. 7)

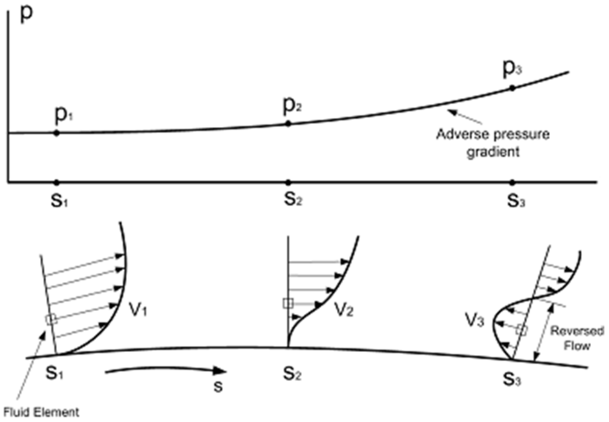

Fig 7: Reversed flow in presence of adverse pressure gradient, from Ref [70], used by permission

This results in the flow separating from the surface creating a large wake of recirculating flow downstream of the surface. The turbulent boundary layer might reattach with the surface again forming a separation bubble. Form drag is due to pressure changes only. The pressure coefficient is denoted by C_d and is defined as following.

$$C_d = \frac{2R}{\rho u_\infty^2 \text{ x } projected\ area} \qquad 2.1.1$$

The force exerted by the pressure on a small surface area is p dA. If the surface is inclined at an angle ψ to the general direction of flow, the force is p cosψ dA. The total force is found by integrating all over the surface.

$$R = \oint p cos\psi\ dA \qquad 2.1.2$$

The pressure coefficient is defined as:

$$C_p = \frac{2(p - p_0)}{\rho u_\infty^2} \qquad 2.1.3$$

Where p_0 is the static pressure of undisturbed fluid, u_∞ the velocity of undisturbed fluid and ρ the density of the fluid.

Flow separation caused by the adverse pressure gradient can have severe implications. Consider an aircraft wing flying at moderate speed, increasing the angle of attack of the wing would result in stall and the aircraft goes out of control. It is well known that the boundary layers on low-Reynolds-number airfoils would remain laminar at the onset of the pressure recovery unless artificially tripped. The behavior of the laminar boundary layer on low-Reynolds number airfoils would affect the aerodynamic performance of the airfoils significantly. Since laminar boundary layers are unable to withstand any significant adverse pressure gradient, laminar flow separation is usually found on the airfoils, and post-separation behavior of the laminar boundary layers accounts for the deterioration in the aerodynamic performances of low-Reynolds-number airfoils. The deterioration is exhibited in a dramatic increase in drag and decrease in lift (Fig. 8).

It has been suggested in the literature that the separated laminar boundary layers around a low-Reynolds-number airfoils would behave more like free shear layers, which are highly unstable, therefore, rolling-up of Kelvin-Helmholtz vortex structures and transition to turbulent flows would be readily realized. When the adverse pressure gradient over the airfoil surface is adequate, the transition of the separated laminar boundary layer to turbulent flow could be conducted rapidly, and the increased entrainment of the turbulent flow could make the turbulent flows to reattach the airfoil surface as turbulent boundary layers. This would form what is called a laminar separation bubble. The reattached turbulent boundary could stay in attaching to the airfoil surface firmly up to the airfoil trailing edge. As the adverse pressure gradient become more severe with the increasing angle of attack, the separation bubble would burst suddenly, which result in airfoil stall subsequently.

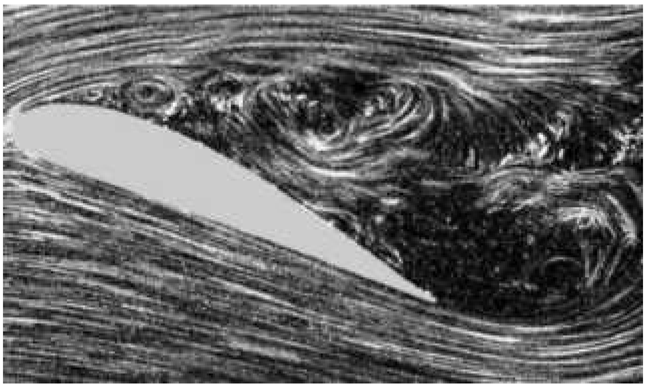

Fig 8: separated flow over airfoil, by Ref [71] used by permission

2.2 Skin Drag

Skin friction drag is due to the viscous shearing that takes place between the surface and the layer of fluid immediately above it. This occurs on surfaces of objects that are longer in the direction of flow compared to their height. Such bodies are called streamlined. When a fluid flows over a solid surface, the layer next to the surface may become attached to it (it wets the surface). This is called the no ‘slip condition’ The layers of fluid above the surface are moving so there must be shearing taking place between layers of the fluid. The shear stress acting between the wall and the first moving layer next to it is called the wall shear stress and denoted by τ_w.

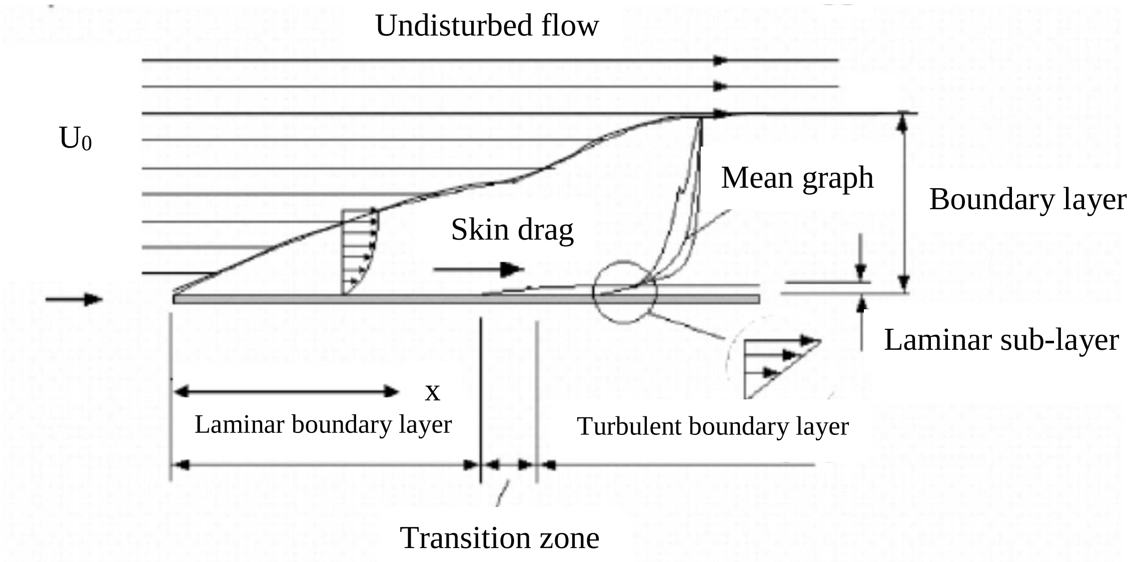

Fig 9: Schematic diagram of the flow over flat plate

It is essential to investigate the flow near the wall (the boundary layer) to comprehend the effects of structured surface on the skin drag and total drag of the plate. The shape of the velocity profiles near the wall depends upon various factors including Reynolds number, shear stress and density. Hence, they need to be determined. The boundary layer is mainly of two types, the laminar and the turbulent boundary layer. Only viscous and inertial forces play a vital role in case of a laminar boundary layer. The laminar layer becomes unstable and transforms into a turbulent boundary layer at a critical Reynolds number (Fig. 9). Various mathematical formulations are present in the literature to describe a turbulent boundary layer over a flat plate. The *logarithmic law* is the most commonly used description.

$$\frac{u(y)}{u_\tau} = \frac{1}{\kappa} ln\left(\frac{yu_\tau}{\nu}\right) + B \qquad 2.2.1$$

Where $u_\tau = \sqrt{\tau_w/\rho}$ is the shear stress velocity, u(y) the velocity, y the vertical distance from the surface and κ and B are constants. Common values of κ and B are 0.41 and 5.2. The logarithmic law is used to determine the wall shear stress acting on the surface by assimilating it with the measured velocity profiles. This method of determining the wall shear stress was devised by Clauser [24]. It is explained in detail in Section 5.4.1. The wall shear stress and the dimensionless shear stress coefficient C_f can be computed by knowing the shear stress velocity and density of the fluid.

$$\tau_w = \rho u_\tau^2 \qquad C_f = \frac{\tau_w}{\frac{\rho}{2}u_\infty^2} = 2\frac{u_\tau^2}{u_\infty^2} \qquad 2.2.2$$

For a plate of length l and width b the skin drag can be determined by integrating the shear stresses over the area in streamwise direction.

$$R(x) = b\int_0^x \tau_w dx \qquad 2.2.3$$

Putting it in the definition of drag coefficient:

$$C_F = \frac{R}{\frac{\rho}{2}u_\infty^2 bl} \quad => \quad C_F \frac{2}{l}\int_0^l C_f dx \qquad 2.2.4$$

Global skin drag (the total drag) can also be determined by using boundary layer quantities such as displacement and momentum thicknesses

2.3 Fundamentals of Boundary layer

The boundary layer thickness δ is taken as the distance required for the velocity to reach 99% of u_∞. It is possible, however, to define the boundary layer thickness in terms of an effect on the flow indirectly. The displacement thickness is defined as the distance the surface would have to move in the y direction in an inviscid fluid stream of velocity u_∞ to give the same flow rate as occurs between the surface and the reference plane in a real fluid.

$$u_\infty \delta_1 = \int_0^\infty (u_\infty - u)dy \qquad 2.3.1$$

$$\delta_1 = \int_0^\infty \left(1 - \frac{u}{u_\infty}\right) dy \qquad 2.3.2$$

Analogous, the momentum thickness is the distance by which a surface would have to be moved parallel to itself towards the reference plane in an inviscid fluid stream of velocity u_∞ to give the same total momentum as exists between the surface and the reference plane in a real fluid.

$$\rho u_\infty^2 \delta_2 = \rho \int_0^\infty u(u_\infty - u)dy$$

$$=> \quad \delta_2 = \int_0^\infty \frac{u}{u_\infty}\left(1 - \frac{u}{u_\infty}\right) dy \qquad 2.3.3$$

By having known the momentum thickness of the boundary layer, the global skin drag of a plate of width b and length l can be determined.

$$R(x) = b\int_0^x \tau_w dx = \rho b \int_0^{\delta(x)} u(u_\infty - u)dy$$

$$R(x) = \rho b u_\infty^2 \delta_2(x)$$

By putting this relation in the definition of drag coefficient, following can be achieved;

$$C_F = \frac{\delta_2 - 1}{x_2 - x_1} \qquad 2.3.4$$

3. State of the art

The quest for drag reduction has compelled the researchers to look for new ways and strategies to control the flow. Most of the strategies which aggravate the aerodynamics of a streamlined body are actually quite useful to improve the aerodynamic performance of bluff bodies. Although the findings of some experiments regarding the use of dimples as a drag reduction strategy for streamlined bodies is controversial, they proved to be surely beneficial for controlling the flow over bluff bodies.

3.1 Drag reduction of bluff bodies

Roughening the surface by applying sand on the surface has proven to be an effective way by Achenbach [7,25,26]. A roughened surface with sand particles of several diameters had been investigated. The results of these investigations suggested that the drag crisis which occurs for a smooth cylinder at about Re = 3 x 10^5 moves towards a lower Reynolds number in the subcritical regime. The drag coefficient of the roughened cylinder starts increasing after dropping to its minimum at a critical Reynolds number and rises to a much higher value in the post critical regime for all investigated k/d values (Fig. 10). The reason of this increase is thought to be due to the effect of roughness on the development of turbulent boundary layer. The roughness thickens the turbulent boundary layer causing an earlier separation of the boundary layer at high Reynolds numbers. Dimples on a cylinder influence the shear layer over the surface of the cylinder reducing its drag coefficient [8]. Besides that, the drag coefficient of a dimpled cylinder remains unchanged even at higher Reynolds numbers in contrast to the sand roughened cylinder (Fig. 10). The frequency of the vortex shedding caused by a dimpled cylinder is rather higher than a smooth cylinder at critical Reynolds number (Fig. 11). According to choi [27] no vortices are generated from the dimples during transition of the flow from laminar to turbulent and hence are not responsible for the transition.

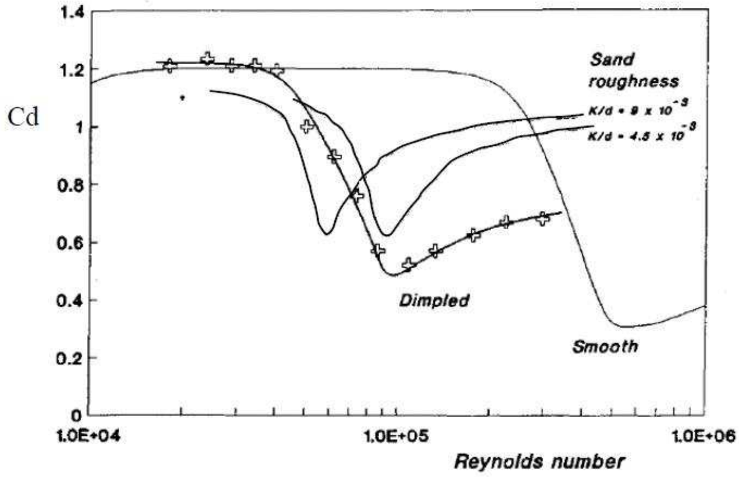

Fig 10: Drag coefficient for smooth, dimpled, and roughened cylinders: smooth [28]; dimpled (k/d=9x10^{-3}) [29]; Sand roughened (k/d=9x10^{-3}, 4.5x10^{-3}) [25]. Here k is the height of roughness or depth of dimples, by Ref [8], used by permission

Grooves [30] have also proven to be an effective way of controlling the flow passively. The drag coefficient drops suddenly at about Re = 4 x 10^4 and rises again to a value higher than the value of drag coefficients of the dimpled cylinder as the Reynolds number increases. The triangular grooves appear to have a better effect on the drag coefficient as compared to the circular grooves with 15% lower value of drag coefficient. Similarly the higher number of grooves on the cylinder causes the critical Reynolds number to shift towards left affecting the flow positively. No information on the vortex shedding by the grooved cylinder is available.

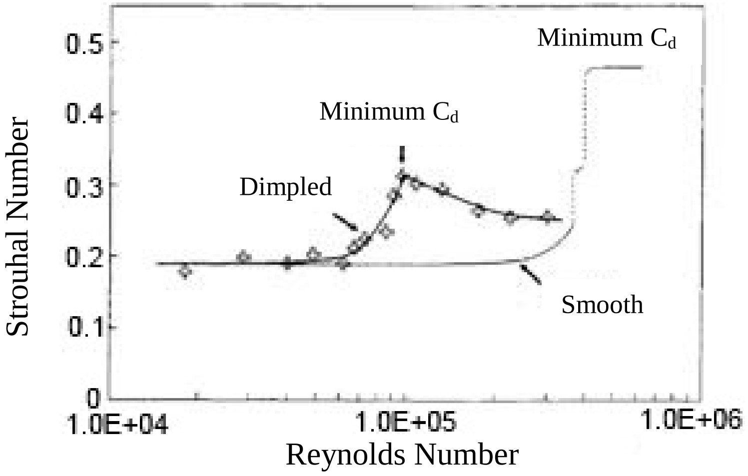

Fig 11: Variation of Strouhal number against Re for smooth and dimpled cylinder, by Ref [8], used by permission

Placing a small cylinder in the upstream direction of the flow also reduces the drag coefficient of the cylinder to about 52% over a certain range of Reynolds numbers [3]. The shear layer coming from the smaller cylinder affects the pressure distribution around the larger cylinder in such a way that the separation process is altered and hence the aerodynamic forces are reduced. The flow over sphere can also be controlled actively. Jeon et al. [2] has demonstrated that a time periodic blowing and suction from a slit on the sphere with a forcing frequency in a range of one to thirty times the natural vortex shedding frequency reduces the drag significantly by about 50%

The flow separation over circular and square cylinders can also be suppressed by applying electromagnetic fields during the flow of electrically conducting fluids. The flow of a viscous, incompressible and electrically conducting fluid over a Reynolds number range of 10-40 and at a low magnetic Reynolds number is considered in the work of Chattarjee et al. [4]. Mechanism of drag reduction by using a surface trip wire on a sphere for $0.33 \times 10^{-2} < k/d < 1.33 \times 10^{-2}$, which is somewhat similar to mechanism of a dimpled sphere, has explicitly been explained by K. Son et.al [32]. The effect of a flat plate placed upstream of a square cylinder over a Reynolds number range of 50-200 has been studied by S. Malekzadeh et al. [5]. The results show that the optimum position and width for the control plate are a distance of 3D away from the cylinder and a width of 0.5D (D the diameter of cylinder), respectively, where the almost maximum reduction of the fluid forces and the minimum reduction of the heat transfer are provided. Using a control plate also delays the onset of the vortex shedding. A 60% reduction in drag and a significant decrease in the maximum amplitude of oscillation for the cylinder have been observed by I. Korkischko et al. [6] for a cylinder with moving surface boundary layer. Two small rotating cylinders strategically located inject momentum in the boundary layer of the cylinder, which delays the separation of the boundary layer. Forced reattachment of shear layers separated from a cylinder has been achieved by setting up a screen around the cylinder by Oruc [10]. As a consequence the formation of vortical flow pattern was suppressed.

3.2 Drag reduction of streamlined bodies

Riblets of various sizes and geometries have proven to be a practical and effective way of reducing the global skin friction between the surface and the flowing medium. The cross-section of a (Riblet) is characterized by a triangle or a Trapizium and the cross-section of a groove’s peak as an equilateral triangle. Introducing fences on the surface along the direction of the flow influence the boundary layer near the wall in such a way that the skin drag is reduced [33]. The same structure was found independently on the skin of sharks by a Zooligist in 1982 [34]. Riblets are fine grooves encarved parallel to the direction of the flow which can reduce the skin drag under specific conditions. Various forms and shapes of Riblets have been studied in the past years to comprehend their effects on the flow. Squire & Savill [35] investigated saw shaped Riblets with a constant groove height and breadth in a supersonic wind tunnel. The measurements showed a 3% reduction in Skin-drag. Bechert et al. [36] illustrated a maximum achievable reduction of 8% with saw shaped and 10% with V-shaped riblets for Reynolds numbers between 5000 and 33000. Hage, Bechert und Bruce [37] studied quantitatively various Riblet geometries for different angles of incidence with the flow. Skin drag reduction by trapizun shaped grooves was found to be least sensitive to varying angles. Debisschop & Nieuwstadt [38] have demonstrated a 13% reduction in skin drag for V-shaped Riblet with trapezium shaped vales as compared to a smooth surface. Sundaram, Viswanath, Rudrakumar [39] also reported a 15% skin drag reduction for the Riblets of V-shaped cross-section encarved on an airfoil NACA 0012. These experiments were conducted at a free stream velocity of 30 m/s.

Another way of controlling the flow that has intensively been studied in the recent years is the use of dimples. Introducing a regular arrangement of surface depressions called dimples is well known measure to increase heat-transfer from a wall. Compared to a smooth wall, the Nusselt number can significantly be enhanced by dimples with a small increase in pressure drop. For that purpose, deep dimples with a ratio of depth to diameter of h/D=0.2-0.5 are typically applied to enhance the convective transport from the wall [40]. Alekseev et al. [41] discovered that apart from heat-transfer enhancement, dimples might be useful for drag reduction. Their findings are based on experimental measurements of turbulent flows over surfaces with a regular arrangement of shallow dimples leading to a decrease in drag of a turbulent flow up to 20%. However, no clear explanation has yet been provided which can illuminate this effect. Hence, some doubts remain regarding the experimental investigations and their outcome. Therekov and lagrani [42] described a pressure field in a shallow dimple. According to them, a primary vortex pair is shed from the central portion of a dimple, including a large upwash region. This shedding occurs periodically and continuously and is followed by the inflow advection into the dimple cavity. The strength of the primary vortex pair increases as the height to the diameter ratio of the dimple decreases.

Various Research groups reported contradictory conclusions on the effect of dimples on skin friction drag. Some of them could measure a significant reduction in skin drag, whereas others measured an increase. Kiknadze et al. [43] investigated dimples with a h/D ratio of 6% and achieved a noticeable reduction in drag coefficient. Shushkin et al. [44] recorded a reduction in a range of 5 – 18% for dimples with a height to diameter ratio of 14…18%. Yu Lashkov [45] presented totally contradictory results. Dimples of h/D=7…15% were investigated for Reynolds numbers Re_x ranging from 3×10^6 to 9×10^6. No influence on laminar-tubulent transition as well as an increase in drag was observed as compared to a flat surface. Further propositions came from Chyu et al. [46] Moon et al. [47], Mahmod et al. [48] and Ligrani et al. [49], in which a positive influence of dimples on the skin drag was falsified. Bunker and Donnellan [50] investigated even deeper dimples of h/D=23.3…39.4% and measured much higher drag than a flat surface.

A famous study on dimples was conducted by German Aerospace in 2004 [22]. The experiments were performed on scaled train models and a reduction of 16% in total drag was reported and discussed in the Press.

Leinhart et al. [23] investigated partly through experiments and rest through numerical simulations a dimpled surface of h/D =0.05 and 0.042. Drag of the plate was measured by using the law of momentum and compared with the drag of a flat plate. No reduction in drag, rather an increase for higher dimple diameters was recorded.

The reduction of skin friction drag through the injection of gas to form micro bubbles in a liquid turbulent boundary layer has received a good deal of attention. The pioneering work in this field was done by McCormick and Bhattcharra [51], who used electrolysis to generate bubbles over a towed body of revolution and observed a significant reduction in skin drag. The influence of the type of gas on the performance of micro bubble skin friction reduction was investigated on an axis-symmetric body by A.A. Fontaine [52]. Gases covering a wide range of densities and solubilities showed qualitatively a similar behavior. A 60% reduction in skin drag by injecting micro bubbles into the flow immediately upstream of a floating drag balance has been reported by Y. Kodama et.al [53]. It was found during their investigations that the local void ratio (ratio of gas to the total volume flow rate in the boundary layer) close to the wall has strong correlation with skin friction reduction. Y Murai et al. [54] investigated the dependence of the average skin drag on the bubble-size in the intermediate bubble size condition. By using bubble sizes of 2-90 mm a negative correlation between the skin drag and the local void fraction was confirmed through time-resolved measurements. An experimental investigation to reduce skin-friction drag of turbulent boundary layer was conducted with an electro conductive solution in water by J. Pang et al. [55]. An array of actuators made of permanent magnets interleaved with copper electrodes, which were set flush with the wall surface across the flow. Due to the Lorentz force created by the setup in the cross-flow direction, skin-friction reduction of about 40% was observed. Large eddy break-up devices are also employed to control the flow of turbulent boundary layer.

Boiko and Kornilov [56] reported a skin-drag reduction of about 28% by installing LEBUs of dimensionless height $h^+=194$ ($h^+=hu_\tau/\nu$), width $c^+=99$, thickness $t^+=1.43$ and packing $\lambda^+=69$ (u_τ is the shear stress velocity and ν the kinematic viscosity) on a flat plate.

No studies have yet been made on the flow over cylinders and plates with hexagonal structures or patterns. Therefore, the presented results serve as a contribution for a fundamental understanding of the described patterns, which can be referred as hexagonal dimples or bumps. The behavior of the patterned cylinders for a particular range of Reynolds numbers is investigated using flow visualizations, measuring their drag as well as the boundary layer velocity profiles above the cylinder surface. The evaluation of the measurement data supports the view of drag reduction due to patterned surfaces. The responsible mechanism is explained in detail in section 6.1.5 considering the already known drag reduction mechanisms for dimples and rough surfaces. The motivation behind the Experiments on structured plates was mainly to investigate the influence of hexagonal structures on the flow over patterned plate and assess their capability of affecting the global drag coefficient of the plate. The above mentioned task was accomplished by analyzing the boundary layer quantities such as local & global drag coefficients and momentum thicknesses at various positions along the direction of the flow.

4. Experimental Setup

The Wind tunnel in the Institute of combustion & aero engines provided a platform to achieve above mentioned targets regarding investigations on structured surfaces. It is a closed circuit wind tunnel with an open Test chamber. The dimensions (in mm) of the Test chamber are shown in Fig. 12.

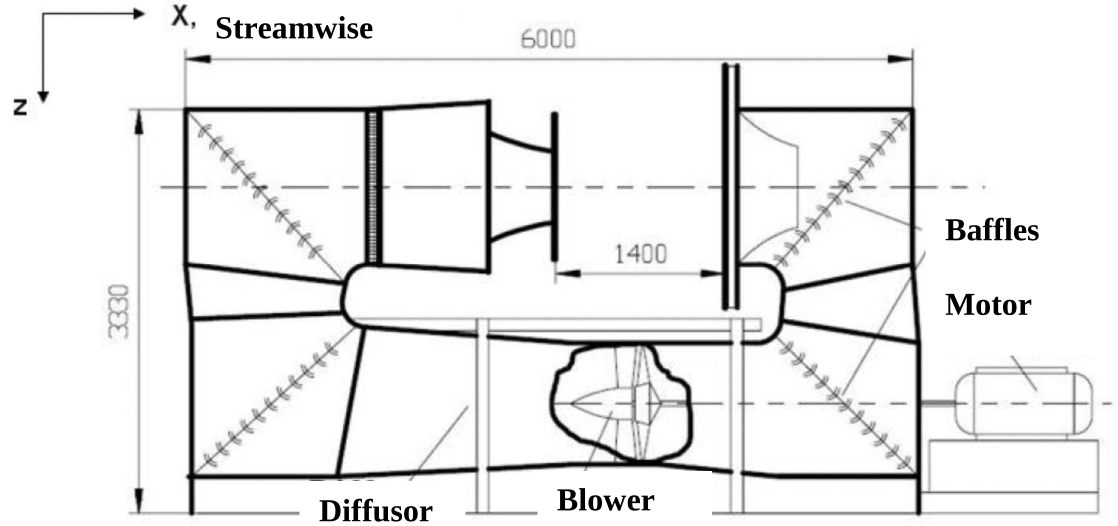

Fig 12: Wind tunnel at Institute of Internal combustion and aero engines

One of the most fundamental tasks was to determine the Turbulence intensity of the flow over the cross-section of the wind tunnel nozzle. To determine the turbulence intensity Tu hot wire measurements were performed along the central axis of the Test chamber. Turbulence intensity was measured along y and z-axis. The measured turbulence intensity lies within the range of Tu = 0.4 - 0.6% except on the edges due to the shear layer coming from the walls of wind tunnel. A graphical presentation of these measurements is shown in Fig. 13 and Fig. 14.

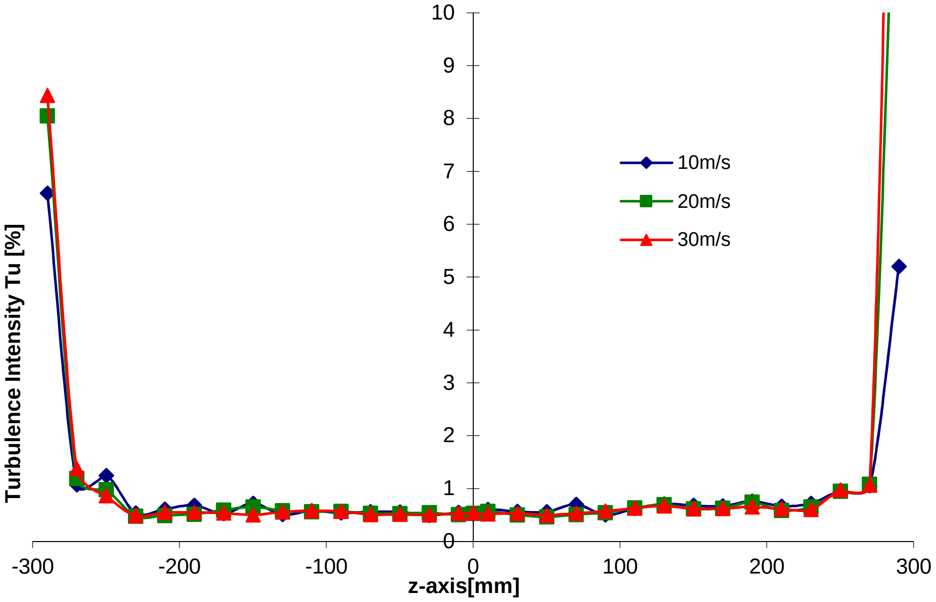

Fig 13: Turbulence intensity along z-axis

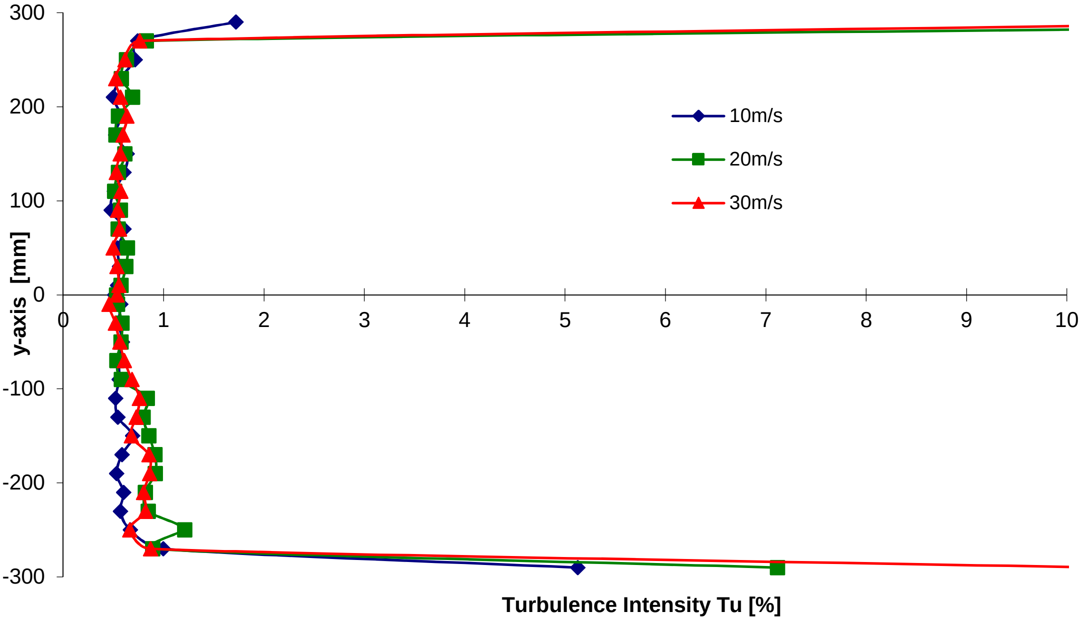

Fig 14: Turbulence intensity along y-axis

Additionally, the laboratory is equipped with measurement techniques such as Hot wire Anemometry, piezoelectric pressure modules with multiple inputs, Fog machine & Cameras for flow visualizations and Oil film Interferometer. All the techniques are described in detail in section 5. Two different experimental setups were improvised to investigate various aspects of hexagonal structured surfaces and described in following sections.

4.1 Bluff body investigation

A U-formed frame made of my-tech aluminum profiles was made and test cylinder mounted on it horizontally across the flow. A schematic diagram of the setup is presented in Fig. 16. The length of the cylindrical is 49 cm and disks of diameter 18.5 mm were placed on its ends to prevent the secondary flow or any three dimensional effects disturbing the measurements performed on the cylinder. The Test cylinders being hollow from inside were held in the fluid stream with the help of a cylindrical holder and an axle passing through its axis. The axle is supported by the U-formed frame on both sides. Due to the depth of hexagonal structures, the inner diameter of the cylinders with inwardly curved structures and outwardly curved structures cannot be identical. Hence, a holder whose diameter could be varied was designed and fabricated. The cylindrical holder was made of a plexy glass cylinder of diameter 145 mm. Acyrl glass cylinder was cut through the middle to form a slit, whose gap can be widened or narrowed according to the requirement. The width of the slit was adjusted by using a bolt and a nut mechanism on the top and bottom of the holder (Fig. 15). The width of the slit and hence the diameter of the acryl glass cylinder can be varied by rotating the bolt in clock-wise or anti clockwise direction.

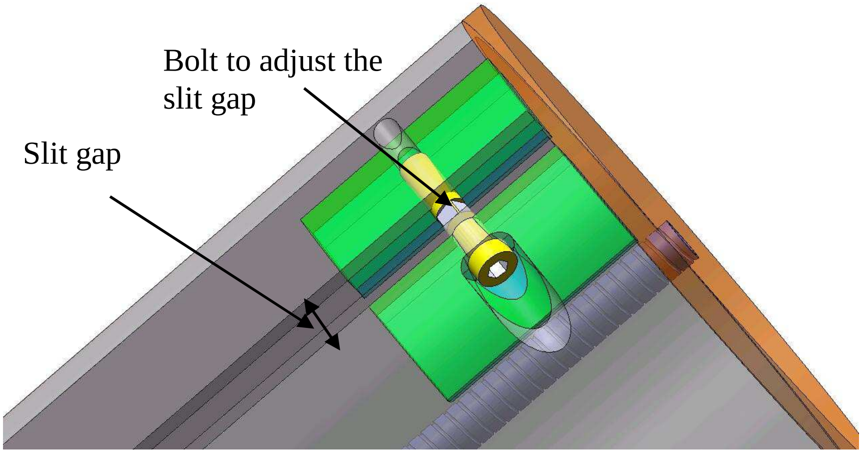

Fig 15: Nut and bolt mechanism to vary the diameter of the cylindrical holder

Now the test cylinders with multiple inner diameters could be fitted onto the cylindrical holder. The complete U-shaped frame and the test cylinder are supported on the cone edges on mutually perpendicular axes normal to and parallel to the flow direction for drag measurements. Whereas, the frame was kept fixed and standstill in a vertical position for velocity measurements and flow visualization. Drag force is measured by the piezoelectric gauge mounted on the wall of the wind tunnel. The U-shaped frame acts like a cantilever with its fulcrum pivoted on the cone edges and the cylinder and the sensor on either side. The drag acting on the cylinder pushes the other end of U-shaped frame against the piezoelectric sensor with a force in relation with the lever arm ratio. Due to point bearings used as supports for the frame, frictional effects, which would induce error in the measurement of drag are eliminated.

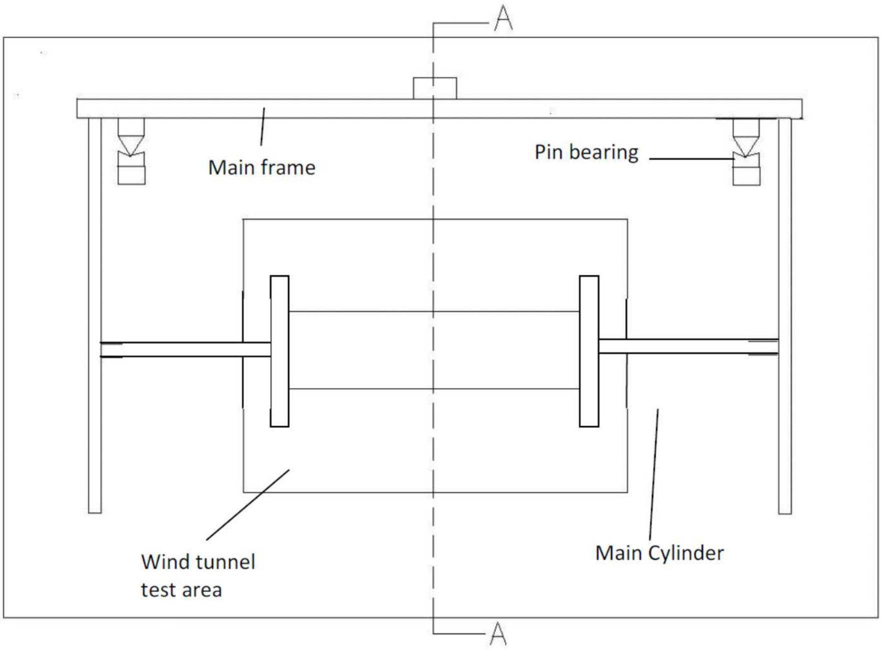

Fig 16-a: Experimental setup for the determination of drag acting on the cylinder front view (top), side view (bottom)

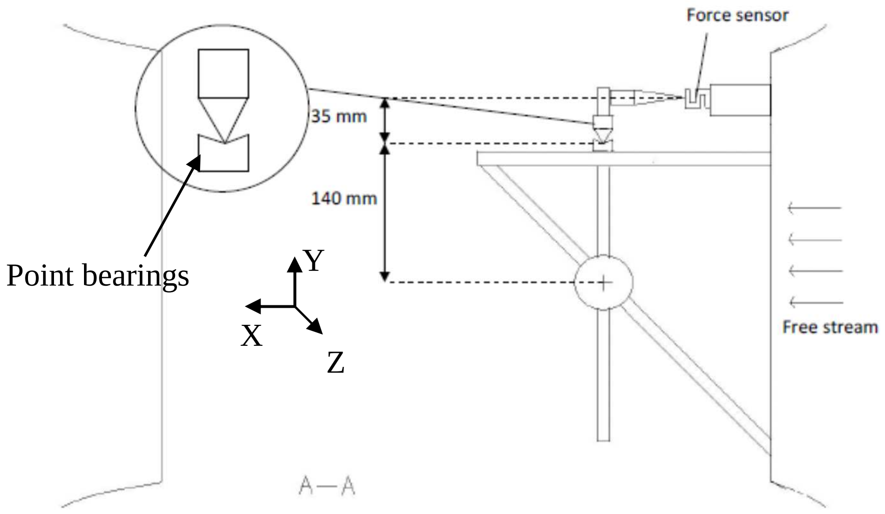

Fig 16-b: Experimental setup for the determination of drag acting on the cylinder front view (top), side view (bottom)

The investigated Reynolds numbers based on the diameter of the cylinder ranges to Re < 2.7 x 10^5, which is below the critical Reynolds number of a smooth cylinder. The investigated Reynolds number range is shown in Fig. 17

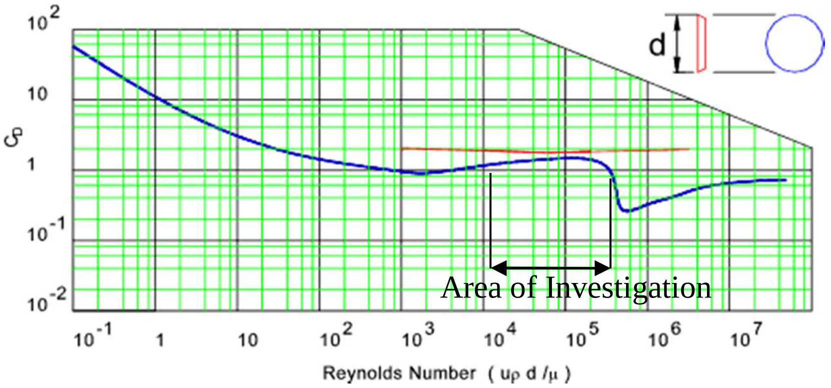

Fig 17: Drag coefficient of cylinder vs Reynolds number, by Ref [72], used by permission

4.2 Streamlined body investigation

A base plate with a wide pocket served as a platform for the structured plates to be investigated. The test plates of similar width as the base plate and smaller length were placed in the pocket of the base plate and fixed with the help of fixing elements on both sides. A flap to be mounted on the trailing edge of the base plate was also developed (Fig. 18). The test plate was placed horizontally in the test section of the wind tunnel and a flap mounted on the trailing edge of the plate was adjusted so that the pressure taps that are placed between the locations A and B at a distance of every 50 mm (Fig. 19) gave identical values. The deviations among the pressure readings lie within the accuracy limits of the measuring device. In this way, it was insured that zero-pressure-gradient is achieved along the plate surface. The width of the base plate was wide enough to guarantee that the three dimensional flow at the edges of the plate do not propagate and disturb the boundary layer in the center plane of the plate, where measurements were performed. The investigations took place in a turbulent boundary layer. To allow the transition of the flow from laminar to turbulent prior to the Test plate, sand paper strips were pasted near the nose of the base plate. The lowest velocity chosen for investigation was 19 m/s, which corresponds to a Reynolds number Re_x of 5.34 x 10^5 based on the location A to ensure that the boundary layer over the test plate is fully turbulent. The surface of the test plate was set flush to the surface of the base plate to avoid stepping and hence any local separation of the flow. The drag caused by the structured plate was measured with the help of velocity profiles at locations A and B and eq. 2.3.4

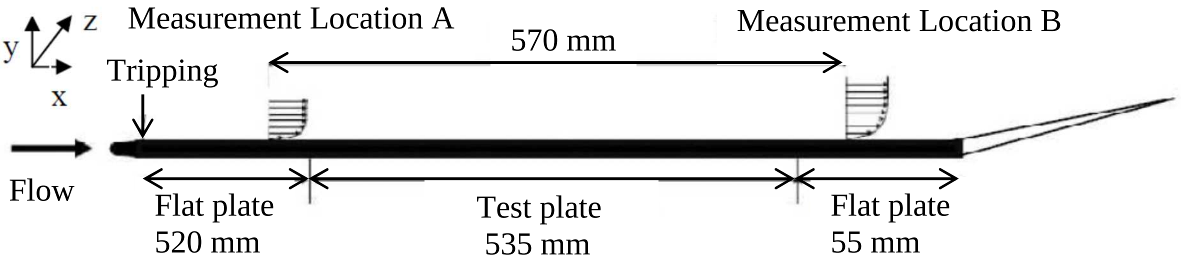

Fig 18: Experimental setup for the determination of drag of a structured plate

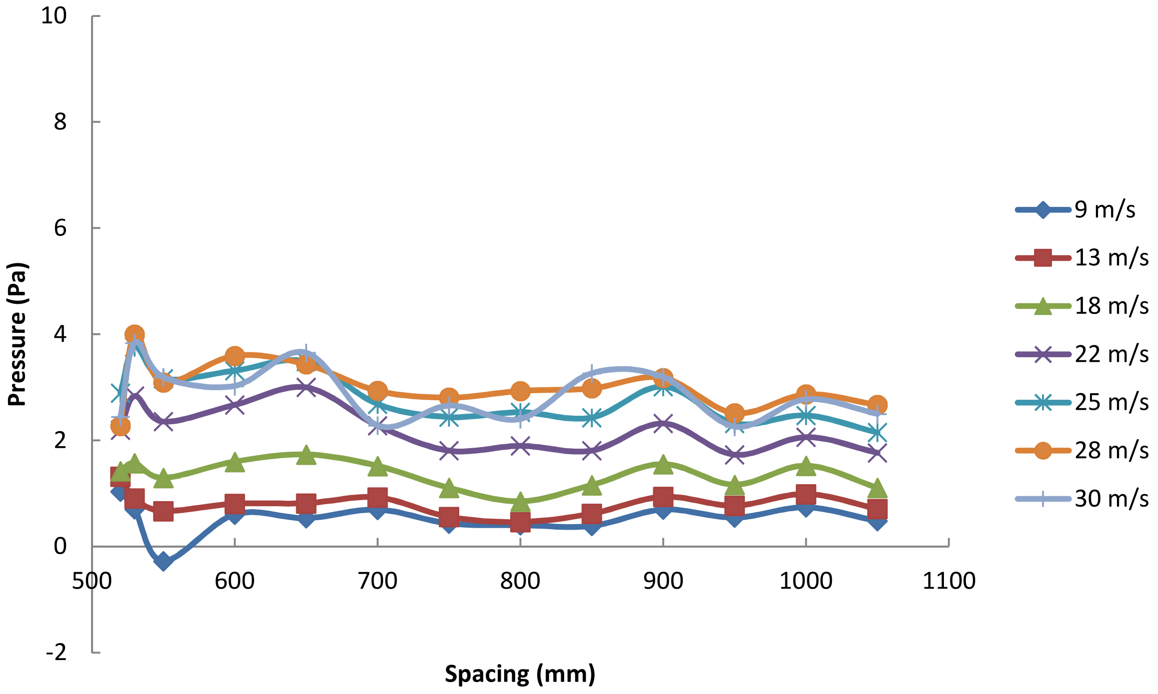

Fig 19: Pressure variation along the test plate

4.3 Investigations on experimental wind turbine

An experimental wind turbine consisting of a main Hub and 8 blades was developed to study the net effect of hexagonal structures on the efficiency of the turbine. The Hub of the turbine was made of aluminum with a cup and fastening screw at the center to fix it rigidly to the shaft. Eight bolts were inserted around the circumference of the Hub and fixed by using screws on the front side of the hub. The angle of incidence θ of the blades can be adjusted by rotating these bolts. Blades were fixed to each of these bolts with the help of two screws.

Hence, various configurations could be tested by simply losing the screws and replacing the blades. Various configurations of wind turbines were tested in above described wind tunnel. Experimental setup is shown in Fig. 20. Turbine is mounted on a shaft which is supported by two ball bearings. Ball bearings are fitted into bearing blocks which are fixed to a rigid aluminum stand. Output power of the turbine is measured by measuring the braking moment applied to the shaft by using an adjustable friction clutch and the angular speed by means of a tachometer. An adjustable friction clutch allows a set of braking moments ranging from nearly zero to 3 Nm to be applied to the shaft by simply adjusting the knurled ring. Hence output power can be determined at different angular speeds. As the clutch tends to rotate with the shaft, it is pushed against the sensor; the force exerted by the clutch is measured by the force measuring sensor. The sensor is placed at a perpendicular distance of 4.5 cm from the shaft. The product of the measured force and the perpendicular distance gives the braking moment resisting the angular motion of the shaft. The efficiency of the turbine is determined by using the following equation.

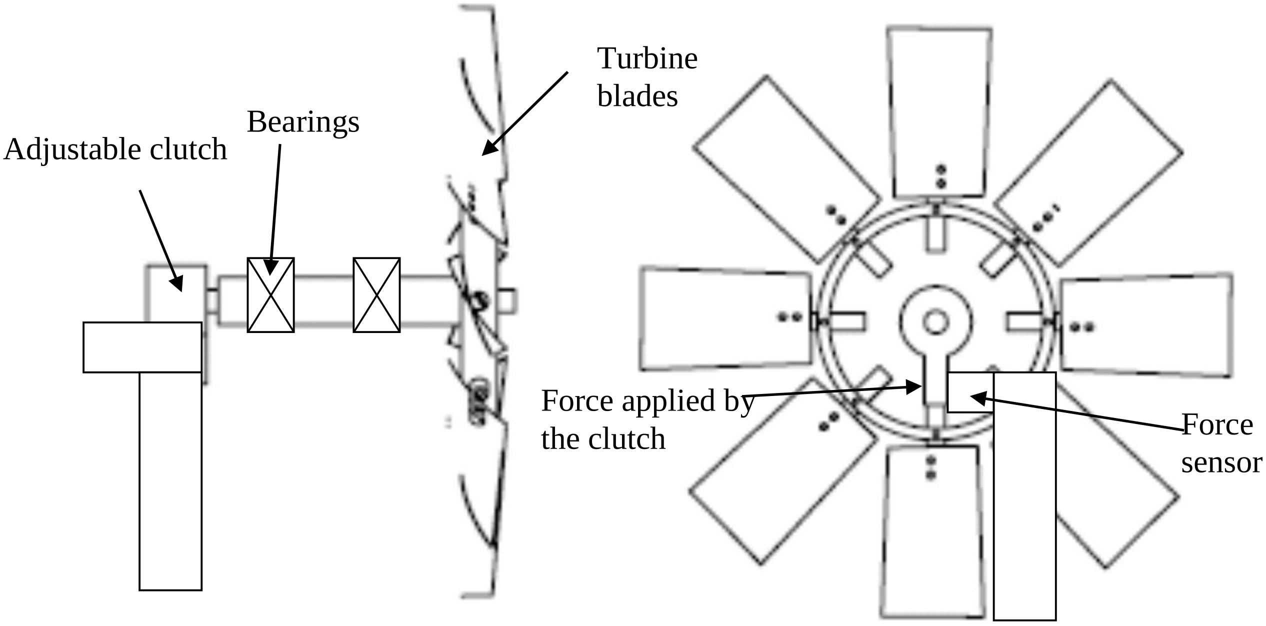

Fig 20: Experimental setup for determining the efficiency of the Turbine

$$\eta = \frac{P_{out}}{P_{in}} = \frac{M\omega}{0.5\rho A v^3} = \frac{\pi F c n}{15\rho A v^3} \qquad 4.3.1$$

Where η is the mechanical efficiency, F the braking force, c the perpendicular distance from the sensor, n the revolution per minute (rpm), ρ the density of air, A the area of turbine and v the velocity of air

4.4 Invested Configurations

As no investigations on hexagonal structures have yet been made, any size of the structures comparable with the known macro structures in literature such as dimples, grooves or cavities could be chosen. Another parameter which served as the criteria for choosing the size of hexagonal structures was the Reynolds numbers range. The Reynolds number range for experiments on cylinders was deliberately selected to be near the critical Reynolds number of a smooth cylinder to observe the effects of hexagonal structures on critical regime. Sheets with smallest available size of hexagonal structures (33 mm wide and 2.7 mm deep) could be formed into the diameter estimated on the basis of selected range of Reynolds numbers and the flow velocities without deteriorating its circular shape. Same size was selected for investigations on structured plates. It is essential to mention here that these patterns were created on steel sheets with a smoothed surface to avoid any effects of surface roughness on the flow. Investigations were performed in a subsonic wind tunnel with an open test chamber. The motivation behind these tests was to study the effects of above mentioned hexagonal structures on the flow of air and their contribution in affecting the drag of the body. The cylinders to be investigated were made by bending and welding patterned steel sheets; firstly with the patterns facing outwards and secondly with the patterns facing inwards. The orientation (Fig. 21) of these patterns towards the free stream of air was also changed during investigations, and hence the investigations could be performed for five different configurations. The length of the sheets required to form circular cylinders was calculated for a diameter of 156 mm through the formula l = pi*D where D is the diameter of the cylinder and l the length of the sheet.

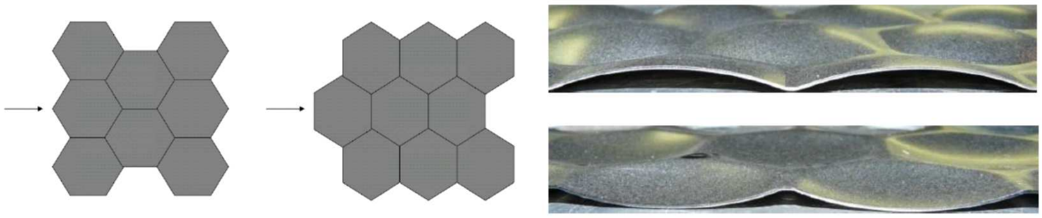

Fig 21: Structures plates with four different orientations 0° and 90°(left), outwardly curved and inwardly curved (right)

A diameter D must be chosen that gives a length, which can be bent and welded together without disrupting the continuity of the patterns on the line of joint.

Fig 22: Structured cylinders

	Configuration	Diameter	Direction/shape	k/D	Orientation/size
S	Smooth	156 mm	-	-	-
O90	Outwards 90°		Outwards/hexagonal	1.98 x 10^{-2}	90°/33 mm
O0	Outwards 0°				0°/33 mm
I90	Inwards 90°		Inwards/hexagonal		90°/33 mm
I0	Inwards 0°				0°/33 mm

Table 1: Properties of the configurations of structured cylinders

To compare the results of our investigations performed on the hexagonal structures with the classical structures like cavities and Dimples, depth to diameter ratios k/D for circular cylinders and k/d for structured plates were defined; where k is the depth of hexagonal structure, D the diameter of cylinder and d the equivalent diameter. An equivalent diameter for the present structures is determined by equating the cross-section areas of a hexagon and a circle and solving for the diameter of the circle. The depth and size of the hexagonal structures are 2.7 mm and 33 mm respectively. The experiments were conducted on four different structured configurations and a smooth flat surface for reference.

	Configuration	Length	Direction/shape	k/d	Orientation/size
S	Smooth	535 mm			
O90	Outwards 90°		Outwards/hexagonal	0.95	90°/33 mm
O0	Outwards 0°				0°/33 mm
I90	Inwards 0°		Inwards/hexagonal		90°/33 mm
I0	Inwards 90°				0°/33 mm

Table 2: Properties of the configurations of structured plates

In contrast to the dimples or grooves, hexagonal structures are not symmetrical in shape. These structures can be oriented to the flow in several ways, i.e. diagonal at 0° or parallel to the flow, diagonal at 90° to the flow. It is hence necessary to investigate and quantify any possible effect of the change in orientation of the structures.

Six different configurations of turbine blades were tested, including three configurations of flat and structured blades each. Due to their largest positive influence on the Form drag of the cylinder, only outwardly curved structures were applied on the blades. Blades are made by bending the plan and structured sheets, 14 cm long and 9 cm wide, to form an arc of 100 cm radius. As we know that the tip of the blade moves at much higher speed than the Hub, its angle of incidence must be smaller than the latter. To account for this effect, the sheets were bended in such a way that the inlet angle at the tip of the blade remains about 15° greater than that at the Hub. Fig. 23 describes the definition of various angles necessary to understand the operation of a turbine blade.

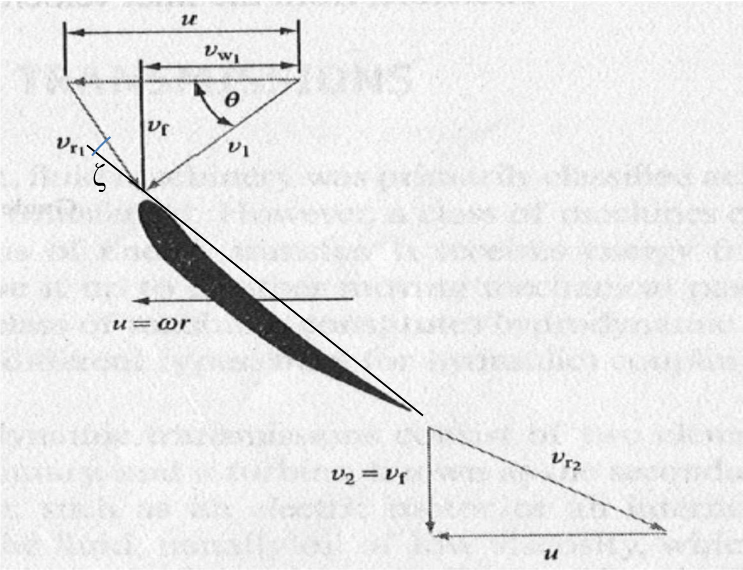

Fig 23: Definitions of various angles in a velocity triangle, v_r = relative velocity, v = absolute velocity, ζ = blade angle with relative flow velocity, ω = angular velocity, r = radius, v_f = flow velocity, by Ref [72], used by permission

Profile	ζ				Length / cm	Radius / cm
Flat	10°	20°	40°	60°	14	100
Structured						

Table 3: Configurations of investigated blades

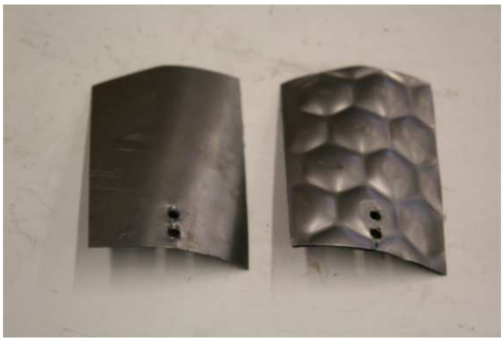

Fig 24: Turbine blades

Table 3 displays the configurations of the blades selected for the investigations. Turbine blades are shown in Fig. 24. There may be a plenty of parameters which can be adjusted and investigated but for simplification, mainly the angle of incidence of both the flat and structured blades was altered and the corresponding changes in the measured quantities recorded. The reason behind this simplification is the relation between the angle of incidence and the instability of a turbine blade. It is well known and already described in an earlier section that increasing angle of attack creates an adverse pressure gradient which results in flow separation above the surface of the blade. Consequently the aerodynamic characteristics of the blade are dramatically deteriorated. On the other hand, a higher angle of attack with a stable flow may give rise to a higher output power. The main purpose behind these tests was to investigate whether the hexagonal structure are capable of inhibiting the undesired flow separation and hence increase the efficiency of the turbine.

5. Measurement Techniques

5.1 Drag measurement

An S-shaped piezoelectric sensor was used to measure the drag force. The forces were measured at a sampling frequency of 4 Hz for 20 seconds. Signals were amplified through an amplifier and data recorded on a computer using commercial software from pce-instruments. The specifications of the sensor and measurement uncertainties are as follows:

- Dimensions 63 x 51 x 22 mm
- Resolution 0.2 N
- ±9.2% at a measured force of 9.3 N
- ±1.8% at a force of 180 N

5.2 Flow visualization

5.2.1 Smoke flow visualization

Visualization of the flow over cylinders was carried out by using an LED lamp which was placed directly above the cylinder (Fig. 25). The lamp produced a light sheet of a very small thickness and a width greater than the diameter of the cylinder. The power consumption of the lamp is 5 W. Fog was injected into the flow by using a 3 mm tube from a Fog machine (Fig. 25). The fog machine consumed a power of 1000 watts to produce smoke making the flow over cylinder visible. The images were captured by a digital Camera at a rate of 8 images/sec. The images were evaluated on a computer with the help of Microsoft Office picture manager. The digital camera was fixed on a tripod at a distance of 600 mm with its focus set on the Test cylinder.

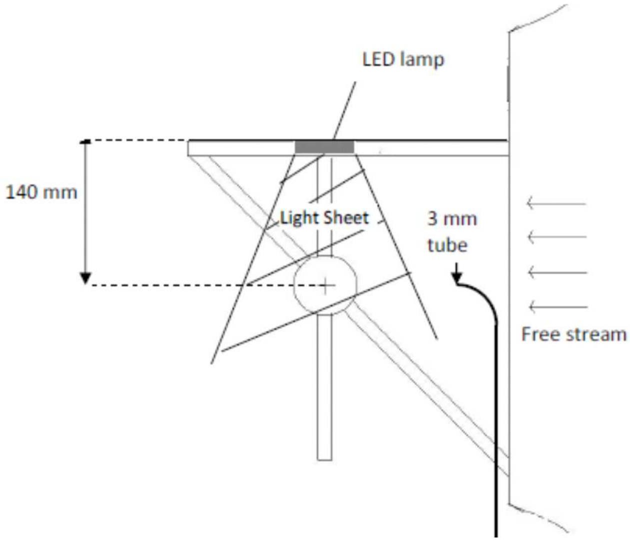

Fig 25: Setup for smoke flow visualization

5.2.2 Surface Oil flow visualization

Surface oil flow visualizations helped to visualize the flow above the surface of structured cylinders. A mixture of silicon oil having a viscosity of 19 mPa and Titnium dioxide was applied in a ratio of 2:1 in weight on the surface of cylinder. Silicon oils are preferred because of their chemical stability and because the viscosity of the oil does not vary with Temperature as much as other oils. After applying the mixture, the wind tunnel is set on immediately. The cylinder with the mixture on its surface is exposed to the flow for about 20 minutes and images are taken using the same digital camera after terminal conditions are achieved. Images are taken by mounting the camera above the cylinder at a distance of 47 cm.

5.2.3 Oil film interferometric Visualization

To visualize the flow over individual hexagonal structures, a sodium lamp was used. The sodium lamp produces monochromatic light of a wavelength 590 nm. An oil drop or a line is applied on the polished or a transparent surface blackened on the other side and wind tunnel is set on. Successive dark and bright bands called fringes starts appearing after some time under the monochromatic light of a sodium lamp. The fringes grow in the direction of flow and the spacing between fringes increases with the passage of time. The rate of increase in spacing is proportional to the mean flow velocity. These fringes not only articulate the flow near the surface and indicate the direction of the wall shear stress acting on the surface but also quantify it by using the relation devised by Tanner& Blow [57]. This technique is described in more detail in Section 5.4.2. The lamp and the camera were placed in a vertical plane parallel to the flow (Fig 26).

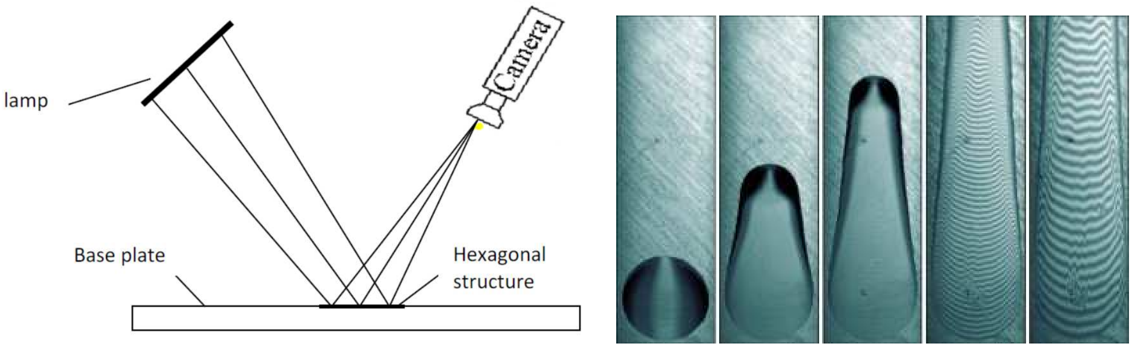

Fig 26: Setup for oil film interferometric visualization (left), typical fringe patterns evolution from oil film light reflections (right), by Ref [73], used by permission

5.3 Velocity measurements

The velocity profiles of turbulent boundary layers were measured by using Constant temperature anemometry. Boundary layer probe 55P15 and an X-wire probe 55P64 were used for the purpose. The hot wire, made of tungstun, has a length of 1.2 mm and a diameter of 5 µm. The probe calibration was performed in the free stream of air in the middle of the Test chamber using a Pitot tube placed 3 cm apart. The probe was calibrated for a velocity range of 0-33 m/s. The movement of probe was controled by a fully automatic traversing system capable of traversing in three diemensions with the smallest step of 15µm. A microsope with a maximum magnification of 200 and opical resolution of 9 Mega pixels was used to adjust the probe near the surface. The probe was traversed towards the surface with the smallest traversing step as long as the prongs and their shadow on the surface of the test plate nearly touched each other (Fig. 27). In this way, a positioning uncertainity of about 15µm was ensured. The traversing operation and the data acquisition were controlled by Dantec software called Streamware. The data signals from the hot wire probe were fed into a DA-conveter National instruments AT-MIO-16X. The bridge signal in a range of 1V to 8V of size 16 Bit is digitized within a measurement range of 0V to 10V with a sampling frequency of 10^4 values/sec. In this way, a resolution of 0.15mV or 0.002% is achieved. Measured data is plotted on the display of the software and saved at the specified location in computer. The velocity measurements were performed at a sampling rate of 10000 values/sec for 15 seconds. Mean velocities, r.m.s velocities and turbulence intensities were later deducted from the data.

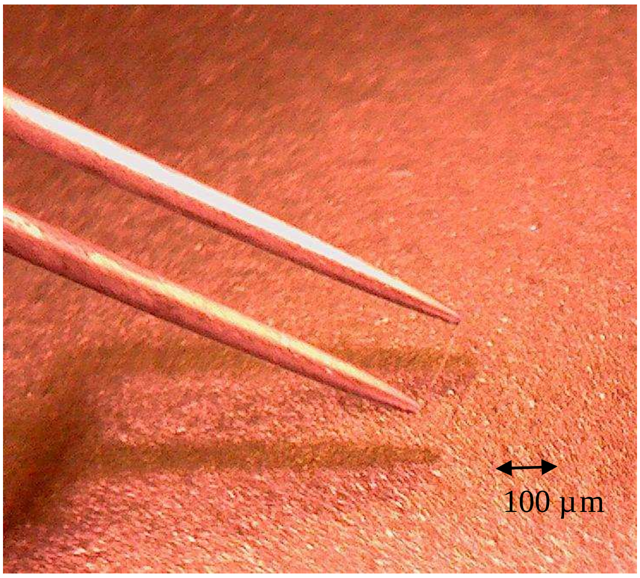

Fig 27: Positioning of hot-wire probe near the surface by using mirror-image technique

By using the shear stress velocity $u_\tau = \sqrt{\tau_w/\rho}$, dimensionless flow velocity $u^+ = \frac{\overline{u}}{u_\tau}$ and dimensionless wall distance $y^+ = \frac{y u_\tau}{\nu}$ a well-known linear relationship, the *law of wall* for the viscous sub layer of a turbulent boundary layer for y^+~5 is expressed as follows:

$$u^+ = y^+$$

Here, τ_w is wall shear stress and ρ the density of air. The kinematic viscosity of air is $\nu = 15.1 \times 10^{-6}\ m^2/s$ at normal pressure and 21°C. This relation can principally be used to determine the shear stress velocity and the wall distance from the surface. The method of determining shear stress velocity in this way is called Gradient method, in which the measured mean velocities are plotted against the distance from the surface. By calculating the gradient and y-intercept of these velocity profiles, shear stress velocity and the corrected wall clearance from the surface can be determined. However, the velocities measured near the surface were found not to be in a linear relationship with the distance. Rather, very high velocities were recorded near the surface. The observed effect near the wall is subjected to the thermal influence of the hot wire probe. As the hot wire probe comes very close to the surface, heat transfer not only occurs between the probe and the air but also between the probe and the test surface resulting in an enhanced flow of electrical current. A larger current through the hot wire sensor results in a higher sensed velocity. The hot wire anemometry is therefore not applicable for determination of wall shear stress by measuring the velocity gradient in the viscous sub layer of a turbulent boundary layer at least for the present Reynolds numbers. This effect is visible in the figures of Section 6.2.1.

For a zero pressure gradient turbulent boundary layer, logarithmic law

$$u^{+} = \frac{1}{\kappa} ln y^{+} + B$$

is valid for a range of $y^{+} \sim 35$ to about 40% of the boundary layer thickness δ depending on the Reynolds number [58]. A literature value of $\kappa = 0.41$ and logarithmic constant $B = 5.5$ has been used in this dissertation.

Hot wire anemometry has been a crucial tool also in obtaining vortex shedding frequencies in the wake of a cylinder or around the hexagonal structures. A hot wire probe was placed in the stream of air at a location where r.m.s velocity was maximum and data was recorded at a sampling rate of 5000 values/sec for 15 seconds. An FFT (Fast Fourier Transform) code developed indigenously in Matlab was applied to the Voltage-time series recorded by the hot wire probe. A peak in the plot (power spectral density vs frequencies) delivered the Vortex shedding frequency present in the flow.

5.4 Shear stress measurements

5.4.1 Clauser chart method

Clauser-chart method together with oil film interferometry has been used to determine the shear stress velocities. The Clauser-chart method, in its conventional form, makes use of the fact that all fully developed ZPG (zero pressure gradient) turbulent boundary layers possess a logarithmic region, with ‘universal’ constants, when plotted in inner coordinates (u^{+} vs. y^{+}). This is the so-called universal log law and is given by

$$\frac{u}{u_{\tau}} = \frac{1}{\kappa} ln\left(\frac{y u_{\tau}}{\nu}\right) + B \qquad 5.4.1.1$$

Using the measured mean velocity profile (u/U_∞ vs. y/δ) in conjunction with these already-known constants κ and B, the ratio U_∞/u_τ may be calculated from the log law. Here U_∞ is the free-stream velocity. There are many different but essentially equivalent ways of rearranging and solving log law equation, of which the following version was preferred and used for evaluation.

The conventional Clauser-chart method proceeds in the following steps.

- First, the measured mean velocity profile is plotted in u/U_∞ versus log (yU_∞/ν) form. Such a plot would make the extent of the logarithmic region in the mean velocity profile apparent. Once this extent is identified by visual inspection, it is fitted with a logarithmic curve. The end points of the logarithmic region are then fixed to obtain the minimal uncertainty. It was observed that the identification of the logarithmic region by visual inspection followed by a logarithmic curve fit is sufficiently accurate.
- The values of universal constants κ and C are already known
- The Universal log law is rearranged as

$$\frac{U_\infty}{u_\tau}\frac{\bar{u}}{U_\infty} = \frac{1}{\kappa}\ln\left(\frac{y}{\delta}\frac{\delta U_\infty}{\nu}\frac{u_\tau}{U_\infty}\right) + B \qquad 5.4.1.2$$

- Note that the eq. 5.4.1.2 is applicable only in the logarithmic region of the mean velocity profile. In the rearranged equation u/U_∞ values for different values of y/δ (in the logarithmic region) are known. The Reynolds number $\delta U_\infty/\nu = R_\delta$ is known for the measurement of the mean velocity profile and the universal constants κ and C are also known. Thus the only unknown in the rearranged equation is the ratio U_∞/u_τ. Since it is an implicit equation, the solution has to found by an iterative procedure. This may be done essentially by carrying out a regression fit. Using the value of U_∞/u_τ the skin friction coefficient can be obtained.

This is the essence of conventional Clauser-chart method. Evidently, the method strongly depends upon the universal nature of logarithmic law and hence is not suitable for situations where this universality is known to fail. Consequently, turbulent boundary layer flows involving strong streamwise pressure gradients are not suitable for applying the Clauser-chart method. There are several aspects in the implementation of this method that can introduce uncertainties in the estimated shear stress. One need to select the beginning and ending points in the data set that are believed to fall within the log-linear region, and this brings an element of user subjectivity into the result. A more important aspect however is the fact that the estimate of friction velocity is directly related to the choice of von Karman constant κ and B. Different values of these constant are reported in the literature [59]. Some studies have indicated that the Clauser-chart method produces artificially high friction velocities, especially at the low range of Reynolds numbers [60], [61], [62]. The friction velocity estimated from Clauser-chart method was reported to have an error varying between 8 and 20% over a Reynolds number in the range of Re_δ = 1000-10000. At very high Reynolds numbers, the larger extent of a well-developed log-linear region improves the accuracy of the Clauser-chart method as long as a suitably accurate value of is κ used. However, it has been shown by Wei et al [63] both experimentally and numerically that friction velocities obtained using Clauser-chart method can potentially mask subtle Reynolds-number-dependent behavior.

5.4.2 Oil film interferometric method

Oil film interferometry (Fig. 28) is based on the principle that there exists a relationship between the thinning rate of an oil film and the forces acting on the oil film such as shear force, pressure gradient and gravity.

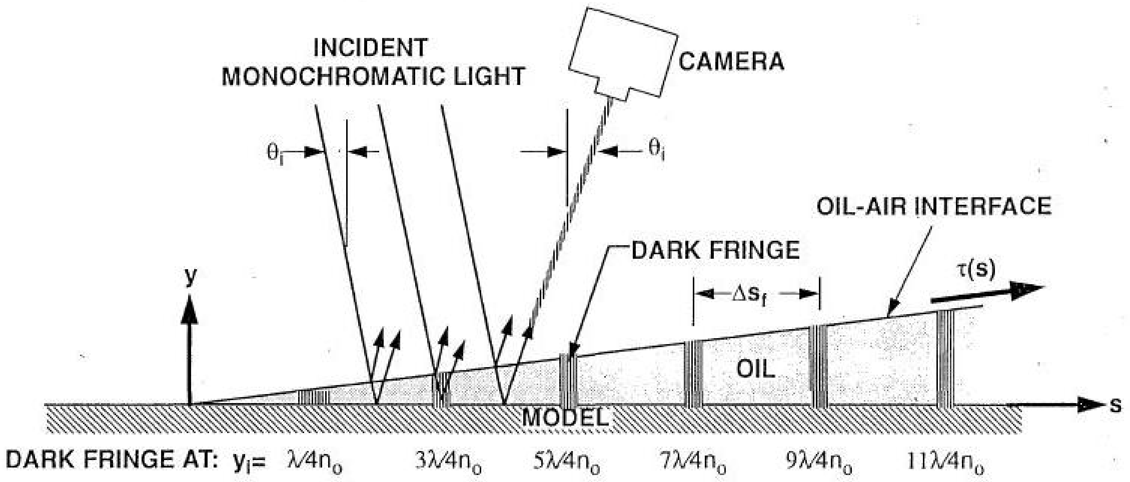

Fig 28: Schematic of oil film interferometry, by Ref [74] used by permission

As the oil film becomes extremely thin, the effects of gravity and pressure gradients can be neglected. This technique can hence be applied to the curved surfaces with pressure gradients. The major drawbacks of this technique are contamination of oil film and uncertainties regarding the properties of the oil, which have a major impact on the accuracy of the measurements. The thinning rate of oil film was first applied by Tanner & Blows [57] to the measurement of shear stress by using the thin oil film equation developed by Squire [64]. There are many variations of the oil film interferometry technique, all of which are based on the original form proposed by Tanner & Blows [57]. These fall into the categories of point, Line and image based techniques and included Laser interferometer skin friction, Fringe-imaging skin friction, Global imaging skin friction and Surface imaging skin friction methods.

As already mentioned that the oil film interferometry is based on the relationship between the thinning rate of the oil film and the three forces that may act upon it; gravity, pressure and shear force. When the oil film is sufficiently thin, the effect of gravity and pressure forces becomes negligible, and hence a linear relationship exists between the thinning rate of the oil and the shear force. The thickness of the oil film is most easily measured using interferometric techniques. Defining the co-ordinate system such that the x is the streamwise direction, y the wall normal direction and z the spanwise direction, than the relationship between the oil film gradient and the shear force expressed by Tanner & Blows

$$\frac{dy}{dx} = \frac{\mu_{oil}}{\tau_w t}(1+\varepsilon) \qquad 5.4.2.1$$

Where dy/dx is the instantaneous oil film gradient, μ_{oil} is the viscosity of the oil, $\tau_w$the wall shear stress, t the time and ε is the term associated with the effects of pressure gradients and is given by

$$\varepsilon = \frac{1}{3}\frac{y}{\tau_w}\frac{dP}{dx} + \frac{2}{3}\frac{\mu_{oil}}{t}\int_{p0}^{p}\frac{1}{\tau_w^2}dP \qquad 5.4.2.2$$

Since the thickness of the oil film reduces with time and hence for sufficiently thin films, ε will tend to zero and hence the effect of pressure gradient can be neglected. Assuming that the shear stress remains constant along the distance eq. 5.4.2.1 can be expressed as following:

$$\Delta y = \frac{\mu_{oil}\Delta x}{\tau_w \Delta t} \qquad 5.4.2.3$$

Δy is the difference in the height of oil film for consecutive fringes. According to Fernholz [65]

$$\Delta y = \frac{\lambda}{2\sqrt{n_{oil}^2 - n_{air}^2 \sin^2\varphi}} \qquad 5.4.2.4$$

Where λ is the wavelength of the light source (590 nm for sodium lamp) n the refractive indices of the oil and air respectively and φ is the incidence angle of illumination. By knowing the fringe spacing, wall shear stress can be calculated as follows:

$$\tau_w = \mu_{oil}\frac{\Delta x}{\Delta t}\frac{2\sqrt{n_{oil}^2 - n_{air}^2 \sin^2\varphi}}{\lambda} \qquad 5.4.2.5$$

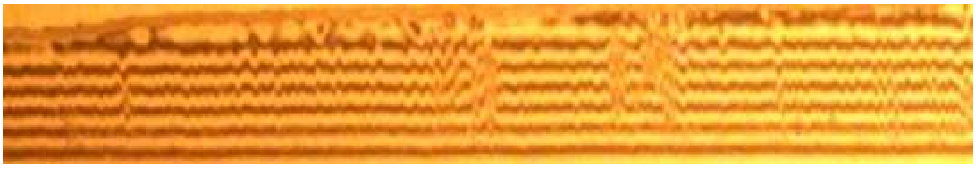

Fig 29: Fringe image on a flat test plate

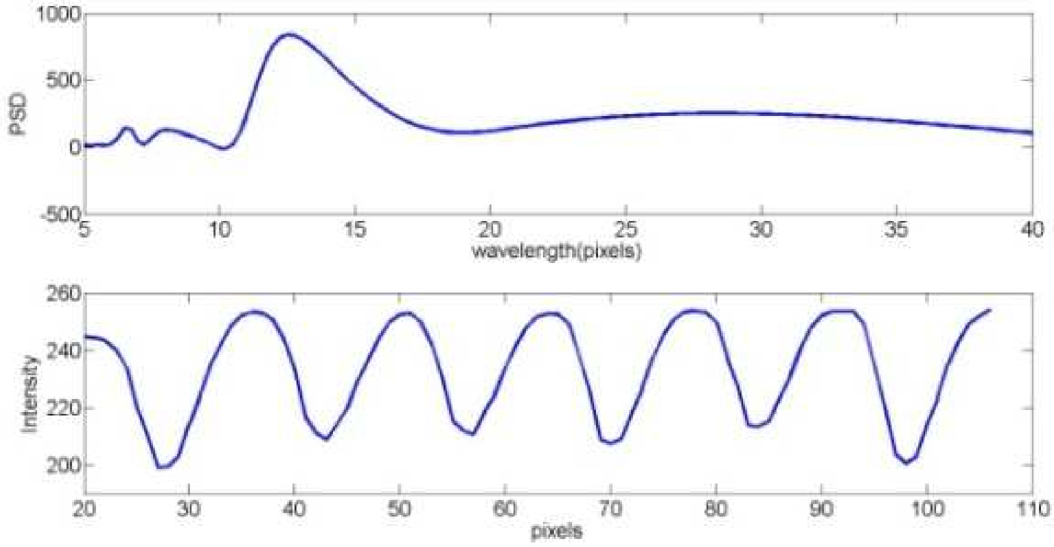

Fig 30: Fringe image (top), intensity and spectral density curves (PSD) (bottom)

The main disadvantage of this technique is the limitation regarding its application on semi refractive surfaces blackened on the opposite side such as glass or highly polished steel surface. As none of these is the case for our investigations, a monokote tape with adhesive consisting of a black surface with a thin layer of plastic on it was used. A monokote tape is pasted to the surface and oil line applied on it. This arrangement delivers the fringes with sufficient quality to evaluate the images accurately, a selected sample is shown in Fig. 29, and determine the shear stress coefficient. Disturbances seen on the film surface are the dust particles caught in the oil film, virtually unavoidable when measuring for extended times. The extended sampling times were deliberately chosen so that the effect of wind tunnel start up times be minimized. It means that the times spent in the transient condition would be small compared to the time spent in the test condition. The procedure of determining the value of shear stress coefficient is described in detail by Marusic et al. [66] and introduced in the following text.

This approach was implemented in Matlab by developing a code to perform Fourier analysis (Fig. 30). An interferogram can be imagined as a digital image comprised of rows and columns of pixels with each column taken to be perpendicular to the fringes in the interferogram, and each column of pixels will produce a pixel intensity signal resembling a periodic function (Fig. 30) since fringes are made up of recurrent light and dark bands. An FFT is applied to the signal and the fringe spacing in pixels is determined from the wavelength corresponding to the dominant peak of the power spectrum. This process is repeated for each column and then an average taken over the number of rows in the image so that a single wavelength is returned for each image in the sequence. With the scaling of pixels to meters and time, the rate of change of fringe spacing is calculated. The major sources of error include uncertainties in measurement of temperature dependent viscosity of oil and the measurement of fringe velocity.

An accurate determination of oil viscosity is essential to compute the wall shear stress accurately. Fig. 31 shows the temperature dependence of the oil viscosity. The variation in the oil viscosity due to change in temperature can cause a significant error. Wacker Silicon fluids AK (used in present experiments) are available in a viscosity range of 0.65 to 106 mm^{2}s^{-1}.

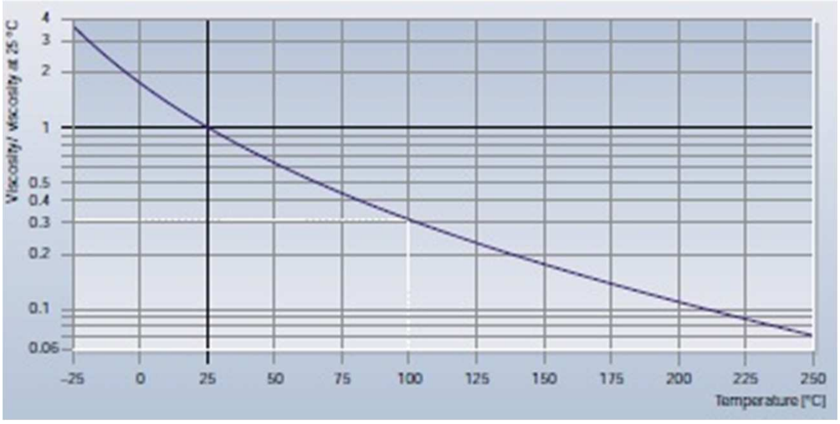

Fig 31: Temperature dependence of the viscosity of silicon oil

The 20 mm^{2}s^{-1} oil was chosen for the measurements. Silicon oils are preferred because of their chemical stability and because the viscosity of the oil does not vary as much as the other oils. The viscosity of the oil at a particular temperature during the experiment was determined by looking at the temperature dependence curve provided by the manufacturer. Other quantities required for calculating the wall shear stress such as the refractive index and the specific gravity of the oil were deduced from the manufacturer's data sheet.

5.5 Pressure & Temperature measurements

Static pressure measurements took place with the help of pressure holes drilled in the surface of hexagonal structures at a spacing of 6 mm from each other along x-axis. The 0.7 mm wide holes were connected to the pressure transducer with the help of rubber tubes of inner diameter of 2 mm. The pressure transducer has a measurement range of ±200 Pa and a measurement uncertainty of ±2 Pa or 1%. The temperature was measured with the help of a thermocouple sensor placed on the surface of the plate. The measurement range of the sensor is -60 – 240°C and measurement uncertainty of $\underline{+}$ 1°C. An accurate temperature measurement is essential for the correct determination of the oil viscosity. The values were recorded at a sampling rate of 1 value/sec for 20 seconds. A personal computer served as the data acquisition device through an IEEE data bus Interface. The evaluation of data was performed using softwares LABVIEW and MS Excel.

5.6 Braking moment and angular speed measurement

As described earlier, the moment delivered by the turbine at a particular speed was measured by applying a known braking moment with the help of an adjustable clutch. A force transducer with a measurement uncertainty of 0.5% of its full scale reading (200 N) was used for the measurement of the force. A laser Tachometer served to measure the revolution per minute of the turbine. The measurement took place contactless by applying a reflecting tape on the shaft. The measurement accuracy of the Tachometer is 0.05% of the measured value.

6. Results and Discussion

6.1 Structured cylinders

6.1.1 Drag Variation

Fig. 32 shows the measured drag coefficients against Reynolds numbers for all the investigated configurations.

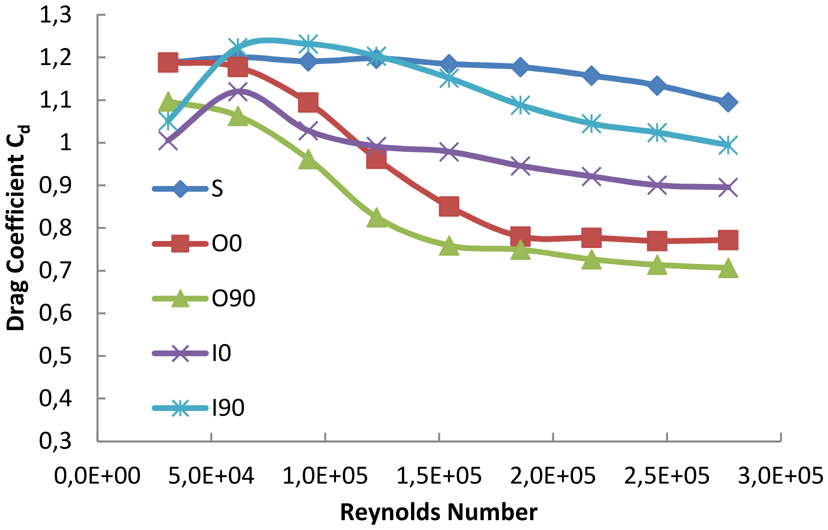

Fig 32: drag coefficients vs Reynolds Numbers: hexagonal patterns (k/d=1.98 x 10^{-2}), here k is the depth of hexagonal pattern

A data set of C_d (total drag constant) vs Re is presented in Fig. 32 for Reynolds numbers Re $\leq$ 2.8 x 10^5, which is quiet below the critical Reynolds number of a smooth cylinder (Fig. 10). A significant reduction in drag coefficient can be seen for nearly all the configurations for higher Reynolds numbers with the largest drop for O90. A small increase in the C_d values for I0 and I90 at lower Re-numbers is also present. The C_d values of I90 rise initially a little higher than the smooth cylinder and drop slowly to a value close to the C_d value of the configuration S. The most interesting fact to know about the hexagonal patterns is the observation of higher reduction in drag coefficient for the outwardly curved configurations (referred as hexagonal bumps) than the inwardly curved configurations (referred as hexagonal dimples) despite their resemblance to dimples in shape and structure. The minimum C_d value for dimples is in order of 0.5 whereas it is around 0.9 for inwardly curved and 0.7 (closer to the C_d of dimples) for outwardly curved hexagonal structures. It is also confirmed that these hexagonal patterns behave in a totally different way than the roughened surfaces, whose drag coefficient rises dramatically for higher Reynolds numbers. Hence, the investigated structures cannot be characterized as roughness structures. The minimum C_d value for dimples is lower than the present values; however the measured C_d values presented in Fig. 32 seem to remain constant over a wide range of Re-numbers than the dimples or at least do not exhibit the same trends (clear minima of C_d at one Re) as the dimpled surface. The behavior of outwardly curved structures is however closer to the dimples than the roughened surfaces in post critical regime, which suggests that the mechanism of drag reduction for hexagonal bumps can be similar to that of dimples. On the other hand, a hexagonal bump does not resemble a dimple in shape and structure, whereas a hexagonal dimple does. Hence, the possibility of a totally different mechanism cannot be overruled. A nearly unchanged drag coefficient over a wide range of Reynolds numbers is probably due to the fixed angle of separation line in contrast to a roughened cylinder, whose separation line shifts upwards at higher Reynolds numbers.

6.1.2 Velocity profiles in the wake region

To validate the observed effect of drag reduction, velocity measurements in the wake region were performed using hot wire anemometry for a Re-number of Re = 2.3 x 10^5. The velocity profiles were obtained by placing the hot wire probe at a distance of 45 cm at the rear of the axis of the cylinder which corresponds to a ratio of x/D = 3. Fig. 33 and Fig. 34 illustrate the mean and r.m.s velocities vs. y/D, where y is the distance perpendicular to the axis of cylinder at a horizontal distance of x/D = 3 to the cylinder and D is the diameter of the cylinder.

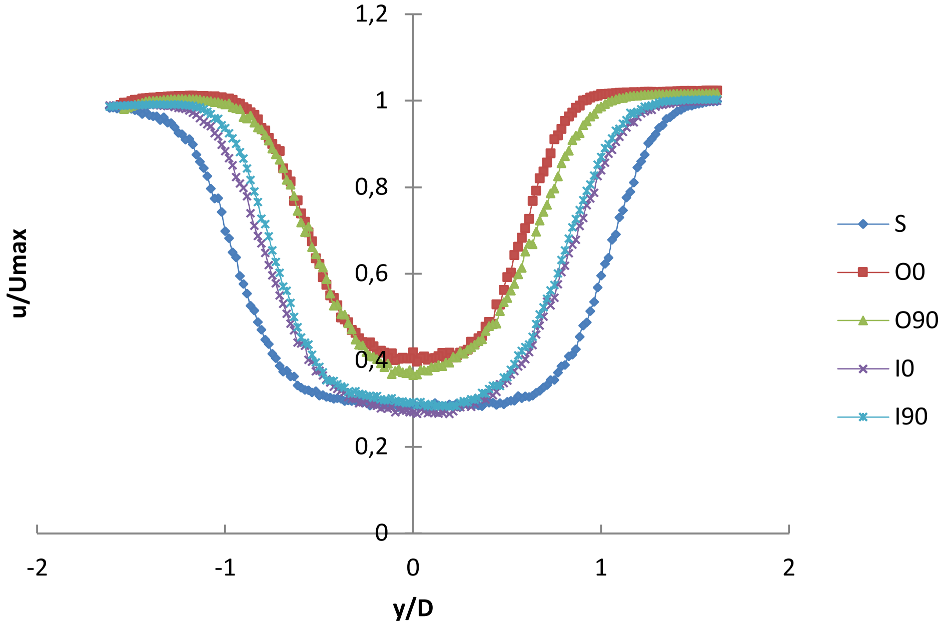

Fig 33: Variation of Mean velocity profiles behind the cylinders for Re=2.3x10^5

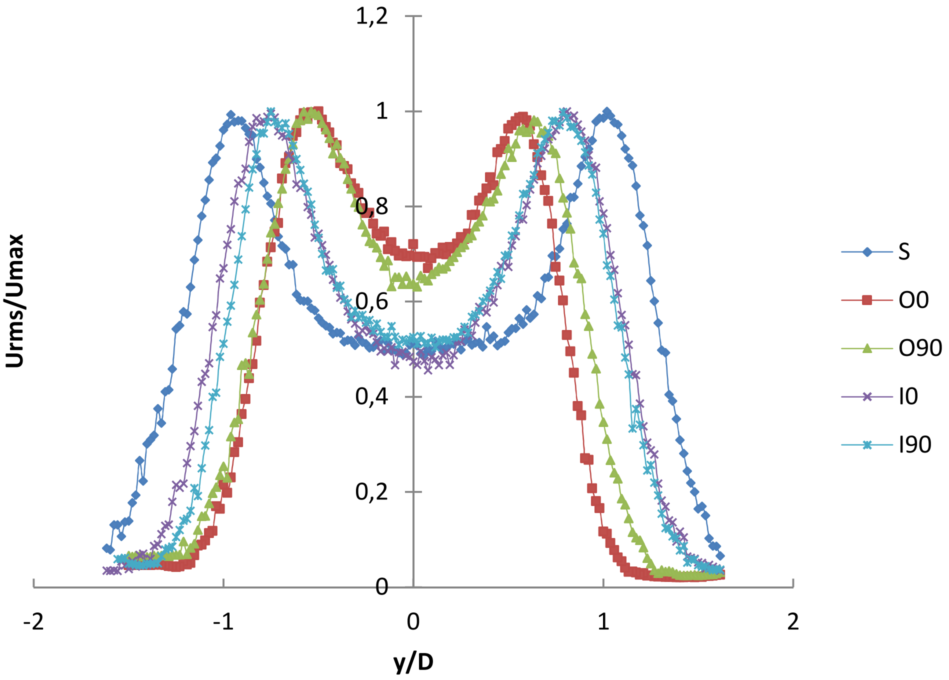

Fig 34: Variation of rms velocity profiles behind the cylinders for Re=2.3 x 10^5

As expected, the configuration O90 and O0 have the smallest wake region (Fig. 33) compared to the others confirming the evidence of their lowest drag coefficients. Symmetry of these wake regions indicates the absence of any forces other than the drag force. A slight difference in minimal turbulence intensities at positive and negative y/D lies within the measurement uncertainty of the ratio u_{rms}/U_{max}, which is ±10.1%.

The patterns on the surface disturb the pressure distribution around the cylinder in such a way that the separation process is altered proving them a suitable passive control. The above shown velocity profiles do not provide any information about the nature of the flow above the surface of the cylinders and hence the mechanism of drag reduction. Nevertheless, a smaller wake region definitely suggests that the separation process has been altered. Whether the separation is caused by a transition from laminar to turbulent boundary layer, is yet unanswered. Therefore, it is essential to investigate the separation process to comprehend the mechanism of drag reduction. In following, results of two different visualization techniques are described to shed light on the separations process.

6.1.3 Location of flow separation

Smoke flow visualization was carried out at a Reynolds number of 2.3 x 10^5 respectively. The smoke follows the air and traces its path when enlightened via light sheet. A noticeable delay in separation was observed for the configurations O90 and O0 having the smallest drag coefficient among all. An estimated position of the flow separation has been marked with the help of an arrow (Fig. 35). The positions of the separation arrows in the configurations I90 and I0 are very much near to the one on smooth cylinder indicating the fact that their drag coefficients do not differ significantly from the drag coefficient of S. The smoke flow visualization results clearly validate the drag coefficient measurements and give an explanation for the observed phenomenon i.e. the delay in separation process occurring on the surface of the cylinder at a lower Reynolds number than the critical Reynolds number of a smooth cylinder is mainly responsible for the reduction in drag coefficient of the cylinders.

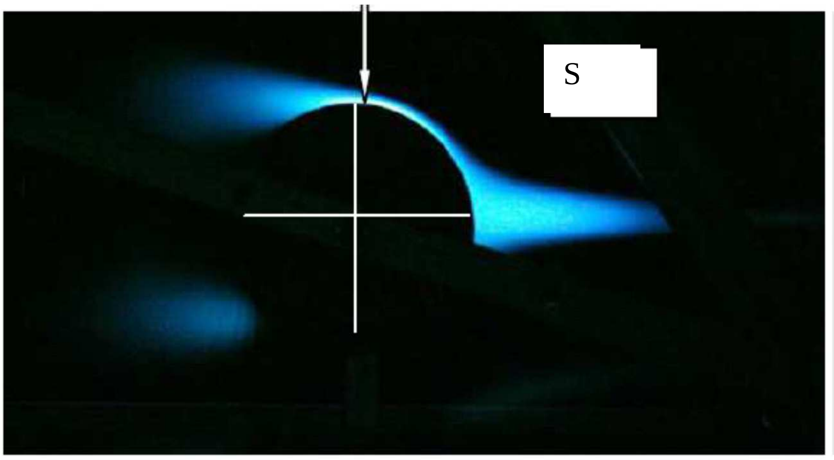

Fig 35-a: location of separation points on structured cylinders

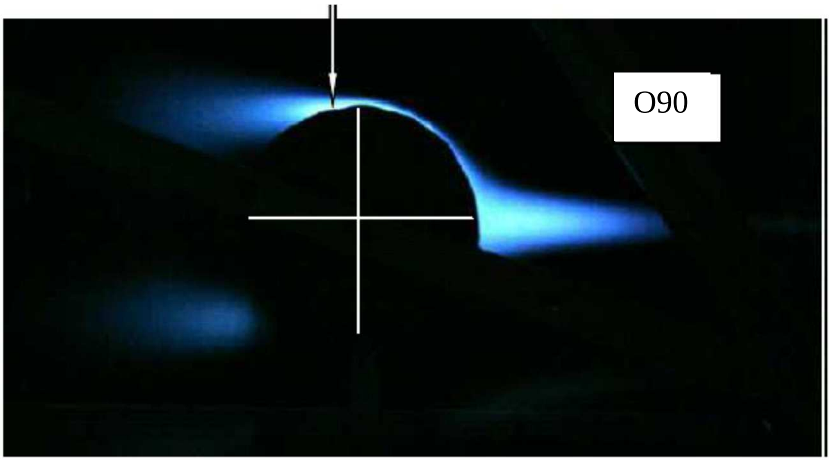

Fig 35-b: location of separation points on structured cylinders

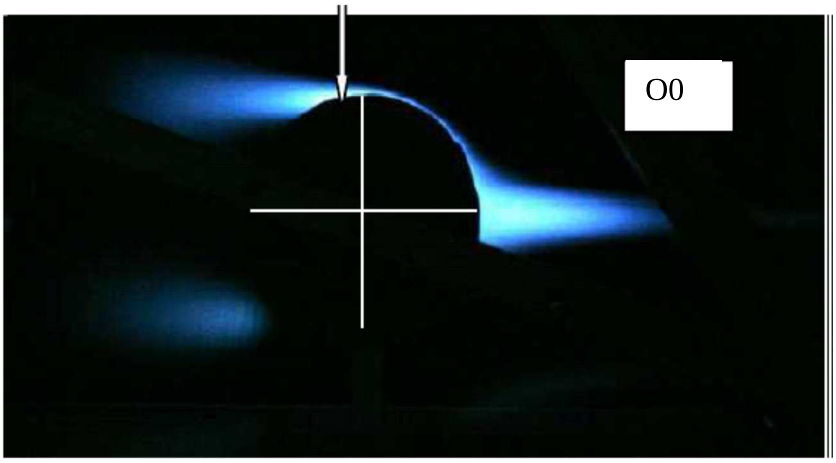

Fig 35-c: location of separation points on structured cylinders

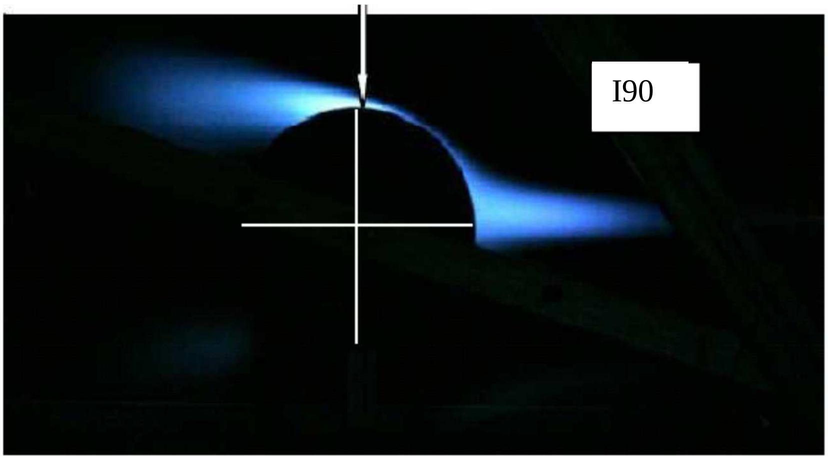

Fig 35-d: location of separation points on structured cylinders

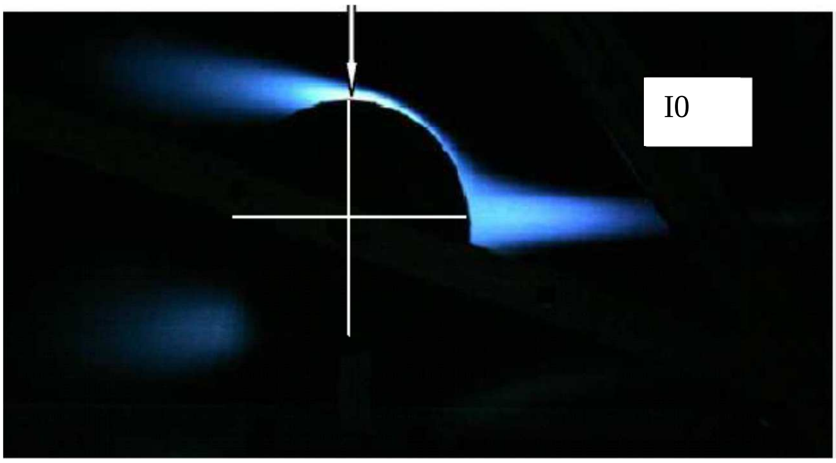

Fig 35-d: location of separation points on structured cylinders

6.1.4 Flow visualization on the surfaces of cylinders

Fig. 36 shows surface oil flow patterns for all the investigated configurations of $k/D = 1.98 \times 10^{-2}$ for a Reynolds number of 2.3×10^5. The flow direction is from right to left. It is commonly known that the powdered titanium dioxide leaves its traces wherever a separation or transition of flow takes place enabling the observer to visualize the flow on the surface. The areas with a low concentration of titanium dioxide are generally interpreted as a high shear force area, whereas a higher concentration or accumulation of titanium dioxide indicates a separation or transition of the flow.

The bright line in Fig. 36 (S) indicates the laminar separation of flow over smooth cylinder. This separation line lies at about 85°. A clear trace of titanium dioxide and hence the separation could be visualized because of the smoothness of the surface. On the other hand, the patterns create extreme difficulties for oil film in marking a clear separation or transition of the flow especially for the cylinders with patterns pressed inwards (I90 and I0). A recurring series of bright lines nearly at the middle of the hexagon at about 75° on O90 represent a local separation. This local separation triggers a shear layer instability causing the flow to reattach to the surface where the hexagon ends.

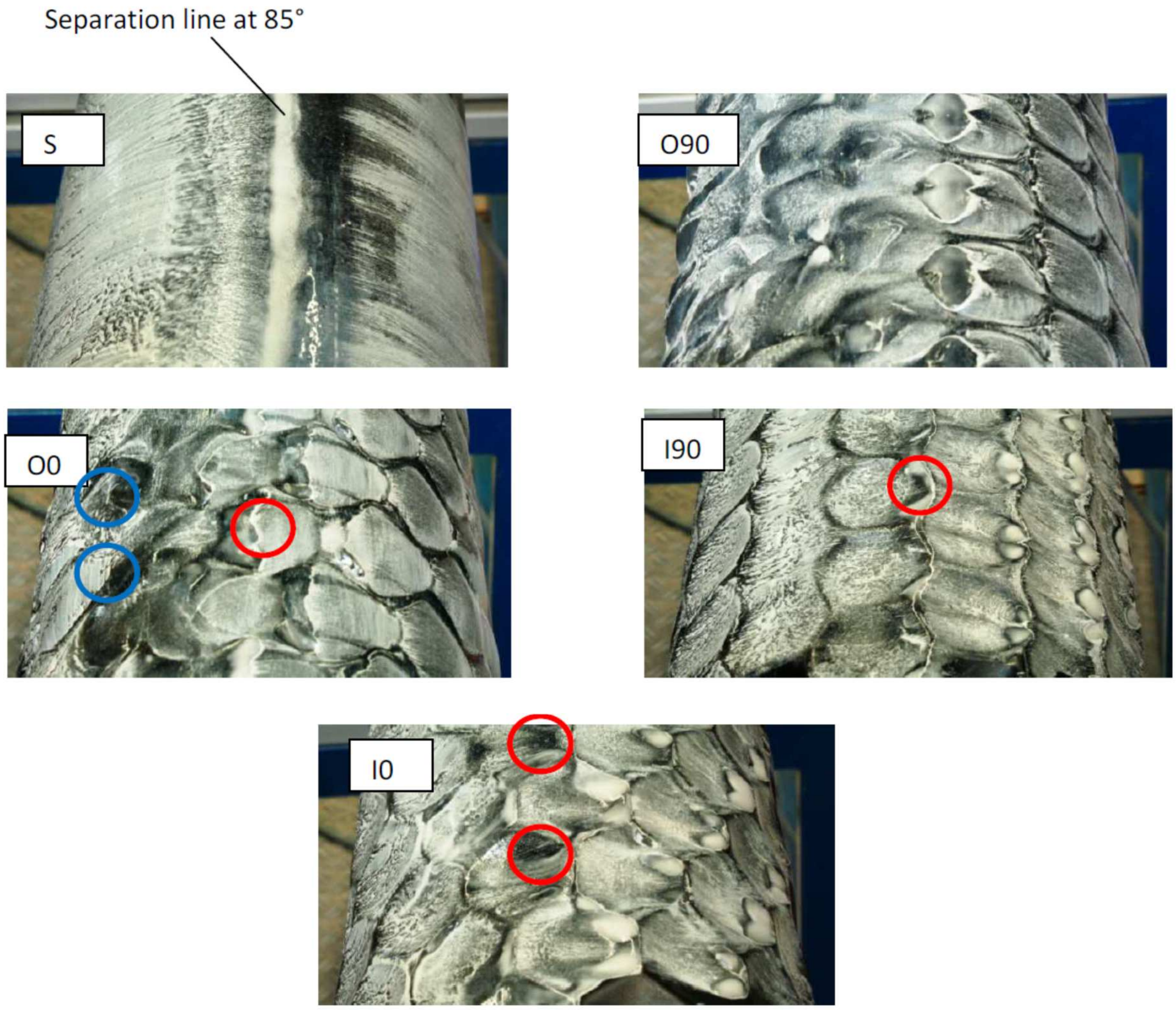

Fig 36: Surface oil film patterns on structured cylinders

Oval shaped separation bubbles having a size of half the hexagon can be seen in Fig. 36 (O90). The flow between two parallel hexagons does not separate there but at the middle of the next series of hexagons. These local separations delay the main separation, which finally occurs at about 110° and 115°. A similar process of local separation (red circle), reattachment and main separation (blue circle) can be observed for the configuration O0. Some part of the flow undergoes secondary separation at about 75° and the rest at 85° delaying the main separation. Oil flow patterns for the configurations I90 and I0 do not depict a clear picture of flow. It seems, that the dimple like hexagonal patterns on I90 cause the flow to separate without any significant delay in local or main separation. The angle of final separation point (red circle) for I90 shows minor deviations from the smooth cylinder. Whereas, some dark areas (red circle) at about 95°, representing a higher shear stress region, can be observed on the oil flow pattern of I0, which means that some part of the flow remains attached to the surface till this region resulting in a lower drag coefficient as compared to the smooth one. Flow undergoes successive local separations exhibited by the bright spots on the surface. Despite these local separations, main separation is not delayed that much as for the configurations O90 and O0 confirming their higher drag coefficient. To consolidate the interpretations made through oil-flow patterns, near wall measurements were performed on O90, O0 and I0. Velocity profiles above the surface were recorded with the help of hot wire anemometry. This quantitative visualization using hot wire anemometry helped not only to understand the flow over patterns, but also to locate the position of boundary layer separation precisely. The velocity measurements were performed in the radial direction at two different locations a and b along the circumference of the cylinder (Fig. 37)

6.1.5 Streamwise velocity measurements

A quantitative analysis of the boundary layer at a Reynolds number of 2.3 x 10^5 was performed for the configurations O90, O0 and I0 using hot wire anemometry as they possess the lowest values of drag coefficients among all the investigated configurations. The purpose of these investigations is to analyze the flow over the surface of the cylinders and to establish the fact that the reduction in drag is caused by the delayed separation induced by the successive separations and reattachments.

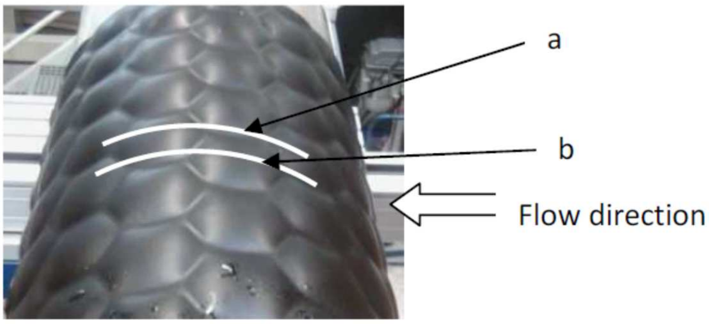

Fig 37: Measurement locations on patterns

The measurements were performed for two different locations along the length of cylinder (Fig. 37).

Fig. 38 shows the velocity profiles above the surface of the cylinders with patterns of k/D = 1.98 x 10^{-2}. Although, the measurements made by a single wire probe cannot represent the true streamwise component of the velocity because the velocity components do not remain much parallel to the surface near separation but the variations in the measured mean and r.m.s velocities clearly articulate the flow before and after separation.

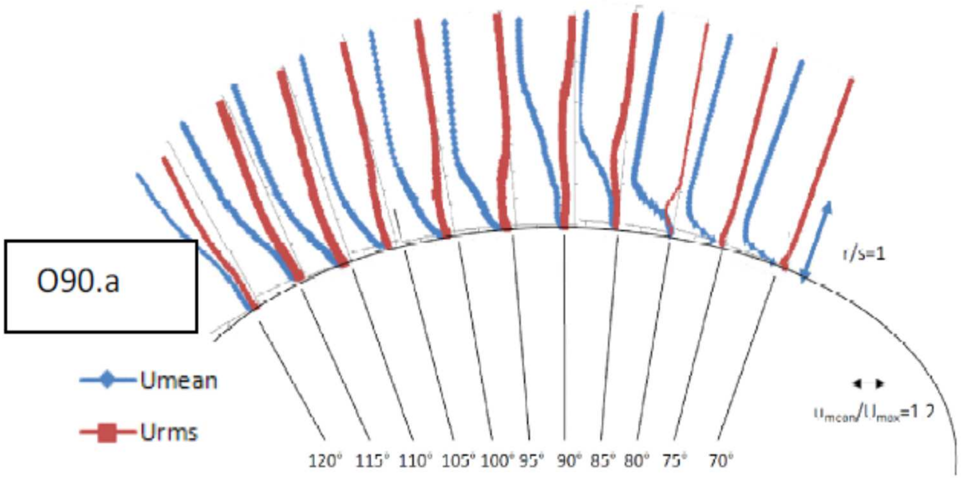

Fig 38-a: Profiles of the mean velocity and r.m.s velocity above configurations O90 (a) for Re = 2.3 x 10^5, r/s=radial position/pattern height

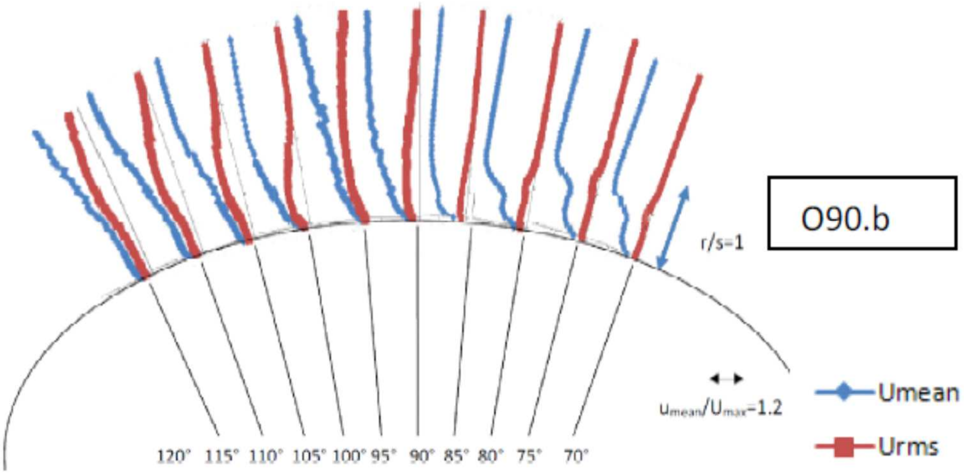

Fig 38-b: Profiles of the mean velocity and r.m.s velocity above configurations O90 (b) for Re = 2.3 x 10^5, r/s=radial position/pattern height

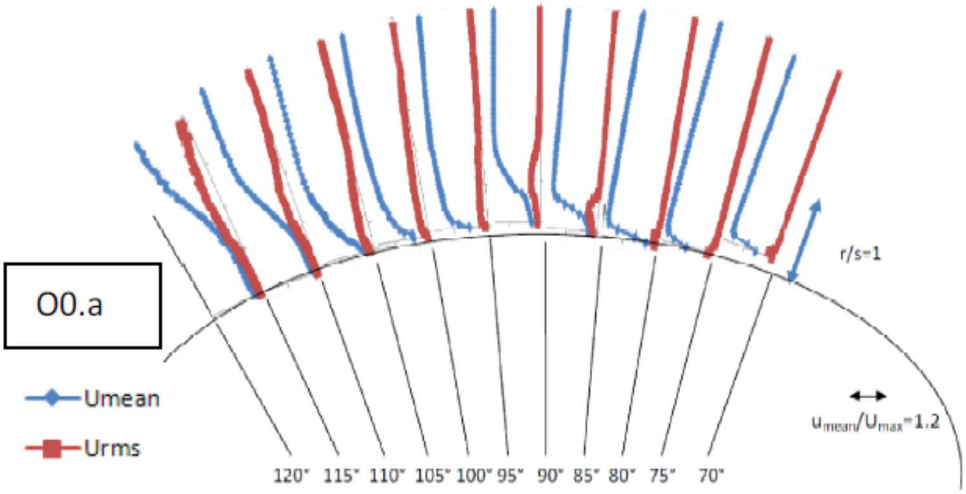

Fig 38-c: Profiles of the mean velocity and r.m.s velocity above configurations O0 (a) for Re = 2.3 x 10^5, r/s=radial position/pattern height

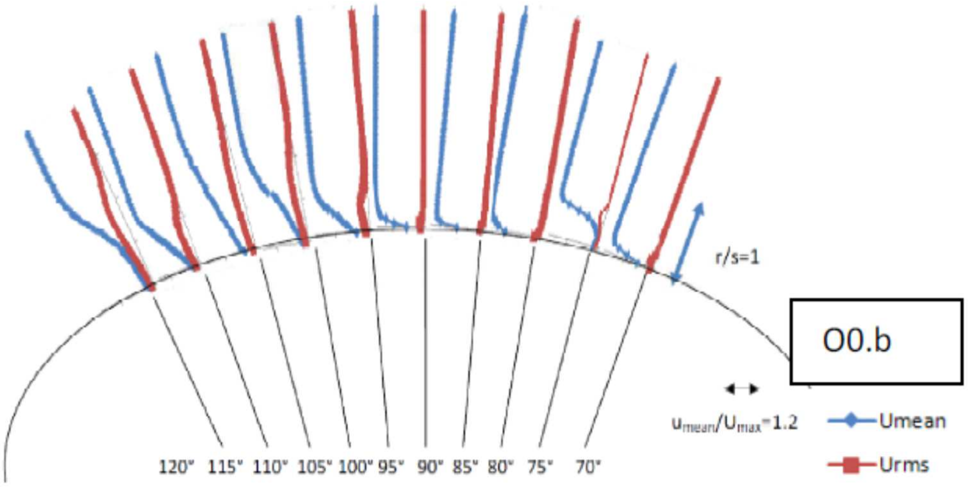

Fig 38-d: Profiles of the mean velocity and r.m.s velocity above configurations O0 (b) for Re = 2.3 x 10^5, r/s=radial position/pattern height

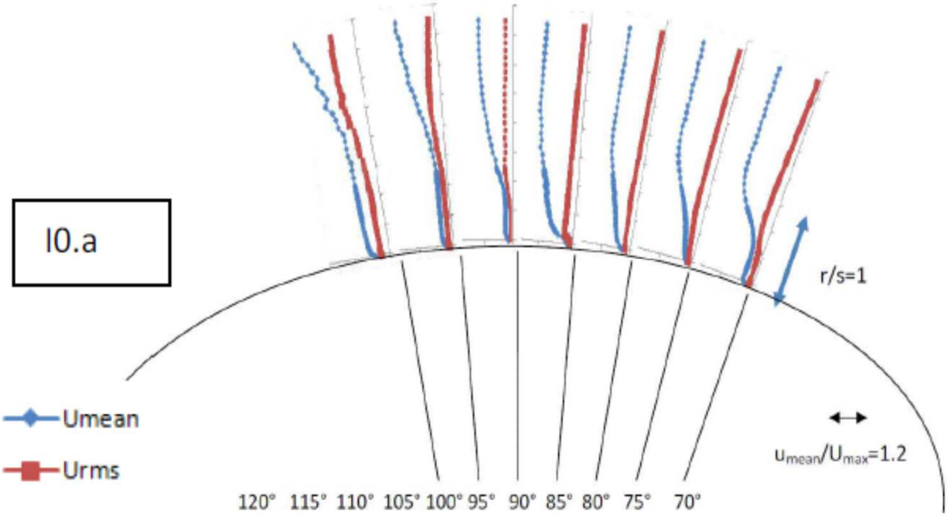

Fig 38-e: Profiles of the mean velocity and r.m.s velocity above configurations I0 (a) for Re = 2.3 x 10^5, r/s=radial position/pattern height

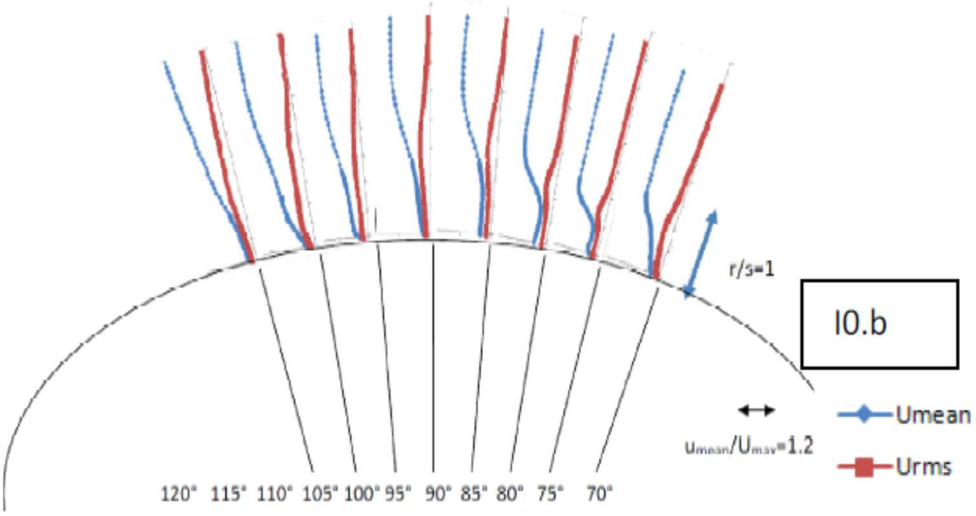

Fig 38-f: Profiles of the mean velocity and r.m.s velocity above configurations I0 (b) for Re = 2.3 x 10^5, r/s=radial position/pattern height

An estimated position of boundary layer separation can be identified by considering near wall velocity profiles. Note that a flow separation is detected from the constant near-wall velocity profile along the radial direction when a type-I hot-wire probe is used. Figure 38-a shows that the

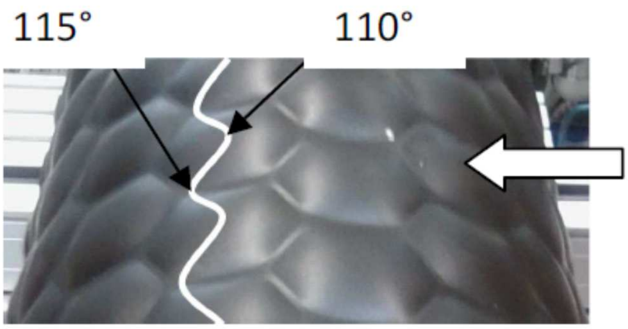

Fig 39: Flow separation indicated by a zig zag line on O90

flow over configuration O90 starts separating at 80° owing to the disturbance caused by the hexagonal bump. It can be observed that u´ increases rapidly destabilizing the shear layer near the surface and energizing the flow. The observation is validated by the energy spectra of the flow at locations 70° and 100° in Fig. 40. The flow reattaches at 100° with higher momentum and hence can withstand the adverse pressure gradient. The reattached flow leaves a separation bubble behind it and remains attached to the surface till 115° where the final separation takes place. On the other hand, measurements taken at location b shifted half the length of the hexagon towards right from the location a show that the boundary layer has already separated at 70° and reattaches at 90°. Final separation takes place at 110°. This indicates that the position of transition and final separation points vary in span wise direction. Hence, the separation cannot be defined as a single line at a particular angle but a wave along the length of the cylinder with its crest at 110° and trough at 115° (Fig. 39).

For the configuration O0.a, first separation takes place at 80° and reattachment at 95°. The flow separation occurs finally at 110°, whereas the flow over the same configuration but at different location b separates partially at 75° and reattaches at 100°. After a separation and a reattachment the boundary layer completely dissolves at 115°. By comparing the velocity profiles of outwardly curved configurations with each other, it can be observed that the mean transition line (defined as the mean of crest and trough) for O0 (97.5°) is a little further upstream than the O90, which is 95°. However, the mean separation line (112.5°) remains same for both the configurations.

A significant downstream shift in the separation points can be observed for I0, where the final separation takes place at 90° and 105° at locations a and b. This downstream shift of separation points results in an increase in the drag coefficient of the cylinder with inwardly curved structures. A similar mechanism of drag reduction for a dimpled sphere has been devised by Choi [9], for periodic blowing and suction by S. Jeon et.al [12] and for trip wire by K. Son et .al. [14] when its drag coefficient becomes minimized. It was illustrated that the dimples produce disturbances causing a partial separation at 70°. The flow reattaches to the surface at 90°, and finally separates at 110° resulting in a significant decrease in drag coefficient.

6.1.6 Energy spectra of the flow over cylinders

It has been confirmed that a delayed final separation induced by a partial separation and a separation bubble takes place above the surface of the cylinders. Based on these observations, it can be hypothesized that the energy is imparted to the flow from the instability in partially separated shear layer owing to the disturbances caused by the hexagonal structures. A higher energy flow is able to withstand the adverse pressure gradient resulting in a delayed flow separation. Energy spectra of the flow before and after partial separation (location of partial separation can be deduced from Fig. 38) is plotted in Fig. 40. The curves clearly vindicate the previously described hypothesis articulating the behavior of the flow at respective locations. The energy of the flow at 100° is much higher than the flow at 70° especially at higher frequencies. At this stage, it can confidently be said that the boundary layer between 80° and 100° represents the characteristics of a turbulent boundary layer, i.e. thick boundary layer flow, a fully mean velocity profile near the wall and broad band energy spectrum. A similar mechanism of drag reduction is responsible for other configurations. Vortex shedding from the surface of structured cylinders is treated in the next section.

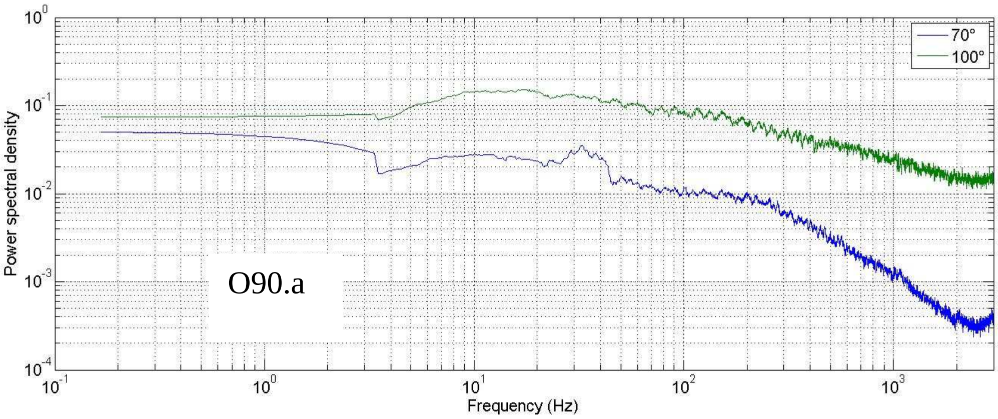

Fig 40-a: Energy spectra of the flow over O90.a before (70°) and after partial separation (100°) at Re = 2.3 x 10^5

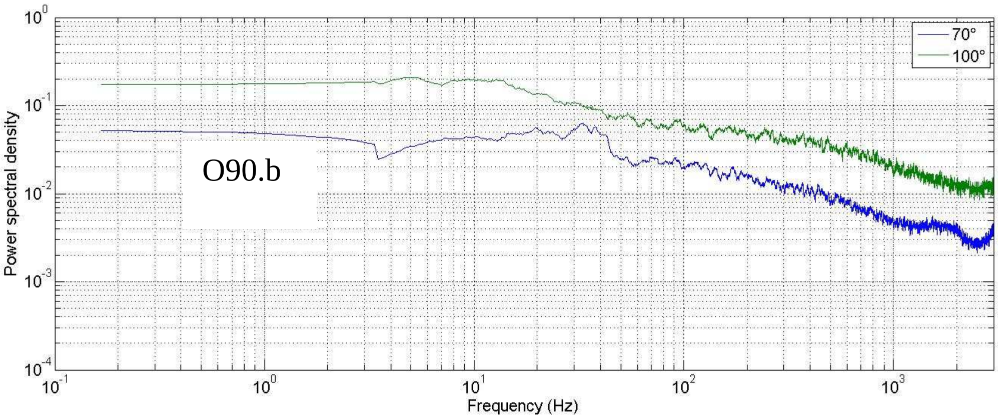

Fig 40-b: Energy spectra of the flow over O90.b before (70°) and after partial separation (100°) at Re = 2.3 x 10^5

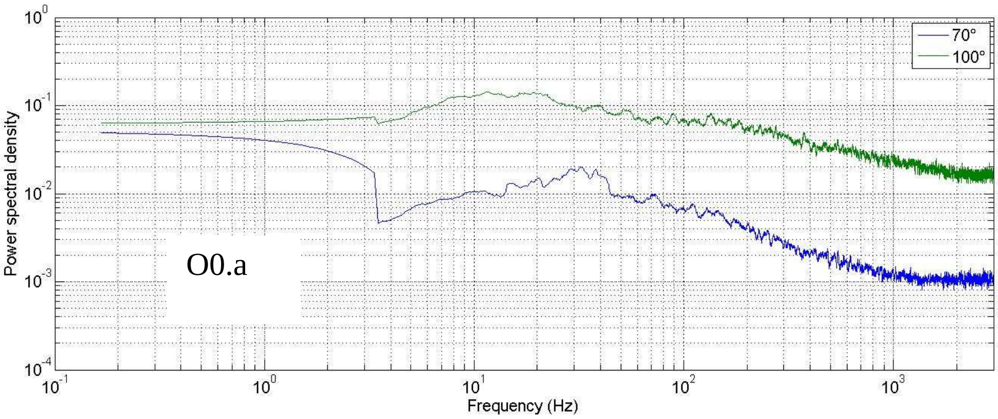

Fig 40-c: Energy spectra of the flow over O0.a before (70°) and after partial separation (100°) at Re = 2.3 x 10^5

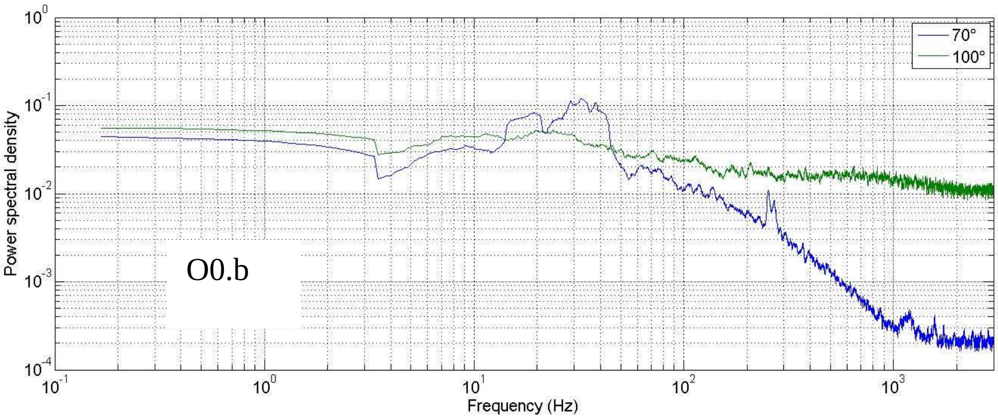

Fig 40-d: Energy spectra of the flow over O0.b before (70°) and after partial separation (100°) at Re = 2.3 x 10^5

6.1.7 Vortex shedding

The Vortex-shedding frequencies in the wake region of investigated circular cylinders caused by the periodic separation of the flow from the surface were also investigated. The investigations were performed for four different Reynolds numbers. A peak in each figure identifies the vortex-shedding frequency with an uncertainty of ±3 Hz present in the wake region of the cylinder.

Vortex shedding frequency increases with increasing Reynolds number for all the configurations illustrated in Fig. 41. The interesting fact to know here is that the vortex-shedding frequency of the flow at a particular Reynolds number for different configurations does not change significantly. It seems that the shear layer coming from the surface of the structured cylinder does not get irregular or stronger as in case of a dimpled cylinder or a smooth cylinder at higher Reynolds numbers (Fig. 11). The vortex generation by the structured cylinder remains steady even at critical Reynolds number.

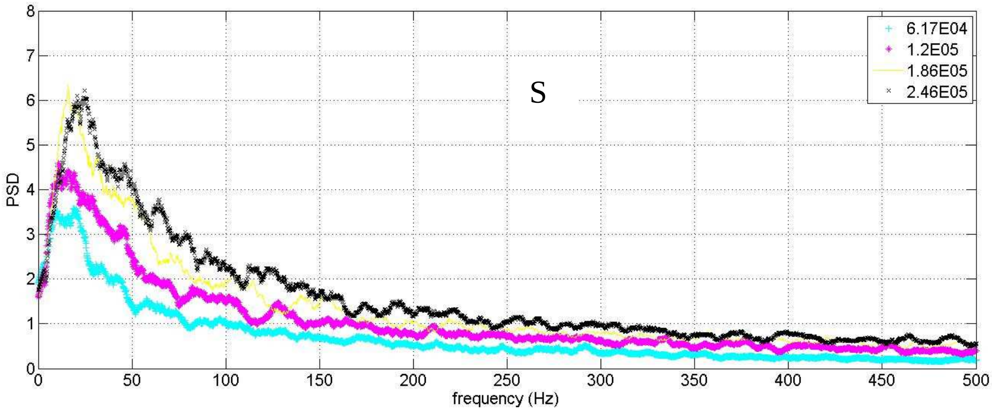

Fig 41-a: Power spectrum of the flow over S at four different Reynolds numbers, (PSD = Power Spectral Density)

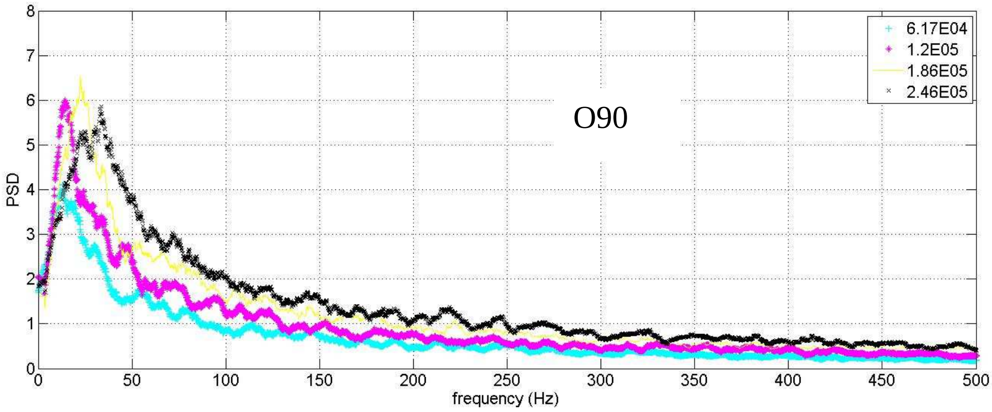

Fig 41-b: Power spectrum of the flow over O90 at four different Reynolds numbers, (PSD = Power Spectral Density)

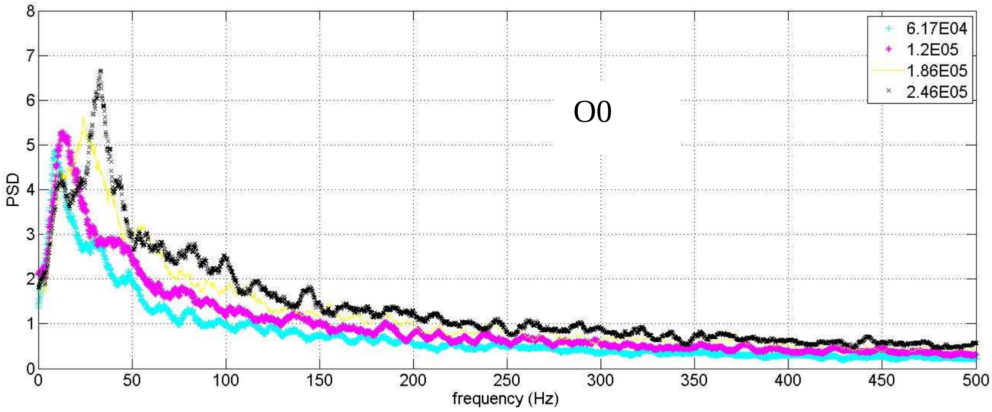

Fig 41-c: Power spectrum of the flow over O0 at four different Reynolds numbers, (PSD = Power Spectral Density)

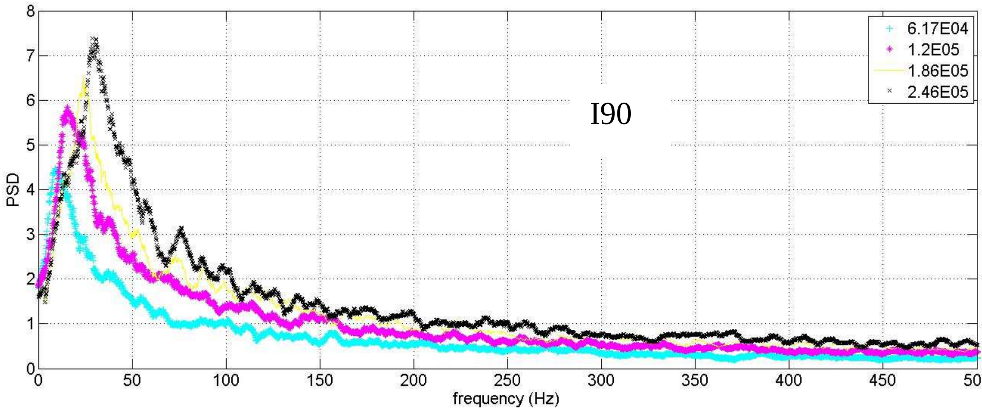

Fig 41-d: Power spectrum of the flow over I90 at four different Reynolds numbers, (PSD = Power Spectral Density)

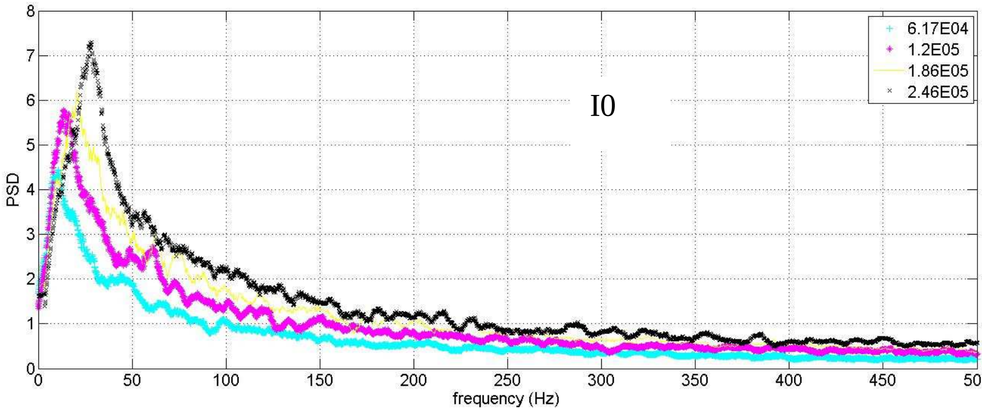

Fig 41-e: Power spectrum of the flow over I0 at four different Reynolds numbers, (PSD = Power Spectral Density)

The Strouhal number ($Str = fD/U_\infty$), where f is the vortex shedding frequency, D the diameter of cylinder and U_∞ the free stream velocity, is plotted against Reynolds numbers with an uncertainty of ±1.8% for Re = 2.46 x 10^5 and ±7% for Re = 4.17 x 10^4 in Fig. 42. The Strouhal number of the structured cylinders for the investigated Reynolds numbers seems not significantly be different from the smooth cylinder implying that the vortex-shedding does not get stronger even at critical Re numbers, i.e. where a significant drop in drag coefficient is observed. For a dimpled cylinder on the other hand the vortex-shedding becomes stronger at critical Reynolds number [2] and get weaker and irregular for a smooth cylinder as the flow approaches critical flow regime and a sudden increase in Strouhal number is observed (Fig. 11). Based on these observations, it can be concluded that a circular cylinder with hexagonal patterns would not only offer less resistance to the flow but also be less vibrant in contrast to a dimpled cylinder.

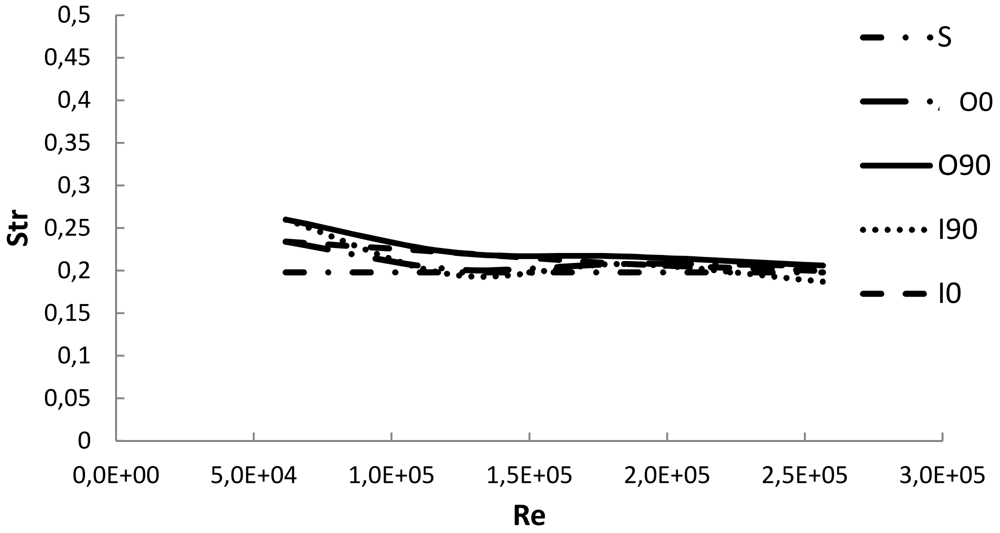

Fig 42: Strouhal number vs Reynolds number for investigated cylinders

6.2 Structured plates

6.2.1 Non dimensional velocity profiles

Fig. 43 illustrate the measured velocity profiles at the front and rear of flat and structured plates together with the law of wall and logarithmic law. The hot wire probe used to measure the velocities was adjusted at a distance of 30 µm from the test surface using a microscope. Measured velocities in the sub-layer region seem to be higher than the actual velocities. This effect can be observed up to $y^+ = 5$, where the viscous sub-layer of a turbulent boundary layer starts to transform into a puffer layer. The observed effect near the wall is subjected to the thermal influence of the hot wire probe. As the hot wire probe comes very close to the surface, the heat from the hot wire probe not only flows into the air but also into the test surface resulting in an increased flow of electrical current. A larger current through the hot wire sensor results in a higher sensed velocity determined by the calibration curve. The hot wire anemometry is therefore not applicable for determination of wall shear stresses by measuring the velocity gradient in the viscous sub-layer of a turbulent boundary layer at least for the present Reynolds numbers.

Shear stress coefficient is hence determined by using Clauser-chart method. Fig. 43 shows the measured velocity profiles at the front and rear of the structured plates plotted with the logarithmic law using already mentioned von Ka´rma´n constant. There are a number of factors which directly influence the correct estimation of shear stress coefficient through Clauser-chart method i.e. Reynolds’s number, accuracy of wall position, fitting of measured data into log law and most importantly the extent of wall distance in which the log law is believed to be valid [67]. The measured data was fitted into the log law by visual inspection and then by least square fitting method which is found to be the most accurate way of determining shear stress coefficient [68]. The logarithmic region ranges from $y^+ = 30$ to $y^+ = 100$ for front and from $y^+ = 30$ to $y^+ = 200$ for the velocity profiles measured at the rear of structured plates. The upper (less than $0.15 y_{max}/\delta$) and lower limits were chosen by considering the findings of Sigalini et.al [68] in order to keep the uncertainty of the chosen Von Ka´rma´n constant at its minimum for the present Reynolds numbers. The turbulence intensity is highest in the puffer layer in a region of $5 < y^+ < 30$ (Fig. 44).

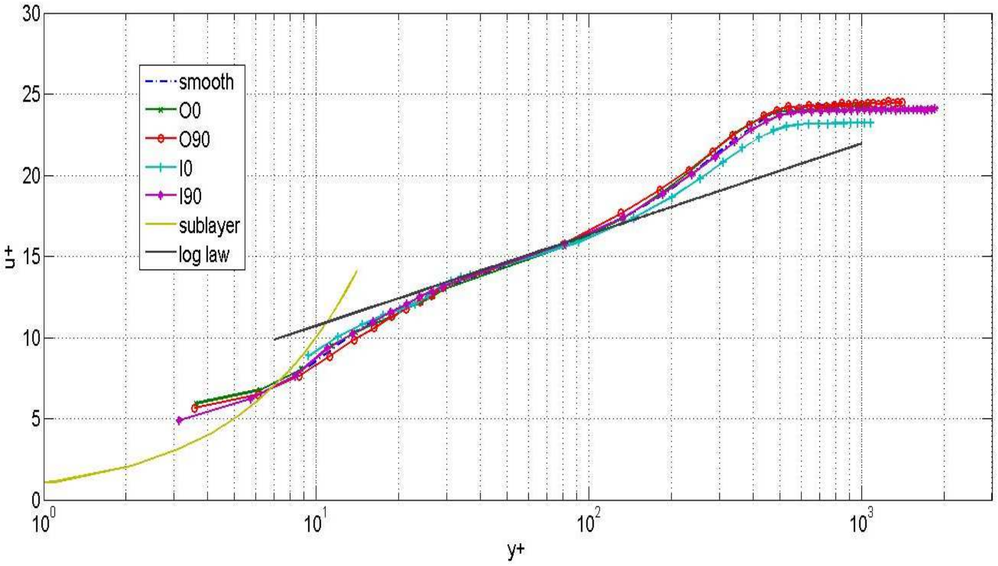

Fig 43-a: Dimensionless mean velocity profiles at front of the test plate for the Reynolds number $Re_x = 5.34 \times 10^5$

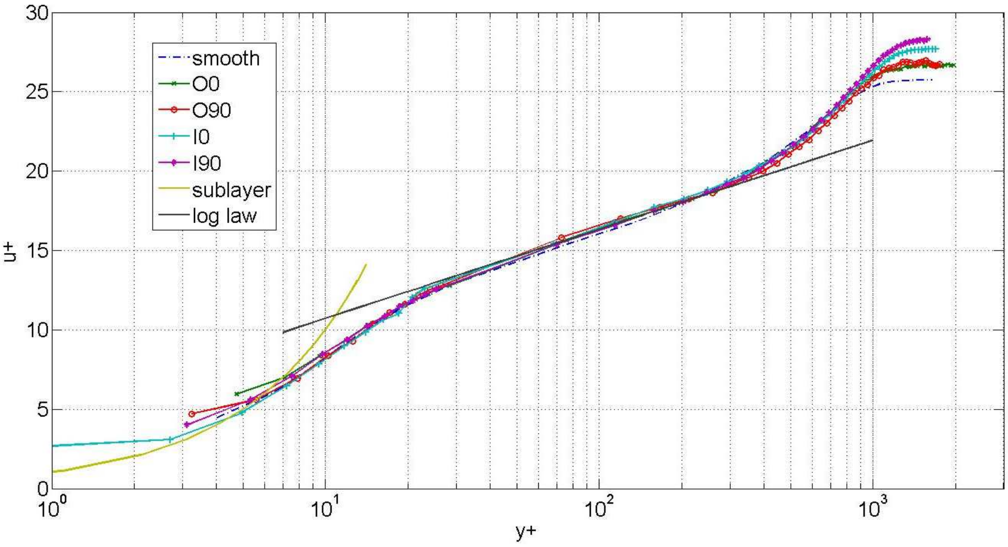

Fig 43-b: Dimensionless mean velocity profiles at rear of the test plate for the Reynolds number $Re_x = 7.99 \times 10^6$

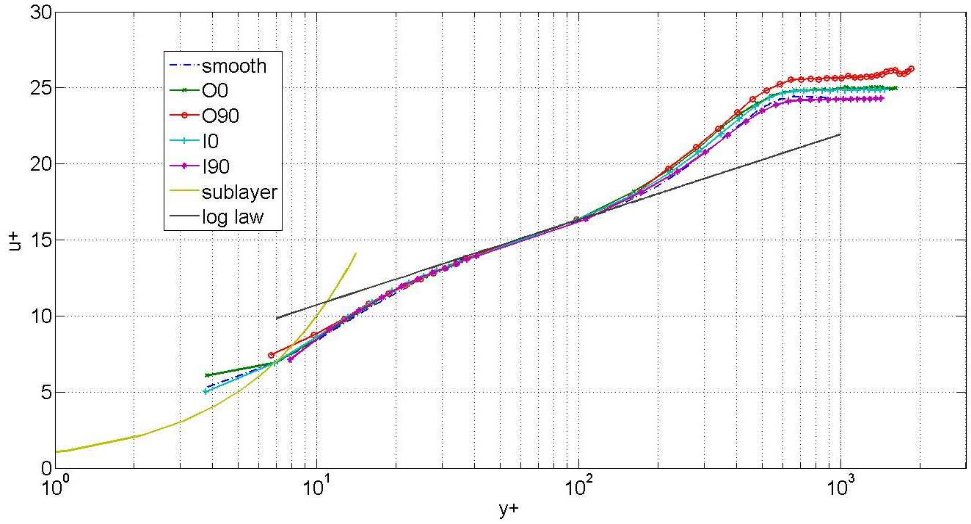

Fig 43-c: Dimensionless mean velocity profiles at front of the test plate for the Reynolds number $Re_x = 6.7 \times 10^5$

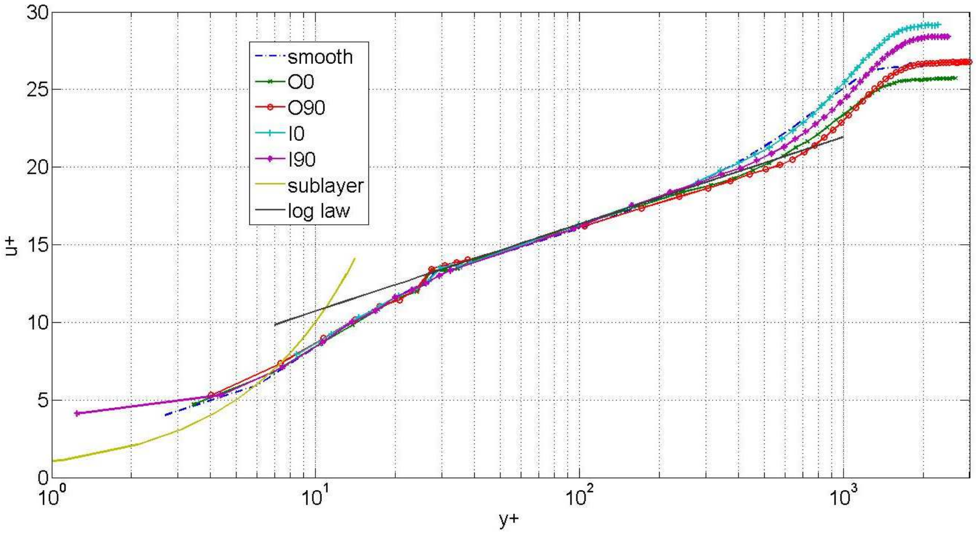

Fig 43-c: Dimensionless mean velocity profiles at Rear of the test plate for the Reynolds number $Re_x = 10.04 \times 10^6$

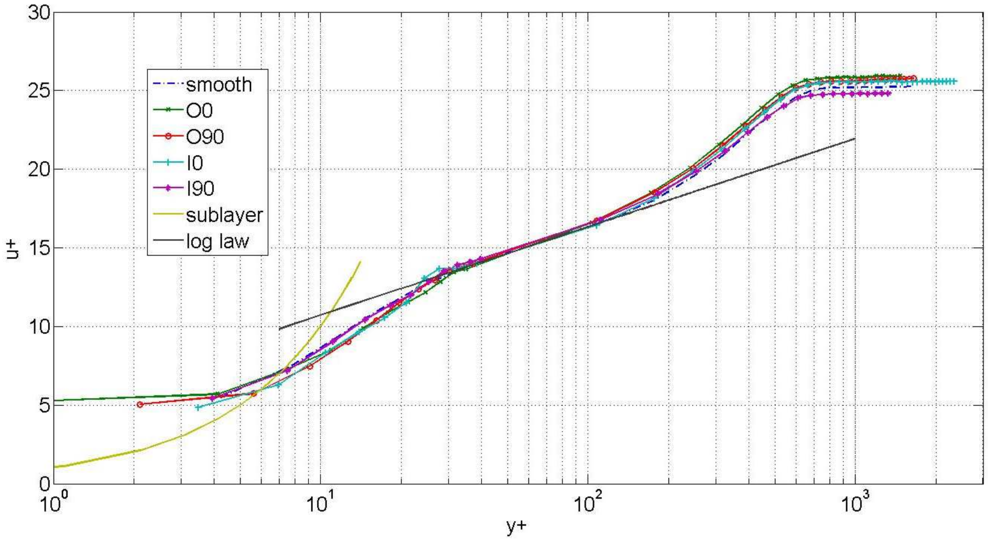

Fig 43-d: Dimensionless mean velocity profiles at Front of the test plate for the Reynolds number $Re_x = 7.54 \times 10^5$

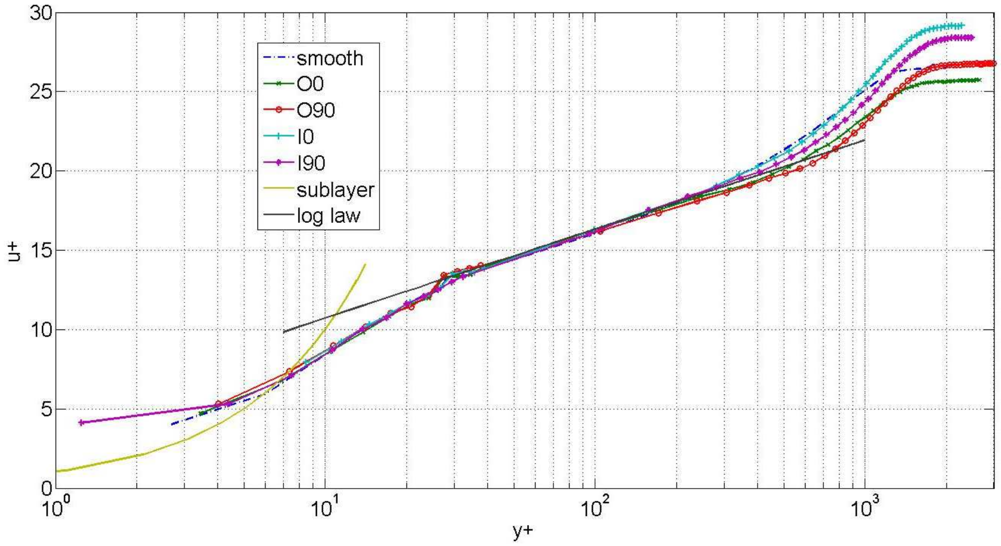

Fig 43-e: dimensionless mean velocity profiles at rear of the test plate for the Reynolds number $Re_x = 11.27 \times 10^6$ (Rear)

In Fig. 44, the effective velocity $\left(u_{eff} = \sqrt{\overline{u'^2}}\right)$ normalized with the shear stress velocity u_τ against y^+ is displayed. The maximum of the curves for all the investigated Reynolds numbers is found between $y^+ = 15$ and $y^+ = 17$. At the rear of the Test plates where the Reynolds number is significantly high, the curve flattens as the velocity profiles stretches over a wider range of y^+. The velocity profiles of the configurations I0 and I90 tend to flatten more than O0 and O90 and in some cases it is hard to identify a clear peak or a maximum but a region of higher turbulent intensities is obvious. Secondly, diverse values of shear stress velocities and hence the shear stress coefficients of the investigated configurations at a particular Reynolds number are also visible. The configuration 'smooth' possess the highest value of u_τ among all the investigated configurations. A similar behavior can be observed at other Reynolds numbers.

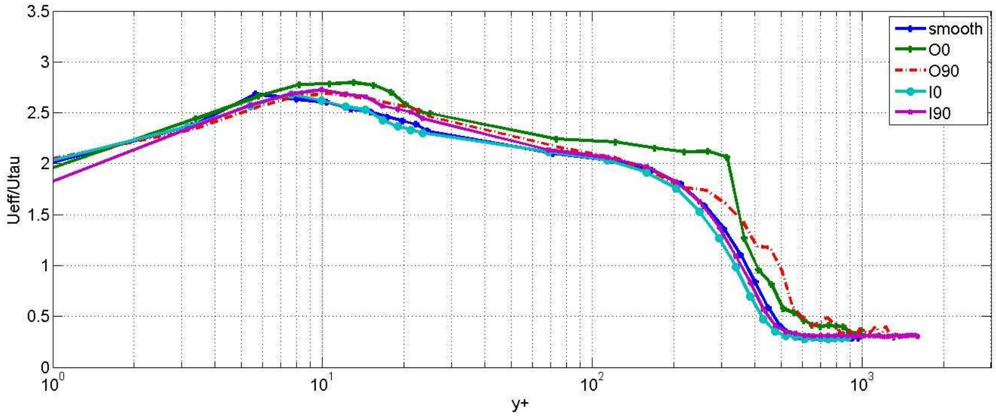

Fig 44-a: Dimensionless r.m.s velocity profiles at front of the test plate for the Reynolds number $Re_x = 5.34 \times 10^5$

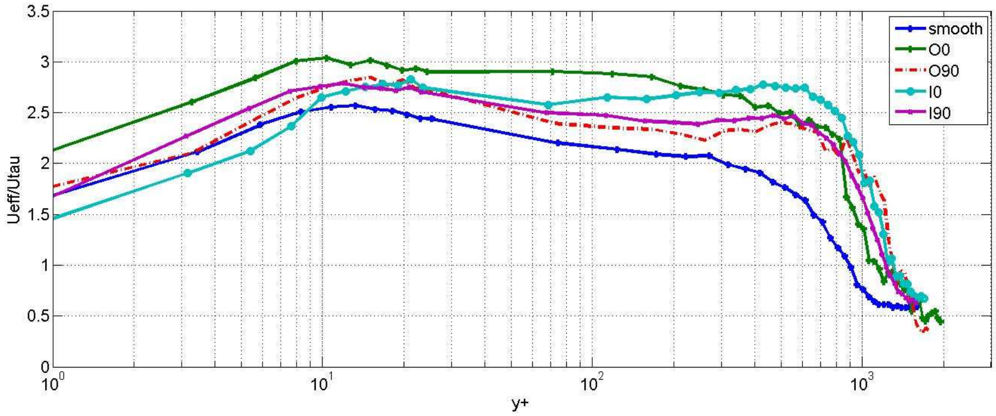

Fig 44-b: Dimensionless r.m.s velocity profiles at rear of the test plate for the Reynolds number Re_x = 7.99 x 10^6

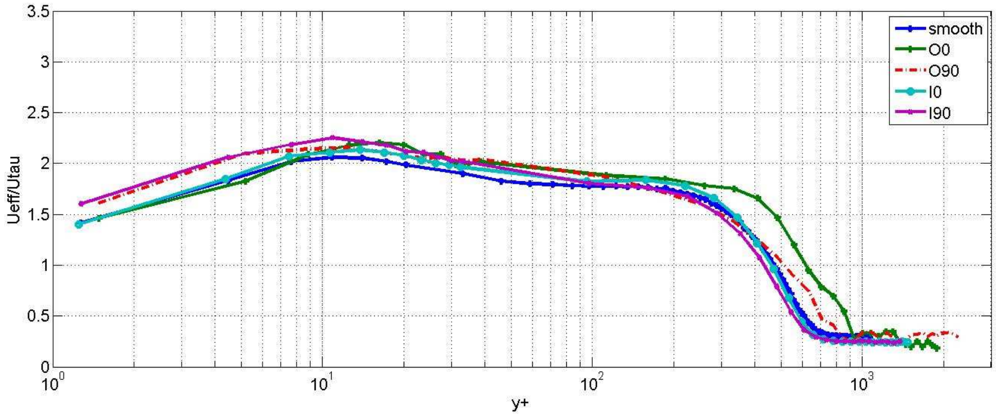

Fig 44-c: Dimensionless r.m.s velocity profiles at front of the test plate for the Reynolds number Re_x = 6.7 x 10^5

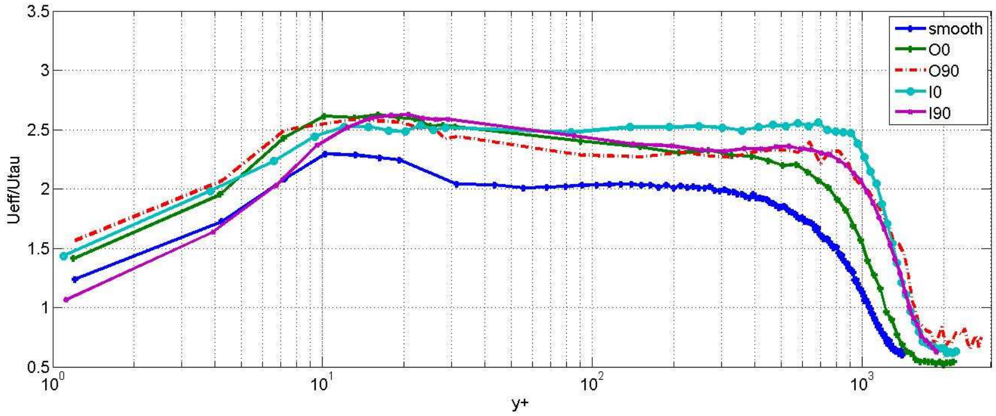

Fig 44-d: Dimensionless r.m.s velocity profiles at rear of the test plate for the Reynolds number Re_x = 10.04 x 10^6

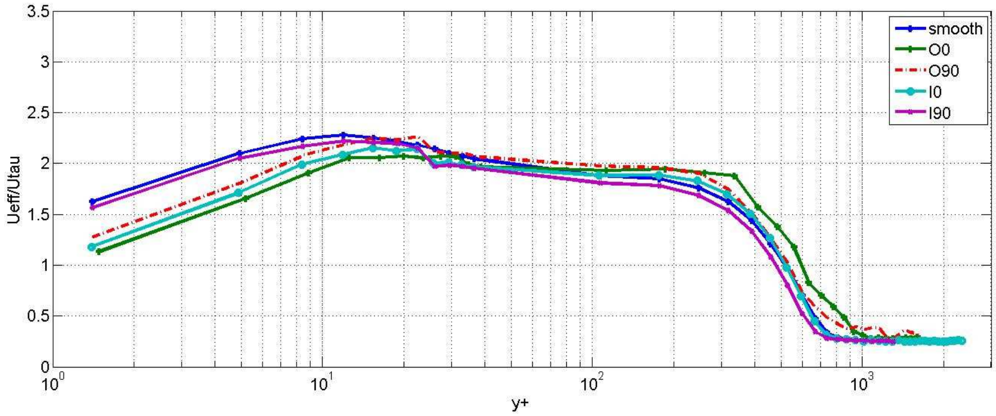

Fig 44-e: Dimensionless r.m.s velocity profiles at front of the test plate for the Reynolds number $Re_x = 7.54 \times 10^5$

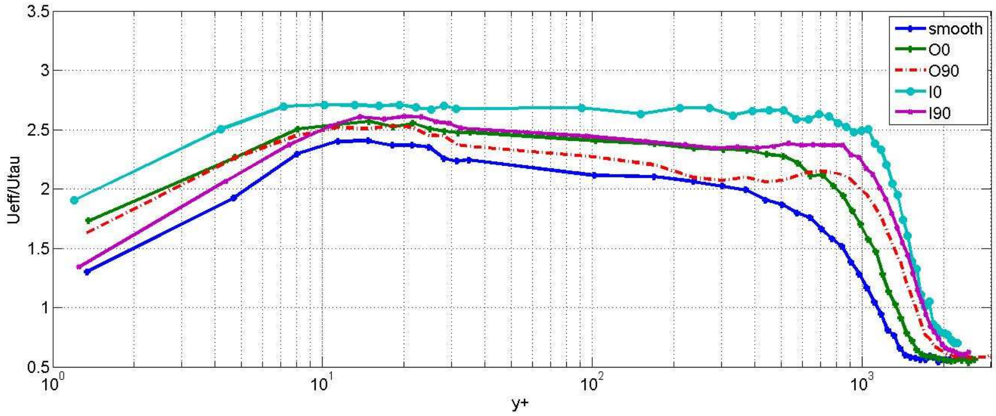

Fig 44-f: Dimensionless r.m.s velocity profiles at rear of the test plate for the Reynolds number $Re_x = 11.27 \times 10^6$

6.2.2 Boundary layer quantities

A summary of experimental results obtained by the measurements at front and rear of the structured plates is presented in Table 4. These include shear stress coefficients (by Oil film Interferometry OFI and Clauser Chart method CL), shear stress velocities, displacement thicknesses (δ_1) and Momentum thicknesses (δ_2) of the boundary layer. A number of observations can be made regarding measurement techniques as well as the nature of the flow over structured plates. The values of shear stress coefficients obtained by the Clauser-chart method seems generally be greater than the values obtained by the oil film interferometry by about 13 %. This difference can be observed for nearly all the investigated Reynolds numbers and configurations confirming the findings of the studies by Kline et al [23], Blackwelder et al [24], Spalart [25], Ong and Wallace [26]). The method of determining the wall shear stress by Clauser-chart and processing of fringe images has already been described in an earlier section. The values of C_f determined by the oil film interferometry are considered to be more accurate because of its independence from the universal log law and Von Ka´rma´n constants. The measurements were performed at three different locations in the span-wise direction to account for any three dimensional effects. The variation in the quantities measured at three different locations was found to be within the accuracy limits of the measurement techniques. The results and the velocity profiles (Fig. 44) reveal that the hexagonal structures thicken the turbulent boundary layer and the boundary layer behind the structured plates is fully turbulent as the velocity profiles at the rear of the test plates strictly adhere to the logarithmic law. However, the flow above the individual structures is more complex because of the wavy surface and the presence of pressure gradients.

		19.5m/s		**24.5m/s**		**27.5m/s**	
		Front	Rear	Front	Rear	Front	rear
S	C_f (OFI)	3.45x10^{-3}	2.8x10^{-3}	3.13x10^{-3}	2.46x10^{-3}	3.08x10^{-3}	2.24x10^{-3}
	u_τ (m/s), CL	0.81	0.78	0.99	0.935	1.09	1.04
	C_f (CL)	3.35x10^{-3}	3.14x10^{-3}	3.23x10^{-3}	2.91x10^{-3}	3.12x10^{-3}	2.84x10^{-3}
	δ_1 (mm)	1.103	2.415	1.101	2.376	1.104	2.29
	δ_2 (mm)	1.587	3.321	1.55	3.299	1.512	3.131
O0	C_f (OFI)	3.36x10^{-3}	2.39x10^{-3}	3.2x10^{-3}	2.29x10^{-3}	2.97x10^{-3}	2.32x10^{-3}
	u_τ (m/s), CL	0.8	0.735	0.98	0.925	1.06	1.05
	C_f (CL)	3.38x10^{-3}	2.84x10^{-3}	3.22x10^{-3}	2.82x10^{-3}	2.99x10^{-3}	2.91x10^{-3}
	δ_1 (mm)	1.031	2.977	1.026	2.752	1.079	2.53
	δ_2 (mm)	1.469	4.129	1.447	3.769	1.559	3.36
O90	C_f (OFI)	3.3x10^{-3}	2.43x10^{-3}	3x10^{-3}	2.3x10^{-3}	3.11x10^{-3}	2.24x10^{-3}
	u_τ (m/s), CL	0.79	0.72	0.95	0.94	1.09	1.04
	C_f (CL)	3.35x10^{-3}	2.84x10^{-3}	3.16x10^{-3}	2.87x10^{-3}	3.12x10^{-3}	2.8x10^{-3}
	δ_1 (mm)	1.09	3.345	1.164	2.935	1.057	3.262
	δ_2 (mm)	1.545	4.655	1.643	3.949	1.505	4.477
I0	C_f (OFI)	3.45x10^{-3}	2.22x10^{-3}	3.13x10^{-3}	2.18x10^{-3}	3.08x10^{-3}	1.95x10^{-3}
	u_τ (m/s), CL	0.83	0.70	0.97	0.85	1.08	0.93
	C_f (CL)	3.4x10^{-3}	2.63x10^{-3}	3.23x10^{-3}	2.43x10^{-3}	3.11x10^{-3}	2.34x10^{-3}
	δ_1 (mm)	1.1	3.627	1.075	3.641	1.09	3.632
	δ_2 (mm)	1.59	5.146	1.513	5.121	1.552	5.098
I90	C_f (OFI)	3.45x10^{-3}	2.22x10^{-3}	3.13x10^{-3}	2.24x10^{-3}	3.16x10^{-3}	2.1x10^{-3}
	u_τ (m/s), CL	0.81	0.69	1	0.87	1.11	0.97
	C_f (CL)	3.37x10^{-3}	2.53x10^{-3}	3.21x10^{-3}	2.52x10^{-3}	3.2x10^{-3}	2.48x10^{-3}
	δ_1 (mm)	1.09	3.896	0.994	3.74	0.989	3.682
	δ_2 (mm)	1.54	5.575	1.358	5.30	1.368	5.14

Tabel 4: Boundary layer quantities at front and rear of the test plates with the help of Oil film Interferometry (OFI) and Clauser chart method (CL)

The local shear stress coefficients obtained by both the techniques namely Clauser-chart and Oil film interferometry at the rear of the structured plates are significantly lower than the values of C_f for a smooth plate. The highest reduction in the value of C_f was recorded for the configuration I0 for all the flow velocities and the second highest for I90 with a minuet difference between them. The shape of the velocity profiles at the rear of structured plates suggests that flow is attached to the plate and is stable, fitting well into the logarithmic law. Hence, it can be confirmed that this reduction in shear stress is not due to any local separation of the flow. It can be hypothesized that the hexagonal structures influence the main flow in such a way that the sub-layer beneath the turbulence created by the structured plates contains less multidimensional vortex structures reducing the turbulent kinetic energy of the flow near the wall and hence the shear stress between the flow and the surface.

Fig. 45 displays the relationship between C_f and the investigated configurations obtained by both the measurement techniques. I0 and I90 possess the lowest shear stress coefficients. On the other hand, the momentum thickness measured behind the test plate is largest for I90. Momentum thickness is plotted against the investigated configurations in Fig. 46. As the difference in momentum thickness between front and rear of a test plate is a measure of the global drag of the test plate, I90 seems to have the highest drag coefficient among all the configurations.

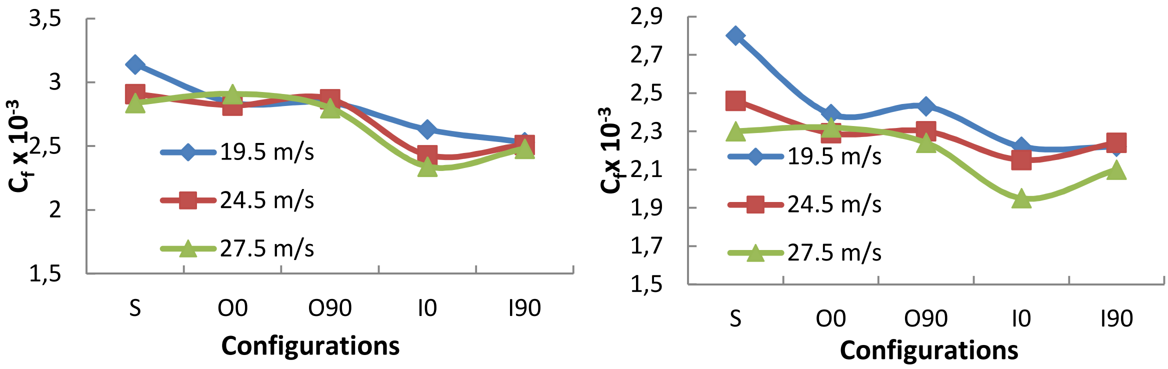

Fig 45: Shear stress coefficient at the rear of the plates vs configurations obtained by Clauser chart method (left) and Oil film interferometry (right)

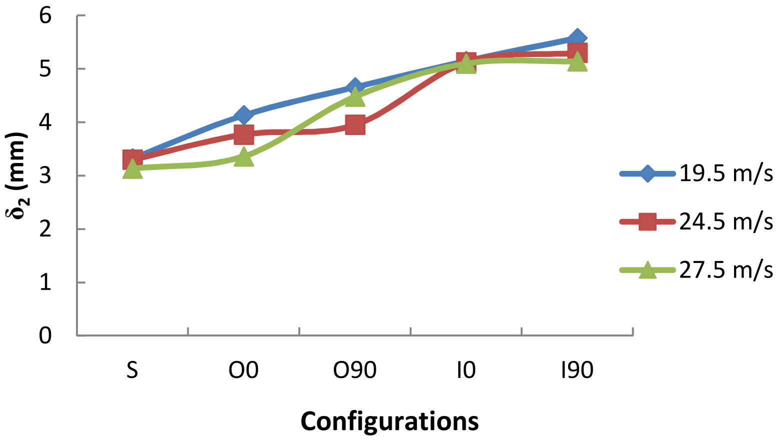

Fig 46: Momentum thickness at the rear of the test plates vs configurations behind the structured plates

A reduction in local shear stress coefficient at the rear of the test plates seems quite positive but it is achieved at the expanse of momentum thickness. The thicker boundary layer and an increased momentum thickness result in an enhanced value of total drag C_F. C_F is determined for each configuration by using eq. 2.3.4. The largest increase in C_F is recorded for the configuration I90 and amounts to about 120%. Table 5 summarizes the values of global drag coefficients for all the investigated configurations and velocities. Although, a significant decrease in the values of wall shear stress coefficients have been recorded at the rear of the plates and an even higher drop is expected within the hexagonal dimples, larger values of C_F for nearly all the test plates may be caused by an irregular pressure distribution over individual hexagonal structures. In this way, contribution of pressure drag in the total drag of a structured plate cannot be overruled. Nevertheless, it can be concluded that the decrease in local skin friction is achievable behind hexagon like surface depressions but at the expanse of total drag.

	19.5m/s	**24.5m/s**	**27.5m/s**
	C_F	**C_F**	**C_F**
S	$3.1x10^{-3}$	$2.92x10^{-3}$	$2.7x10^{-3}$
O0	$4.43x10^{-3}$	$3.87x10^{-3}$	$3.3x10^{-3}$
O90	$5.18x10^{-3}$	$3.84x10^{-3}$	$4.95x10^{-3}$
I0	$5.9x10^{-3}$	$6x10^{-3}$	$5.9x10^{-3}$
I90	$6.7x10^{-3}$	$6.57x10^{-3}$	$6.27x10^{-3}$

Table 5: Global skin friction coefficient C_F for all the investigated configurations

6.2.3 Flow over individual hexagonal structure

6.2.3.1 Optimization of the measurement techniques

To comprehend the phenomenon of elevated global drag of a structured plate, measurements of shear stresses and pressure on individual hexagonal structures were performed. In the next sections, results of these investigations are documented and explicated with the help of figures and curves.

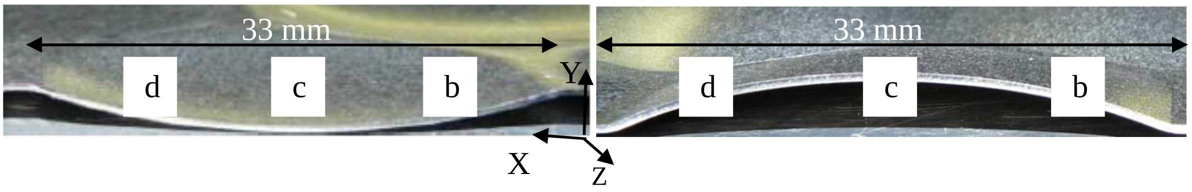

Fig 47: Measurement locations, flow from right to left

Oil film interferometry was applied to measure the shear stresses acting on the hexagonal structures at three different locations and velocities (Fig. 47). Due to the curvature, very strong pressure gradients either positive or negative are likely to exist at various locations (Fig. 47) on the structure. Clauser-chart completely fails to predict the even near to accurate values of shear stress coefficient under such circumstances. As already described, Clauser-chart primarily assumes the validity of universal logarithmic law to determine the shear stress coefficient. Whereas, the universal logarithmic law does not hold for the flows with pressure gradients. Fig. 48 shows the velocity profiles measured at specified locations above the surface of inwardly curved structures (I0 & I90) for a mean stream velocity of 19 m/s. Owing to the negative pressure gradient at locations b and c above the surface of I0, the curve deviates from the universal log law significantly with a very small set of data that fits into the log law. The estimated values of u_τ by using Clauser-chart method at these locations are 0.32 m/s and 0.29 m/s and contradict completely the values obtained by oil film interferometry (Table 6).

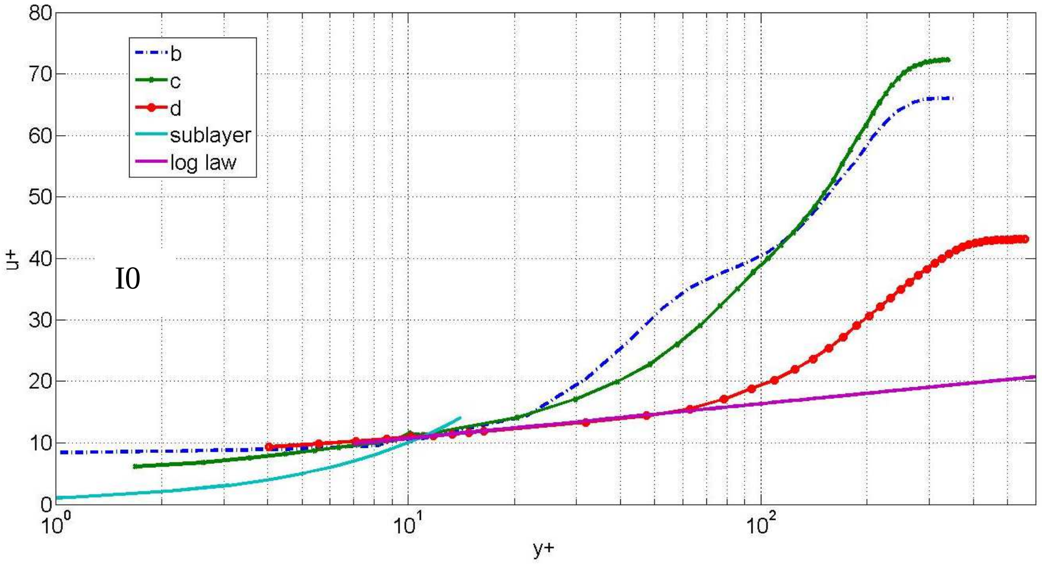

Fig 48-a: measured velocity profiles fitted into the logarithmic law for the determination of u_τ over I0

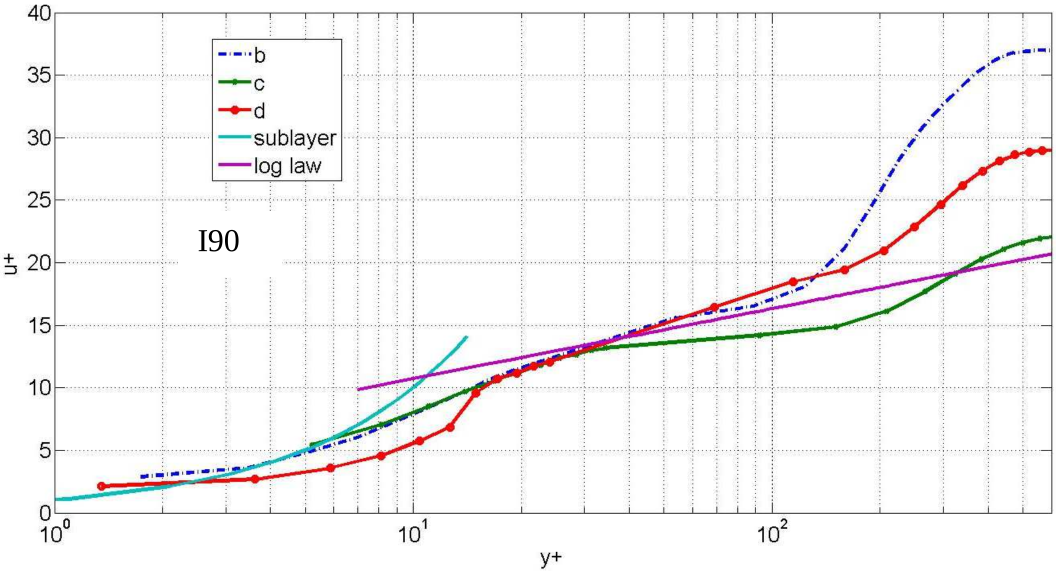

Fig 48-b: measured velocity profiles fitted into the logarithmic law for the determination of u_τ over I90

The flow experiences a negative pressure gradient at position d and still fits partly into the log law. This behavior is probably due to the sudden change in the slope of the surface i.e. the positive slope of the surface at location d counteracts a little bit the effects of a positive pressure gradient at locations b and c on the flow. u_τ at position d is found to be 0.48 m/s. One thing is clear from these results that the velocity profile of the flow in pressure gradients does not fit well into the logarithmic law and hence the wall shear stress obtained by this method must be doubted. On the other hand, oil film interferometry can easily be applied under such circumstances and accurate values of skin drag coefficients be achieved.

6.2.3.2 Shear Stress Measurements

Table 6 shows the shear stress velocities measured at three different locations (Fig. 47) and flow velocities for all the investigated configurations by using Oil film Interferometry. Shear stress velocities are presented in the Table instead of shear stress coefficients so that the results of both the techniques namely Clauser-chart method and oil film interferometry can be compared. Shear stress velocities can easily be converted into shear stress coefficients by knowing the free stream velocity. The shear stress velocities are obtained by capturing the fringe images and evaluating them using a self-developed Matlab code. An expected behavior can be observed by looking at the values, which is that a significantly lower value of shear stress is found at the middle (location c) of inwardly curved structure and a higher value at the downstream edge (location d). Whereas, the flow exerts a higher shear force on the rising edge (location b) of the outwardly curved hexagon structure and lower stress at the downstream edge (location d) as it leaves the hexagon.

	u_τ (S)			**u_τ (O0)**			**u_τ (O90)**			**u_τ (I0)**			**u_τ (I90)**		
	19.5 m/s	24.5 m/s	27.5 m/s	19.5 m/s	24.5 m/s	27.5 m/s	19.5 m/s	24.5 m/s	27.5 m/s	19.5 m/s	24.5 m/s	27.5 m/s	19.5 m/s	24.5 m/s	27.5 m/s
b	0.79	0.91	1.05	1.2	1.39	1.64	1.01	1.13	1.21	0.62	0.86	0.95	0.65	0.79	0.95
c	0.79	0.91	1.05	0.78	0.91	1.11	0.71	0.9	1.04	~0	~0	~0	0.6	0.7	0.84
d	0.79	0.91	1.05	~0	~0	~0	~0	~0	~0	0.88	0.94	1.13	0.91	1.1	1.14

Table 6: Shear stress velocities on individual hexagonal structures using oil film interferometry

The shear stress is nearly absent in the middle of the inwardly curved structure of I0. Quantitatively, its value is either 0 or extremely small that no fringes with enough quality to be evaluated were observed even after the passage of a very long time. Similar behavior is observed at locations d of O90 and O0. The shear stress velocity recorded on the surface at location d of I0 and I90 is in order of 1.14 m/s for a flow velocity of 27.5 m/s, which is higher than the shear stress velocity on a flat surface under identical conditions. At location b of O0 and O90, the shear stresses measured at various velocities are highest among all and approaches the values of 1.64 m/s and 1.21 m/s for the mean stream velocity of 27.5 m/s. They decay in streamwise direction and falls to nearly zero at location d.

6.2.3.3 Boundary layer measurements

Velocity profiles were recorded above the surface of individual hexagonal structures at specified positions with the help of hot wire anemometry. These profiles were processed and evaluated to deduct the boundary layer thicknesses, displacement thicknesses and momentum thicknesses. Fig. 49 displays the variation of above mentioned quantities vs downstream distance from the leading edge of the hexagon and free stream velocities. All the measurements including flat plate measurements were conducted at identical displacements from the nose of the base plate to ensure the constant Reynolds numbers for flat and structured plates. The displacement and momentum thicknesses for a flat surface are in order of 1.2 mm and 1.7 mm. The variation due to change in free stream velocity is minuet. The profile shapes above the hexagonal structures seem to follow the contour of the hexagonal structure. The displacement thickness of an outwardly curved structure (O0 & O90) is in order of 1.6 mm at the leading edge of the structure, which is significantly higher than the flat surface. It decays to a value of 0.86 mm and rises again to about 1.74 mm, which is slightly higher than the value at the leading edge. A similar behavior is shown by the momentum thickness profile. As the height of the structure increases, the values decreases and attain their minimum at the highest point of the structure, which is at its middle. The quantities start rising with the decreasing height of the structure downstream and end up at a higher than the starting value of momentum thickness. For inwardly curved structures (I0 & I90), the profile shapes are the mirror images of the profile shapes of outwardly curved structures. The values at trailing edge of the structures are higher than at leading edges, indicating a net increase in displacement and momentum thicknesses across the hexagonal structures in streamwise direction.

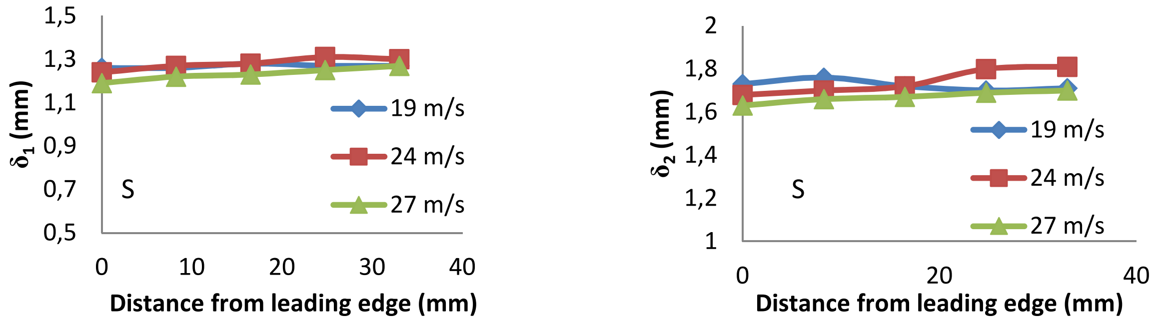

Fig 49-a: Displacement thickness vs upstream distance (left), Momentum thickness vs upstream distance (right) over S

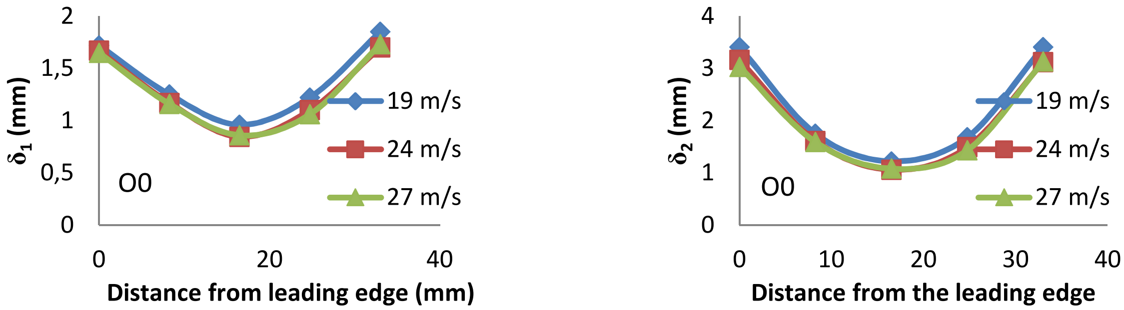

Fig 49-b: Displacement thickness vs upstream distance (left), Momentum thickness vs upstream distance (right) over O0

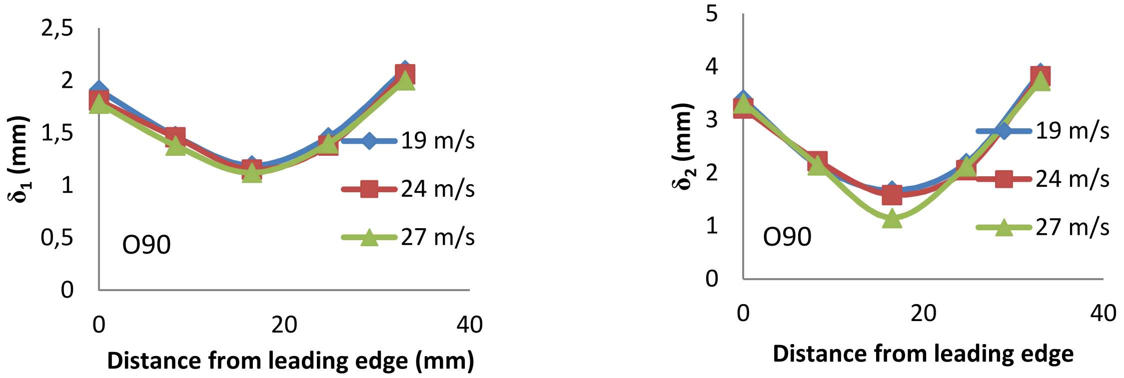

Fig 49-c: Displacement thickness vs upstream distance (left), Momentum thickness vs upstream distance (right) over O90

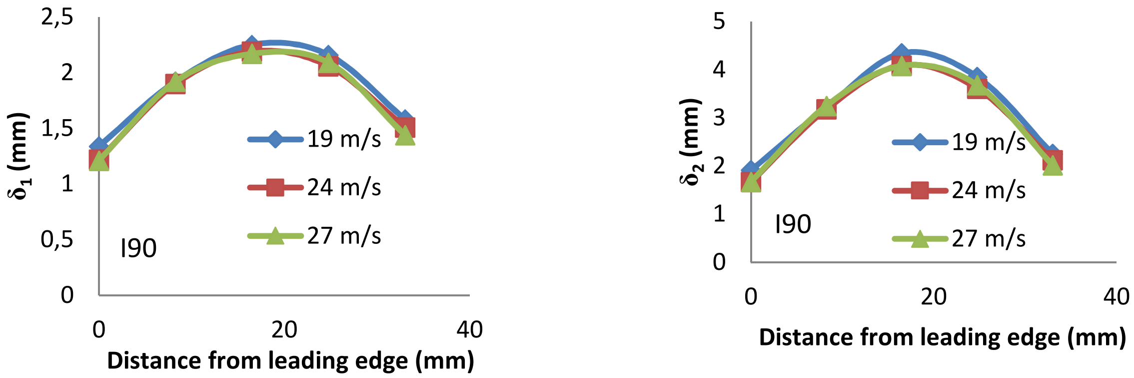

Fig 49-d: Displacement thickness vs upstream distance (left), Momentum thickness vs upstream distance (right) over I90

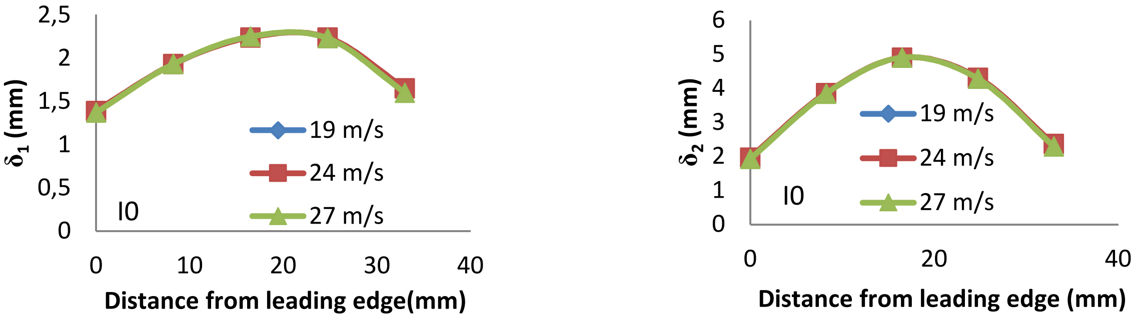

Fig 49-e: Displacement thickness vs upstream distance (left), Momentum thickness vs upstream distance (right) over I0

This net increase is larger than the increase in displacement and momentum thicknesses above the flat surface, resulting in a thicker boundary layer and hence an increased total drag. The largest increase in displacement and momentum thickness is exhibited by I0.

6.2.3.4 Flow structures within the hexagonal depressions and bumps

Hot wire measurements were performed at locations b, c and d and r.m.s velocities recorded. R.m.s velocity profiles against vertical distance Y above a smooth surface at specified locations is presented in Fig. 50. A small peak near the surface indicating the buffer layer i.e. where the laminar sub-layer of a turbulent boundary layer transforms into a turbulent layer, is visible for all the velocities and locations. As y increases, the r.m.s velocity profile decays and fall to a value of u´ for free stream flow.

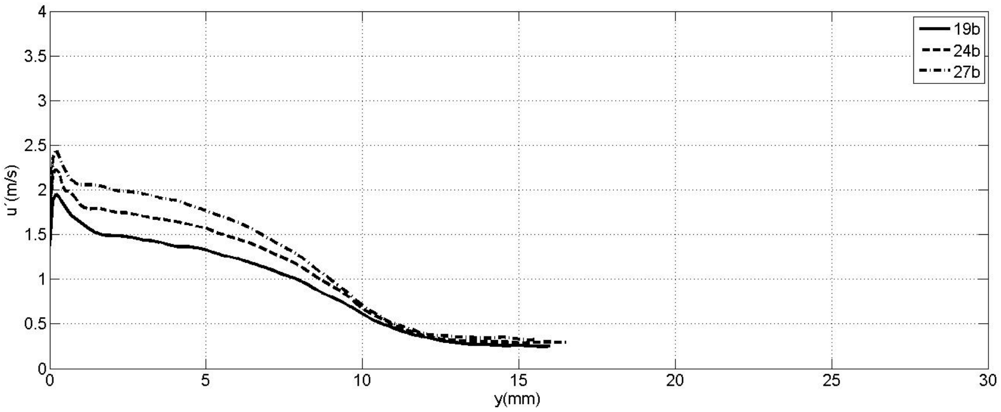

Fig 50-a: Velocity fluctuations over smooth surface at location ‘b’ for velocities 19, 24 and 27m/s

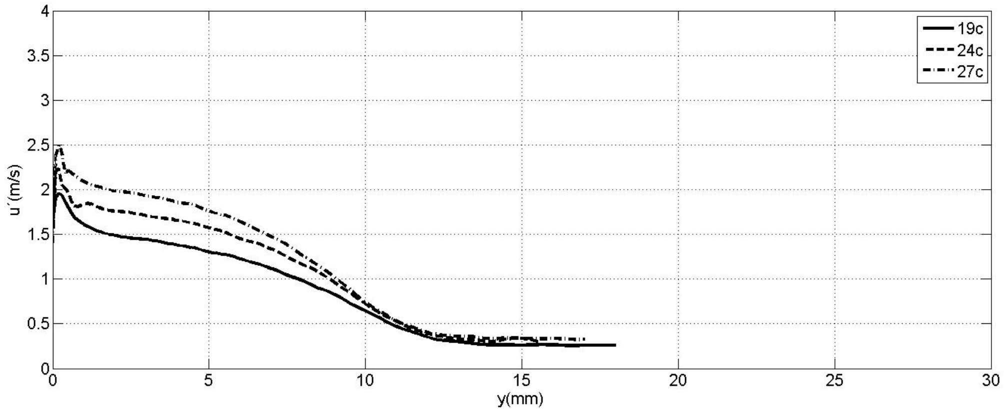

Fig 50-b: Velocity fluctuations over smooth surface at location 'c' for velocities 19, 24 and 27m/s

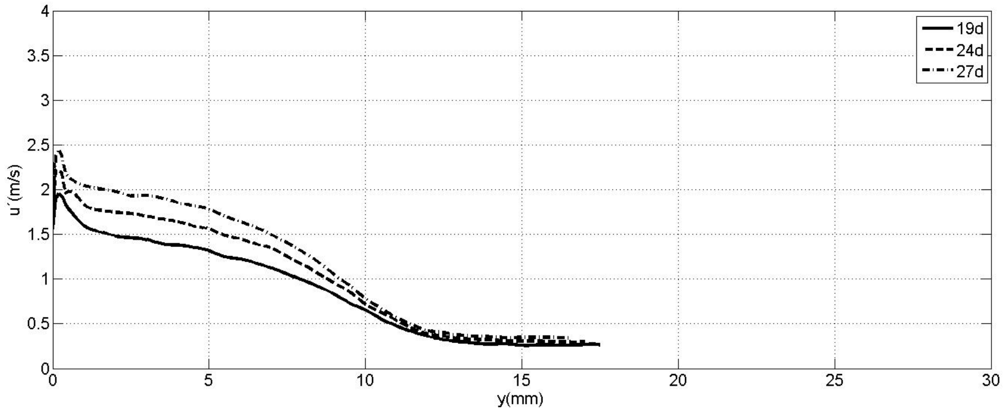

Fig 50-c: Velocity fluctuations over smooth surface at location 'd' for velocities 19, 24 and 27m/s

It is quite interesting to observe that a second peak next to the peak caused by the transition of the flow is present in the velocity curves of the configuration O0 (Fig. 51). The magnitude of this peak is highest for location b and fades away with the changing measurement location downstream. Vortex structures emanating due to detachment of the flow from the surface of the upstream hexagon should be responsible for the observed peak. This happens because the flow cannot follow the curved contour of the hexagonal structures strictly due to adverse pressure gradients and separates somewhere near the downstream edge of the hexagon. This effect has been elucidated with the help of flow visualization by using oil film interferometry in Section 6.2.3.6.

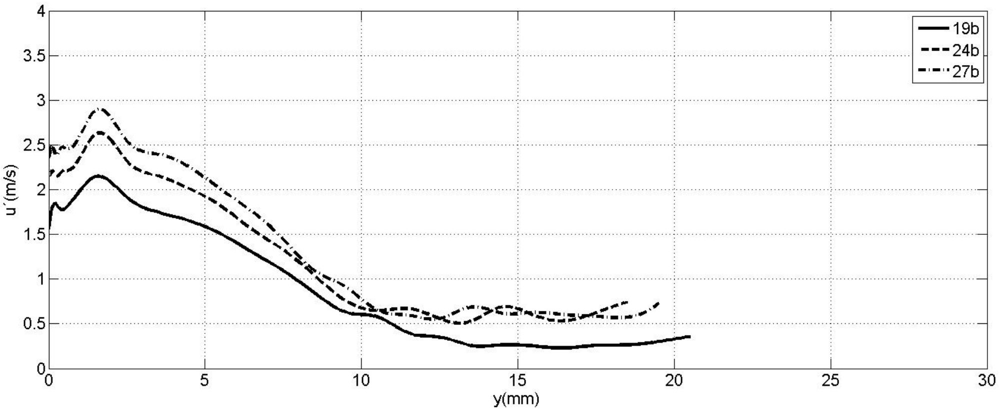

Fig 51-a: Velocity fluctuations over O0 surface at location ‘b’ for velocities 19, 24 and 27m/s

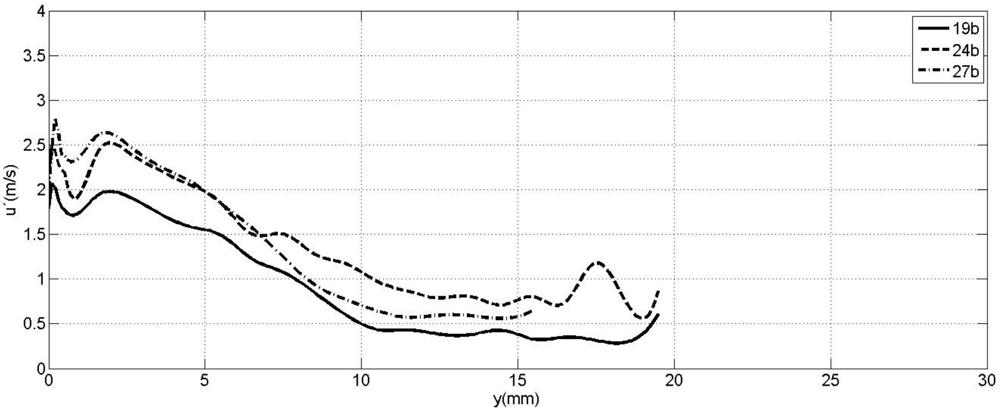

Fig 51-b: Velocity fluctuations over O0 surface at location ‘c’ for velocities 19, 24 and 27m/s

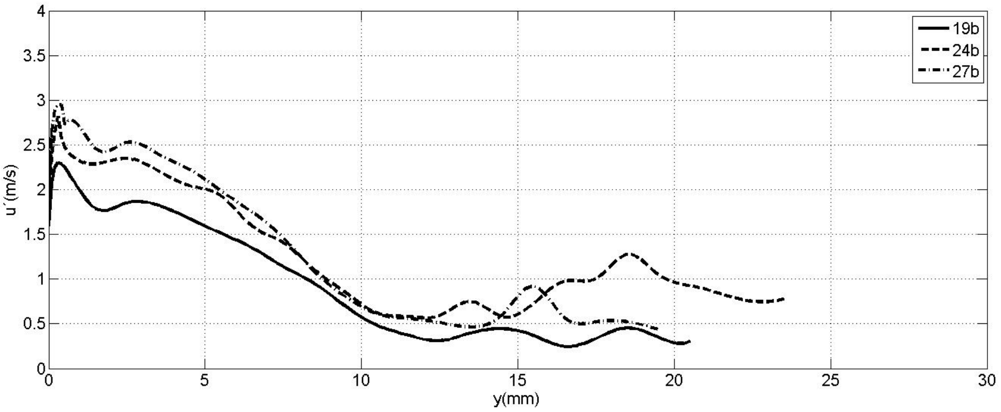

Fig 51-c: Velocity fluctuations over O0 at location ‘d’ and velocities 19, 24, 27m/s

Fig. 52, exhibiting the velocity profiles above the configuration O90, illustrates a similar behavior as O0 with the only exception that the peak remains visible for all the locations. The vertical distance of the peak from the surface is largest at location d. Two counter rotating vortex structures circulating in a vertical plane (Y-Z) normal to the flow originate at the rising edge of the hexagon producing the secondary peaks in r.m.s velocity profiles (see Section 6.2.3.6). These flow structures follow the direction of the mean flow. Therefore, vertical distance between the peak and the surface is higher for the latter measurement location as the height of the hexagonal structure is lowest there.

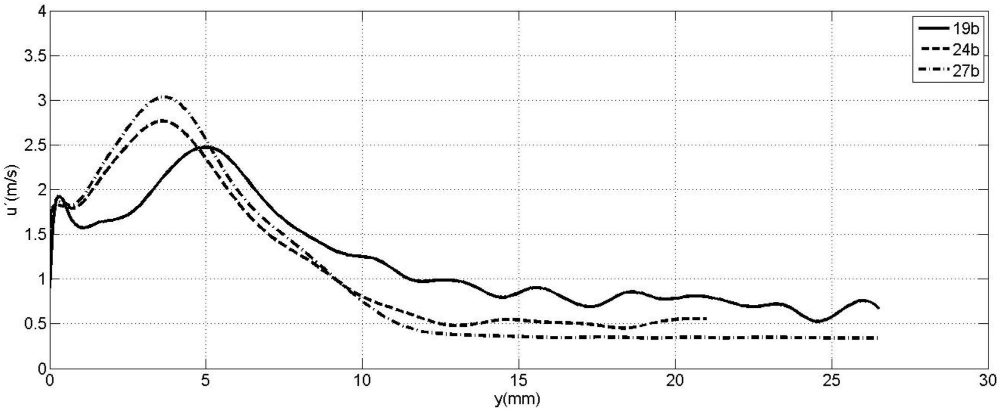

Fig 52-a: Velocity fluctuations over O90 at location ‘b’ and velocities 19, 24, 27m/s

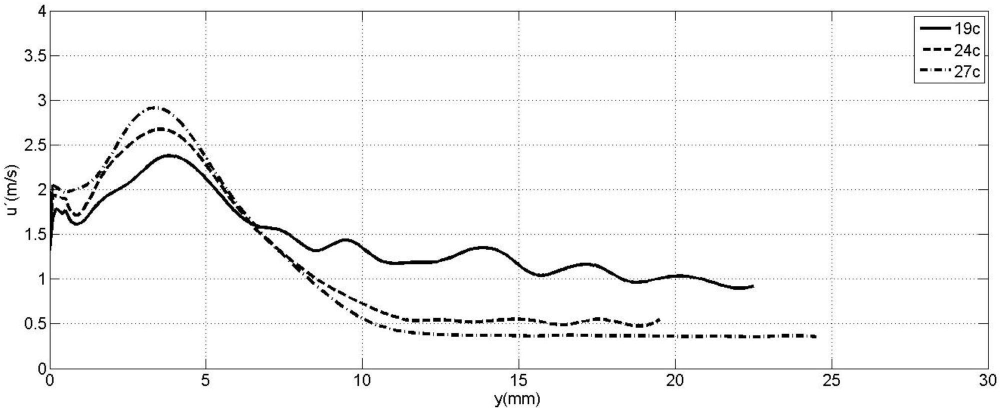

Fig 52-b: Velocity fluctuations over O90 at location ‘c’ and velocities 19, 24, 27m/s

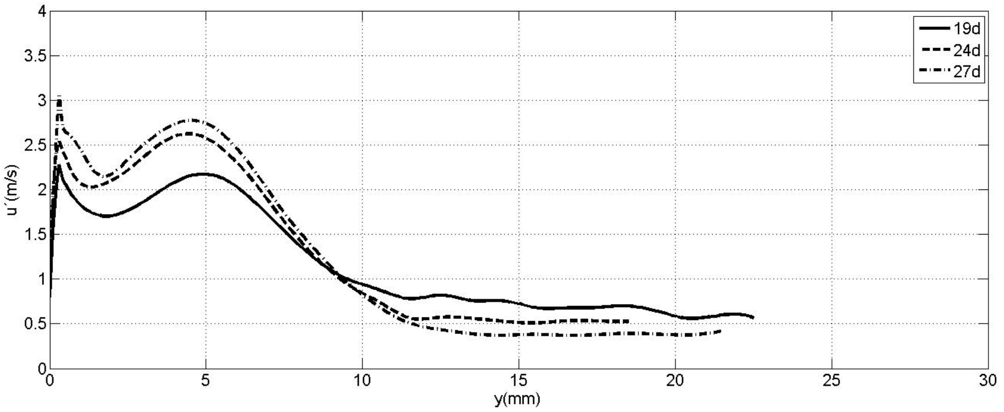

Fig 52-c: Velocity fluctuations over O90 at location ‘d’ and velocities 19, 24, 27m/s

The most interesting phenomenon is illustrated by the velocity profile of the configuration I0 with two consecutive secondary peaks, one after the other (Fig. 53). These peaks merge gradually to form a single larger peak till the location d is arrived. Two peaks definitely represent two vortex structures in the flow at the distances from the surface. What actually happens is, that the flow bifurcates as it enters the depression and form two circulating flow structures in a vertical plane (X-Z) swirling in counter directions. The propagation of these counter rotating flow structures follow the direction of the main flow and merge together to form a single and more complex vortical structure with vortices rotating in multi directions creating a complex circulating region. A surface visualization of such a flow structures is presented in Section 6.2.3.6.

The velocity profiles of I90 (Fig. 54) show a single but a wider peak. In this case, the flow again divides itself into two counter rotating vortices with their axis of rotation parallel to the flow as the flow enters the depression. The vortices rotate opposite to each other in a vertical Y-Z plane at the same height from the surface and propagate in the flow direction (See Section 6.2.3.6 for detail).

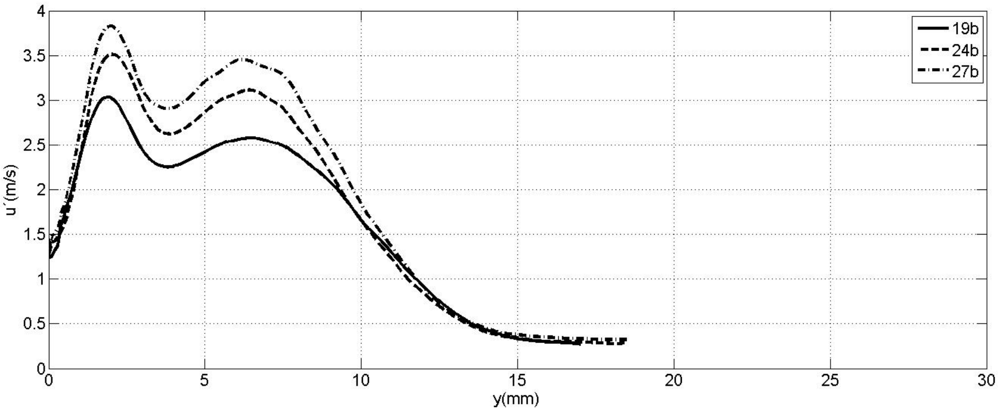

Fig 53-a: Velocity fluctuations over I0 at location 'b' and velocities 19, 24, 27m/s

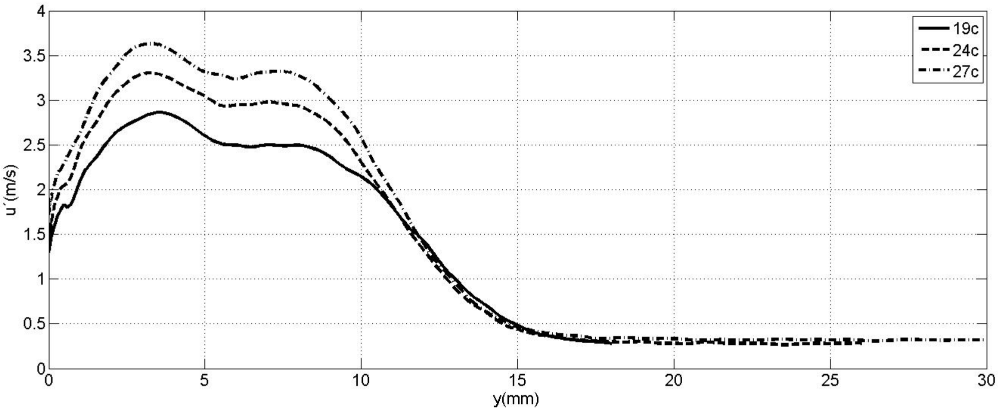

Fig 53-b: Velocity fluctuations over I0 at location 'c' and velocities 19, 24, 27m/s

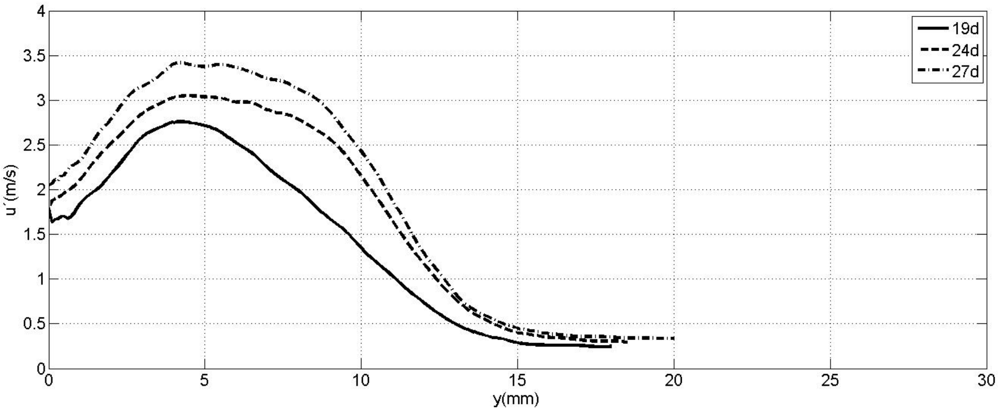

Fig 53-c: Velocity fluctuations over I0 at location 'd' and velocities 19, 24, 27m/s

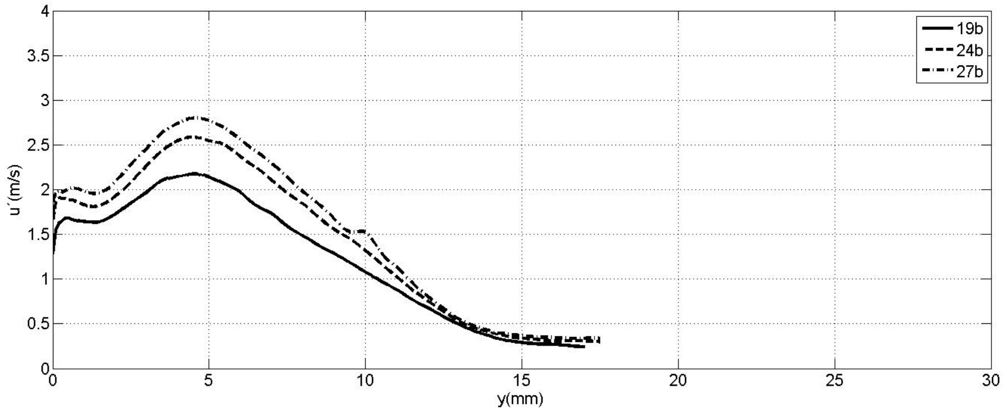

Fig 54-a: Velocity fluctuations over I0 at location ‘b’ and velocities 19, 24, 27m/s

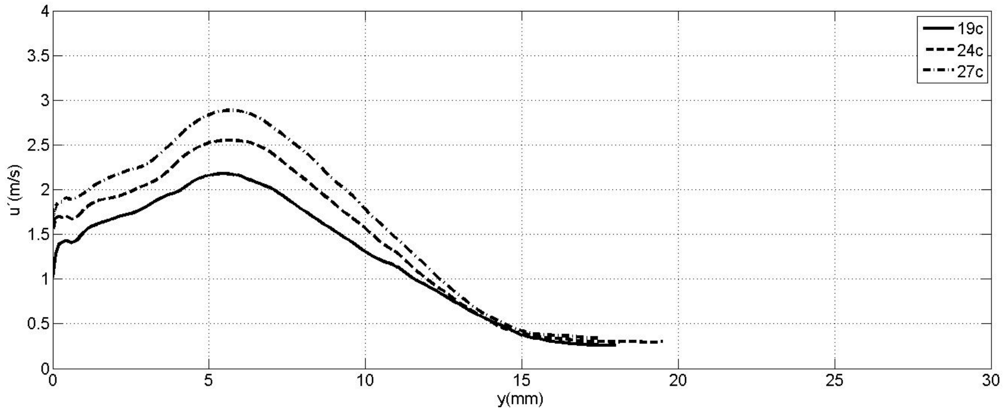

Fig 54-b: Velocity fluctuations over I0 at location ‘c’ and velocities 19, 24, 27m/s

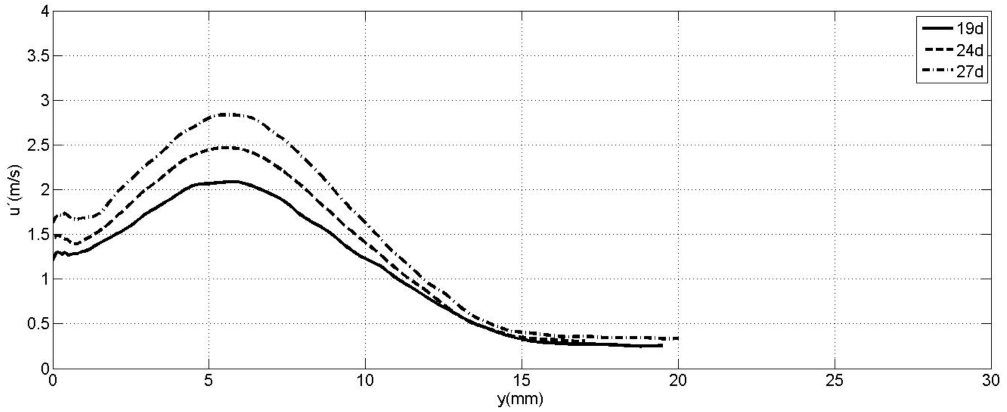

Fig 54-c: Velocity fluctuations over I0 at location ‘d’ and velocities 19, 24, 27m/s

6.2.3.5 Power spectrum

It is necessary to examine whether the vortex structures present in the flow are shed periodically. To achieve the purpose, power spectrum of the flow with a mean stream velocity of 24 m/s at specified locations was determined. A hot wire probe placed at a vertical distance from the surface where u´ is maximum. This procedure was repeated for locations b, c and d. Voltage time series recorded by the hot wire probe was processed using a self-made Code in Matlab to determine the power spectrum of the flow.

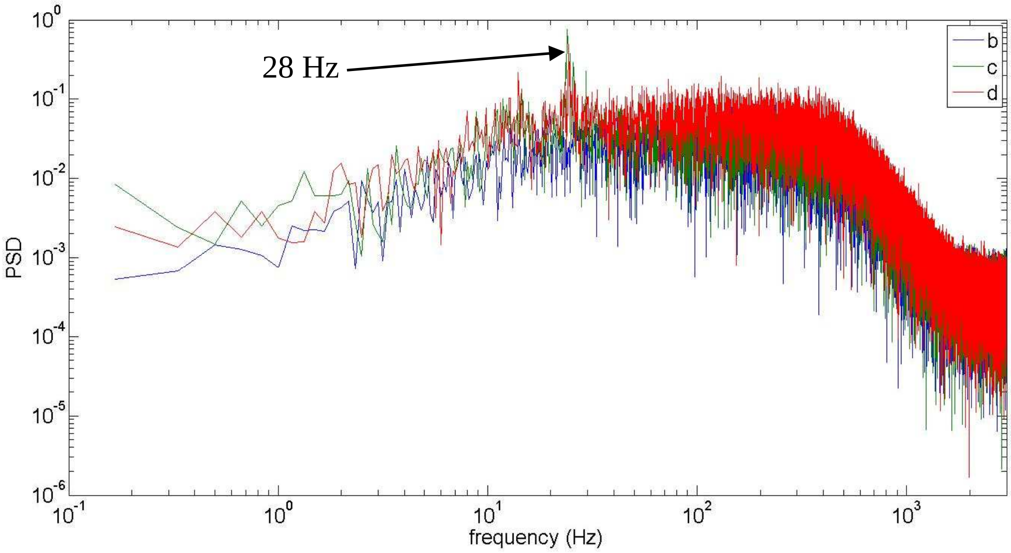

Fig 55: Power Spectral Density (PSD) of the flow over O0 vs frequencies at 24 m/s

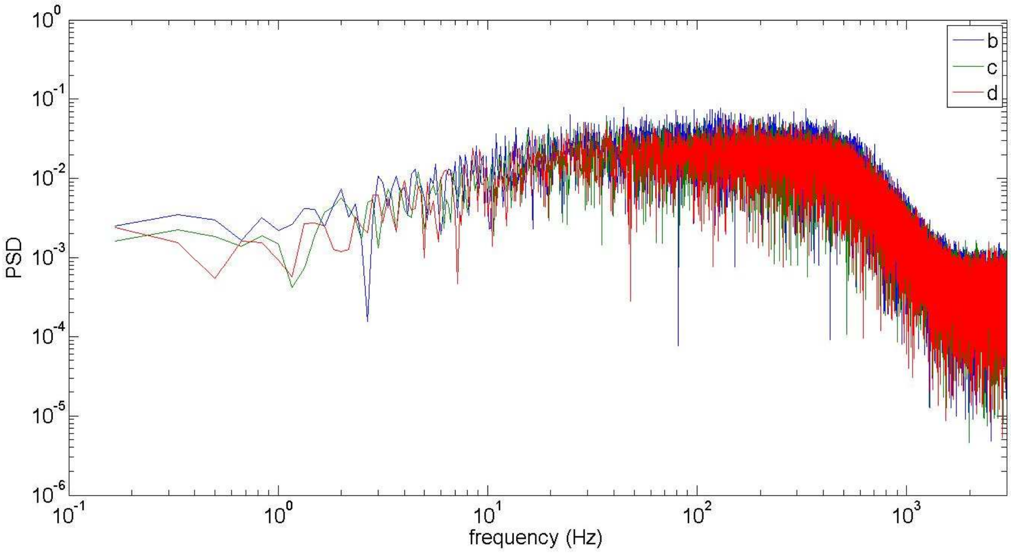

Fig 56: Power Spectral Density (PSD) of the flow over O90 vs frequencies at 24 m/s

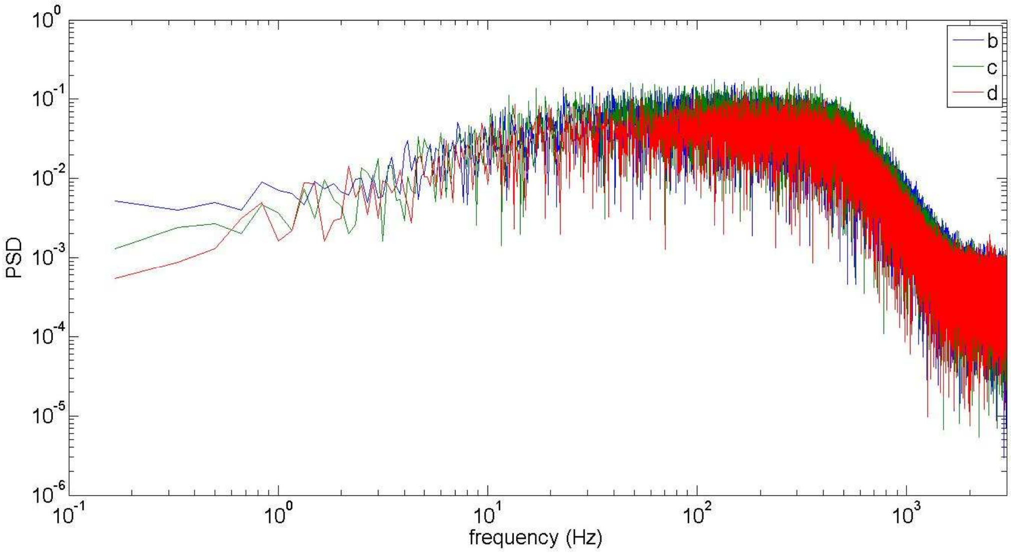

Fig 57: Power Spectral Density (PSD) of the flow over I90 vs frequencies at 24 m/s

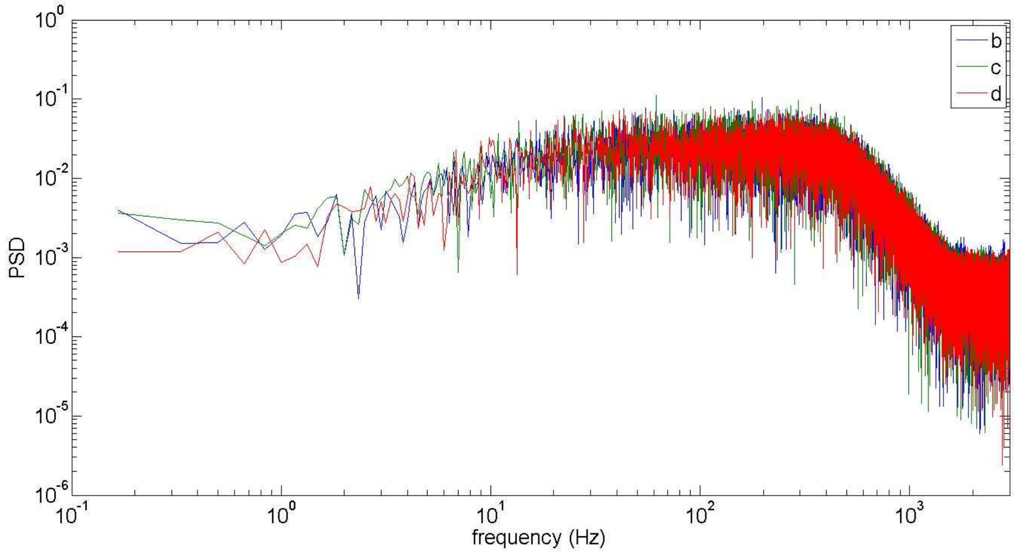

Fig 58: Power Spectral Density (PSD) of the flow over I0 vs frequencies at 24 m/s

Fig. 55 shows the power spectrum of the flow over the hexagonal structure of O0. Power spectral density is plotted against frequencies. A peak indicating the vortex shedding frequency (28 Hz) present in the flow is clearly visible at all the locations accept the location b, which validates the assumption that the flow detaches from the surface somewhere near the downstream edge of the hexagon. No peak and hence no periodic vortex shedding is to be observed in the power spectrum of other configurations (Fig. 56 - 58). This surely indicates that the regions of maximum u´ (peaks in u´-y curves) above the hexagons of latter configurations are caused by irregular shedding of flow structures from the upstream hexagons.

6.2.3.6 Visualization of flow over the surface

Oil film interferometry technique not only predicts the accurate values of shear stresses but also helps to visualize the flow near the surface indicating the direction and magnitude of the shear stress acting on the surface. Fig. 59-62 illustrate the fringe images produced by the flow over individual hexagonal structures of each configuration. Flow direction is from right to left

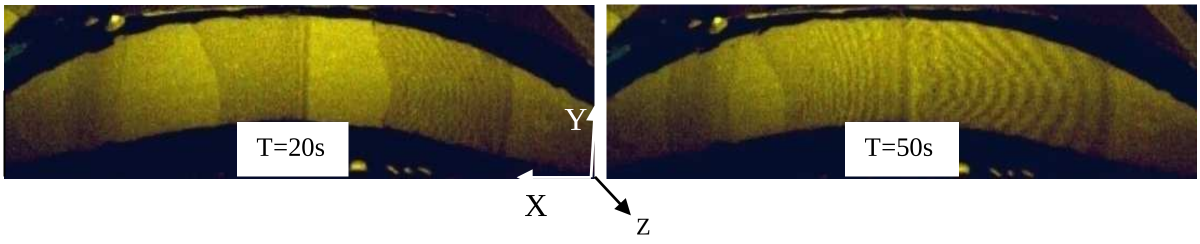

Fig 59: Fringe images over O90

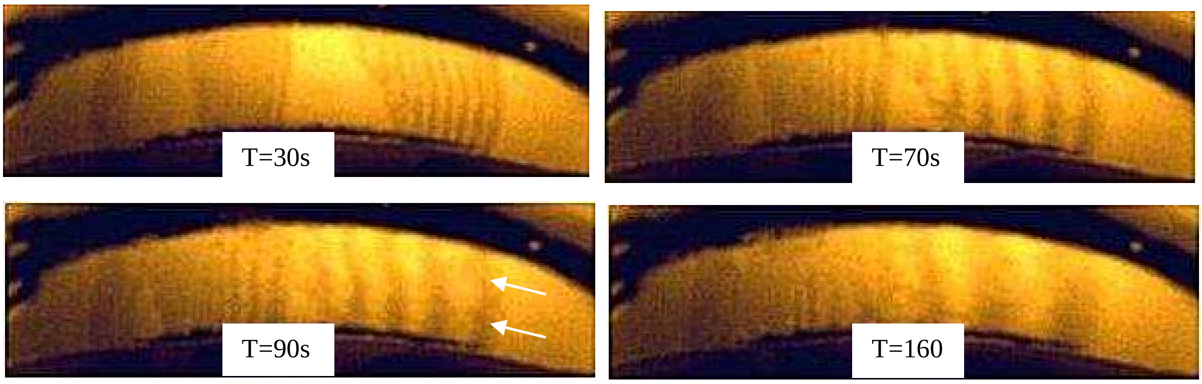

Fig 60: Fringe images over O0

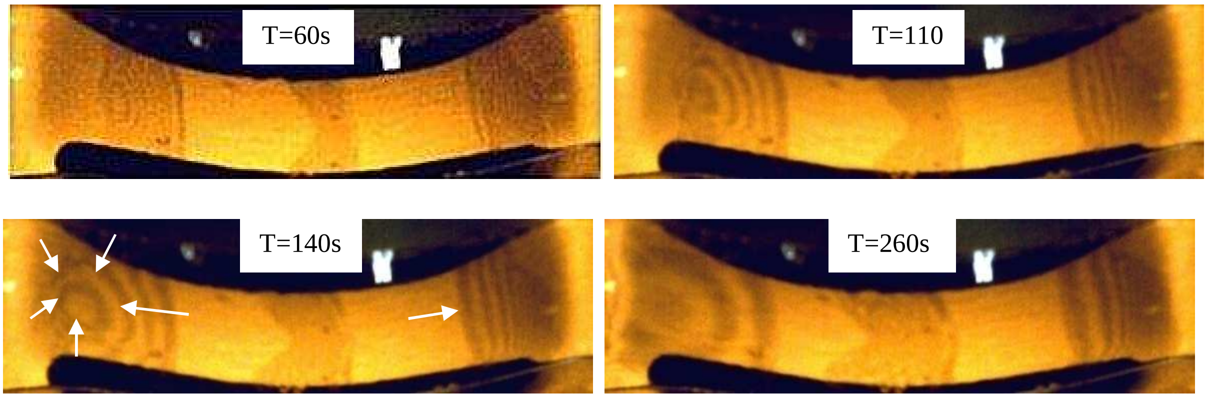

Fig 61: Fringe images over I0

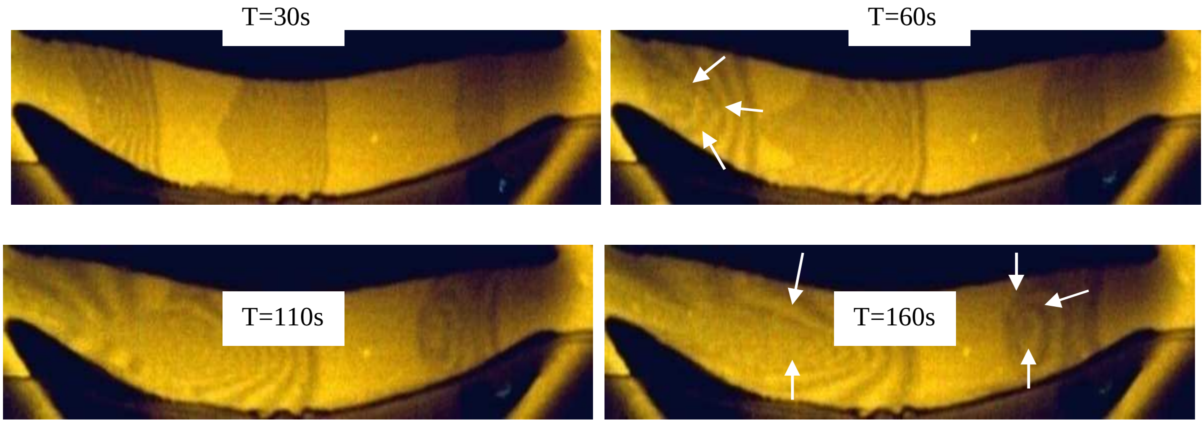

Fig 62: Fringe images over I90

By looking at the time history of the development of the fringes, several stunning conclusions besides the plausible vindication of the presented results in Table 6 can be drawn. At time T = 20 seconds, fringes start appearing at location b (Fig. 59), whereas no fringes are visible at location c and d. At T= 50 sec the fringes start emerging at location c. The comparison of fringe spacing at location b and location c after the same time suggests that the shear stress is higher at location b as indicated in Table 6. No fringes with sufficient quality to be evaluated can be observed even after passage of a very long time at location d. This indicates that either the shear stress is absent at this location or extremely low to be predicted by the present measurement technique. The arrows indicate the direction of the shear force acting on the surface. It is necessary to mention that the length of the arrows do not quantify the magnitude of shear stress. Their purpose is just to show the direction of the shear force. The arrows pointing each other suggest the presence of a counter rotating vortex pair in Y-Z plane with their axis of rotation being parallel to the flow. Some similar flow structures were identified by ligrani et.al [27] within the dimple structures. We believe that the flow divides at the rising edge above the centerline into two circulating flow structures in Y-Z plane, due to the orientation (V corner facing the flow) of hexagonal structure to the flow, and start rotating in counter directions. It seems that the longitudinal movement of the pair of circulating flow structures does not strictly follow the contour of the surface, as no visible patterns can be observed at location d.

Fig. 60 illustrates the fringe patterns and their development history on the outwardly structure of O0. The development of the fringes with time and along the surface is in a way similar to O90 with the highest shear stress at location b and the lowest at location d. Only difference is that the fringes appear to be the straight parallel bands drifting with time in the flow direction. The shear force indicated by the arrows acts only in one direction i.e. the flow direction. No counter rotating Vortices or circulating regions must exist above the centerline.

Fringe patterns of I0 illustrate another interesting phenomenon at location b (Fig. 61). The fringes appear to grow with time in a direction opposite to the flow, indicating the presence of a circulating region with its axis in transverse direction pushing the oil fringes opposite to the flow. Together with the results presented in Fig. 53 and Fig. 61 it can be interpreted that as the flow enters sudden depression, it bifurcates into two counter rotating vortices in X-Z plane (creating two peaks in Fig. 53). In the middle of depression, no visible fringes could be observed even after the passage of a long time. The fringe spacing at location d is the largest indicating the presence of highest shear stress. It seems that multi-dimensional circulating flow structures exist at location d. The shear stresses from multi directions indicated by the arrows are acting in a plane parallel to the plate pointing each other. Various vortex structures in an arrangement similar to the slices in an orange forming a sphere of a circulating region must be present forming dark circular bands on the surface.

Fringes at all the locations of I90 (Fig. 62) predict the existence of circulation regions similar to O90 and I0. Shear stress is highest at location d among all the locations. The dark circular bands at location b indicate the presence of a sphere of vortex structures like the one at location d of I0 with shear stresses acting from all the directions. The V shaped fringes at location c evidence the presence of a pair of circulating vortex structures in Y-Z plan. This pair of vortices must be propagating in the flow direction creating similar fringe patterns at location d.

6.2.3.7 Pressure distribution

Furthermore, static pressure variation over the surface of each hexagonal structure is determined using pressure holes. The pressure distribution is measured at two different locations in Z direction, about half the length of a hexagon apart from each other (Fig. 63).

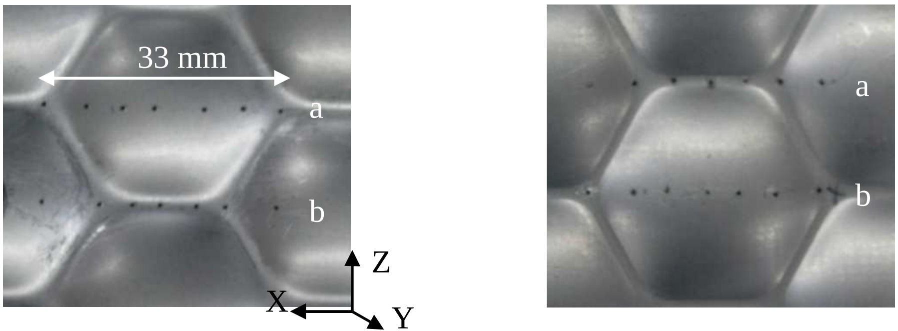

Fig 63: Pressure holes for pressure measurement, flow direction from right to left

As already described, the pressure gradient was kept zero over the flat plate in flow direction by adjusting the flap mounted on the trailing edge of the base plate.

Fig. 64-67 shows the distribution of pressure in streamwise direction over the hexagonal structures of investigated configurations for three different flow velocities. Very high pressure gradients are clearly visible at rising and falling edges of inwardly and outwardly curved hexagonal structures. In Fig. 64b the static pressure above O0 is highest at x = 0, a location between two consecutive hexagons, and decays in streamwise direction to a value of about -45 Pa. The flow velocity above the surface is highest at this location. The pressure increases with further increasing x and decreasing height of the hexagon and achieves a highest value of 55 Pa.

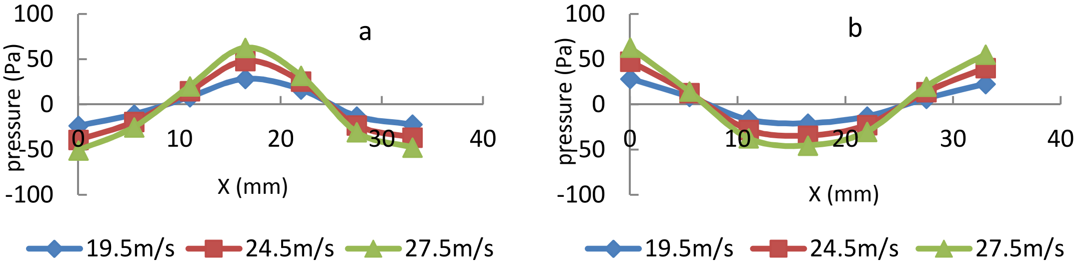

Fig 64: Pressure distribution over O0

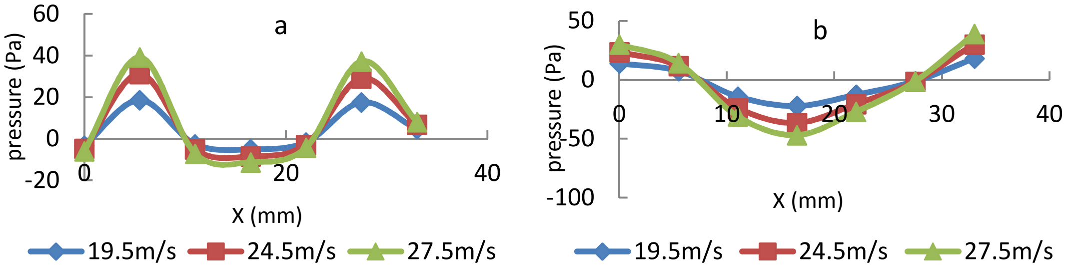

Fig 65: Pressure distribution over O90

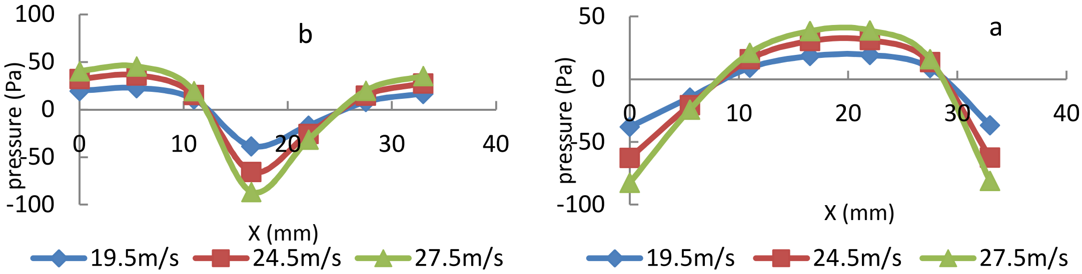

Fig 66: Pressure distribution over I0

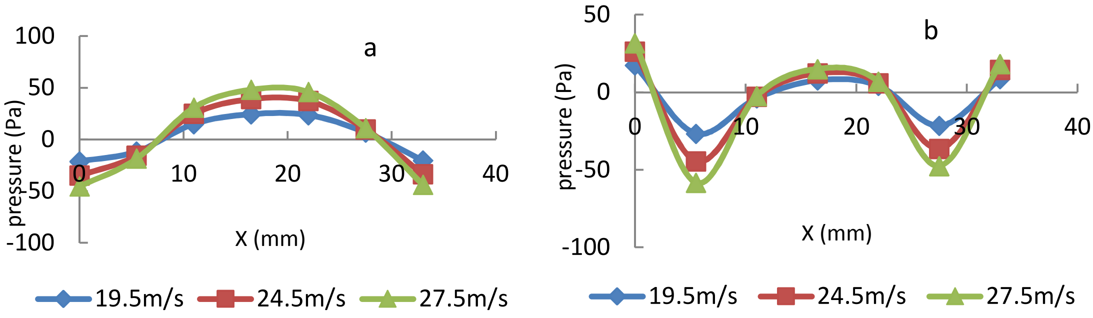

Fig 67: Pressure distribution over I90

A similar behavior is exhibited at other flow velocities but slightly different values of static pressure. This pressure distribution on the wavy (structured) surface yields a pressure force in streamwise direction, which contributes to the pressure drag. The collective pressure drag of the structures on the plate is in turn responsible for a dramatic increase in the global drag of the structured plate.

Pressure distribution over the structure of O90 (Fig. 65b) seems not much different from O0 (Fig. 64b). The highest values of static pressures are in order of 30 Pa for O90, whereas these are in order of 50 Pa for O0.

Fig. 65a illustrates the pressure distribution over the inwardly curved structure of I0. Pressure starts increasing gradually from a value of -82 Pa to 39 Pa and drops steeply at x = 22 mm to -81 Pa. It reveals the presence of a high pressure and low velocity region in the middle of the structure and vice versa on the edges. This uneven distribution of pressure creates a drag force elevating the global drag of the structured plate. Hence, bringing any kind of macro sized depressions i.e. spherical [19] or hexagonal in any orientation on a plate only aggravates the situation by increasing the total drag acting on the plate.

A similar behavior as I0 but with different peak values of static pressure is displayed in Fig. 66a. The pressure drop for individual inwardly and outwardly curved structures seems not extremely different. The collective obstructions (pressure drops) above the inwardly curved structured plate must be higher than the outwardly curved structured plate raising its global drag coefficient to about 120% of a smooth plate.

6.3 Experimental Wind Turbine

Efficiencies of various configurations of the turbine were measured for a set of angular speeds. Following curves display the measured efficiencies against angular speeds for 6 different flow velocities. Fig. 68-72 display the efficiencies of both the turbines, one with flat surface blades and one with structured surface blades at θ = 60° over a set of angular speeds. In general it can be observed, the turbine operates with maximum efficiency when its rotational speed is about 64% of the highest possible rpm.

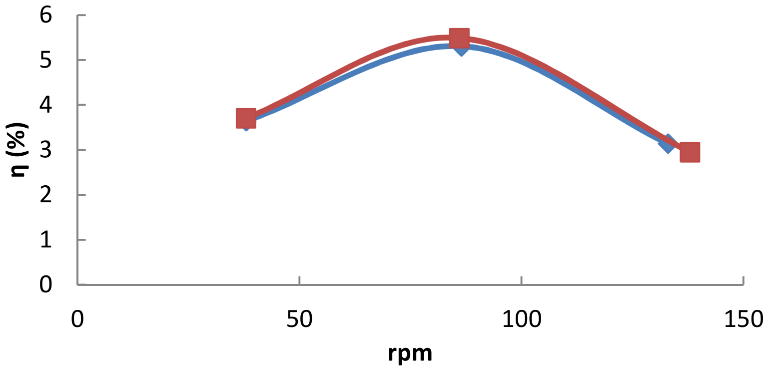

Fig 68: Efficiencies vs rpm for θ = 60° and v_f = 6 m/s, ♦ smooth blades, ■ structured blades

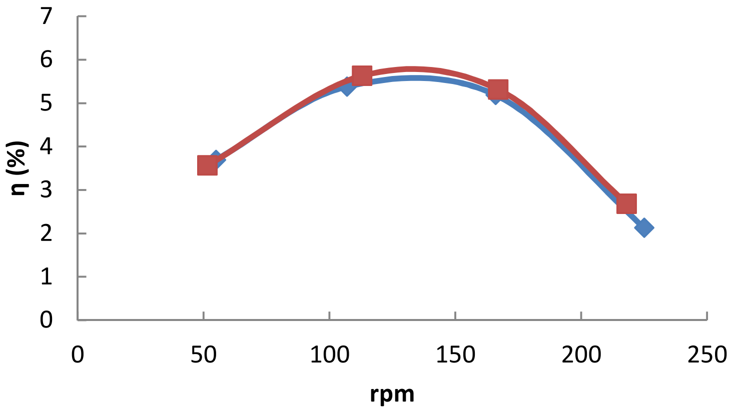

Fig 69: Efficiencies vs rpm for θ = 60° and v_f = 9 m/s, ♦ smooth blades, ■ structured blades

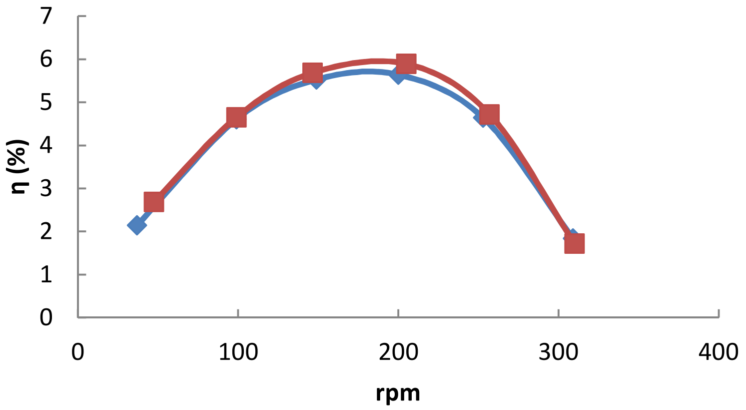

Fig 70: Efficiencies vs rpm for θ = 60° and v_f = 12 m/s, ♦ smooth blades, ■ structured blades

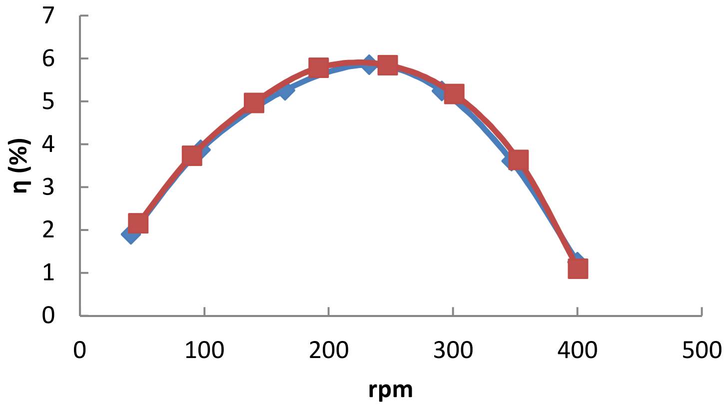

Fig 71: Efficiencies vs rpm for θ = 60° and v_f = 15 m/s, ♦ smooth blades, ■ structured blades

As shown in figures, no significant deviation, neither positive nor negative, can be observed for any flow velocity. A minor increase in the efficiency of structured blades at a flow velocity of 12 m/s lies within the uncertainty of measuring instruments. The uncertainties lie within the range of 18% to the 6% for turbine efficiencies of 3% to 6%

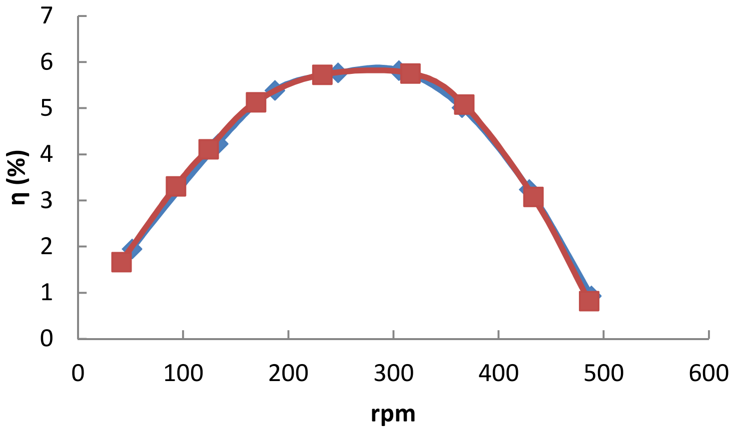

Fig 72: Efficiencies vs rpm for θ = 60° and v_f = 18 m/s, ♦ smooth blades, ■ structured blades

Fig. 73-77 shows the measured quantities and a comparison of flat and structured blades at θ = 40°. A similar kind of behavior with slight deviations lying within the uncertainty limits of the measuring devices can be seen in the following figures. However, the maximum efficiency achieved by both the turbine configurations is about 11 %, which is higher than the configurations with θ = 60°

The maximum efficiency is again delivered at an rpm of about 64% of the maximum (rpm at which the turbine is spinning without any load applied on it) possible revolution per minute. The operating point (point of maximum efficiency) remains independent of the blade incident angle as well as the surface finishing of the blades. The maximum efficiency achieved by a particular configuration seems also not be affected by the hexagonal structures or variation in the mean stream velocity. The only dependency of the efficiency in this case has been the blade incident angle θ.

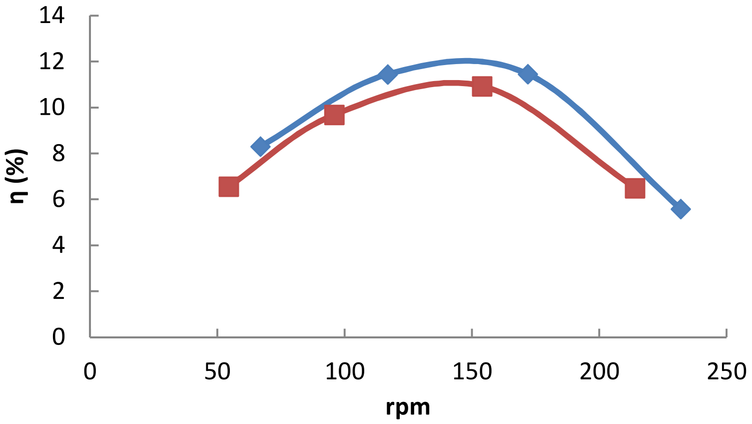

Fig 73: Efficiencies vs rpm for θ = 40° and v_f = 6 m/s, ♦ smooth blades, ■ structured blades

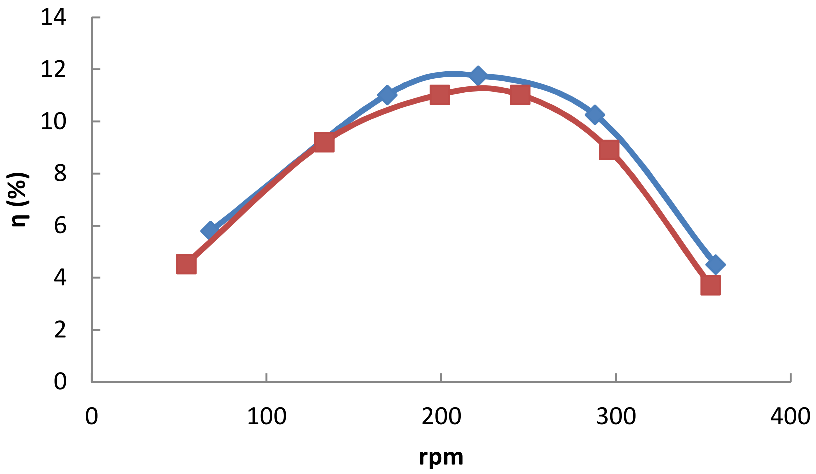

Fig 74: Efficiencies vs rpm for θ = 40° and v_f = 9 m/s, ♦ smooth blades, ■ structured blades

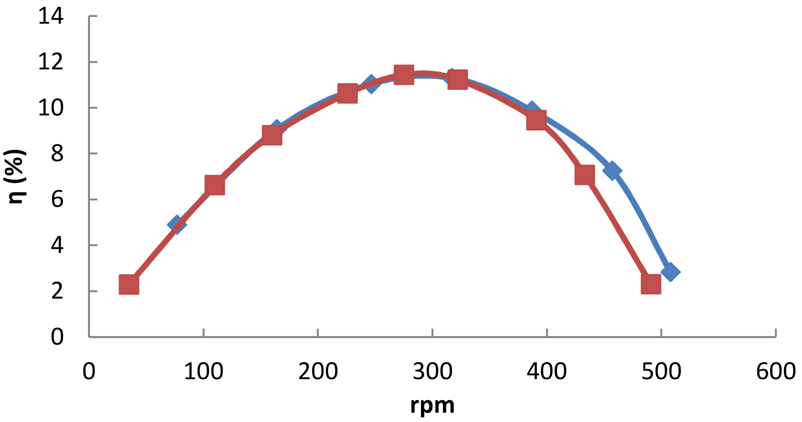

Fig 75: Efficiencies vs rpm for θ = 40° and v_f = 12 m/s, ♦ smooth blades, ■ structured blades

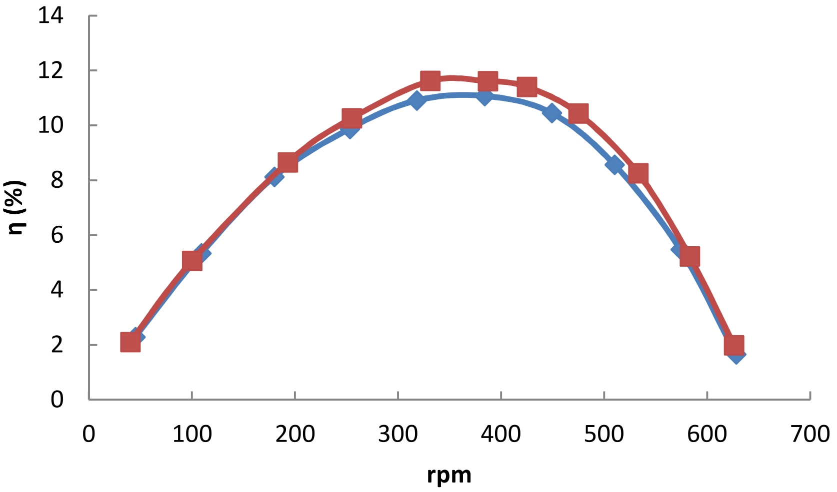

Fig 76: Efficiencies vs rpm for θ = 40° and v_f = 15 m/s, ♦ smooth blades, ■ structured blades

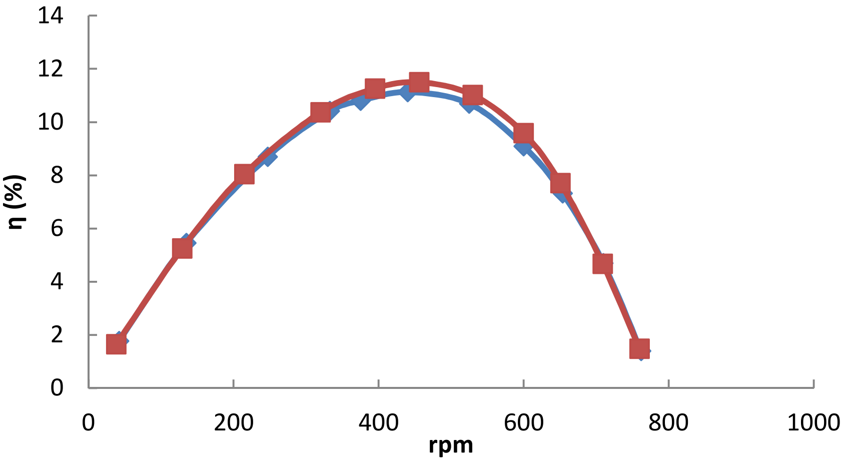

Fig 77: Efficiencies vs rpm for θ = 40° and v_f = 18 m/s, ♦ smooth blades, ■ structured blades

The results of the investigations on the configurations with θ = 20° are displayed in Fig. 78 82. A maximum efficiency of more than 20% is achieved, which is higher than both the previous configurations. However, no significant enhancement in efficiencies of the configurations with structured blades can be observed.

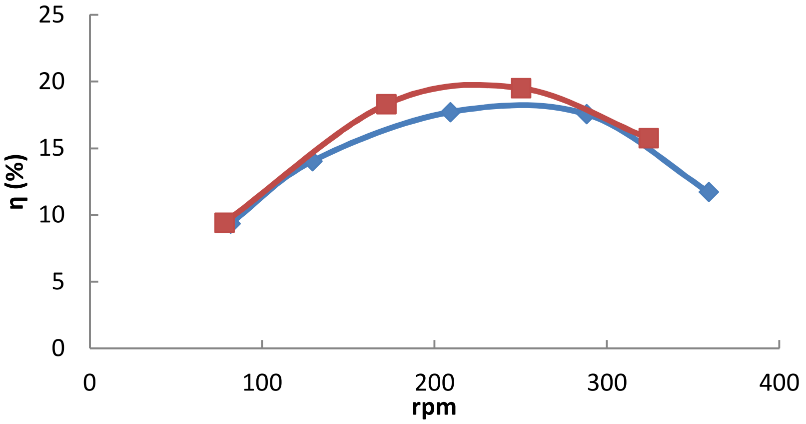

Fig 78: Efficiencies vs rpm for θ = 20° and v_f = 6 m/s, ♦ smooth blades, ■ structured blades

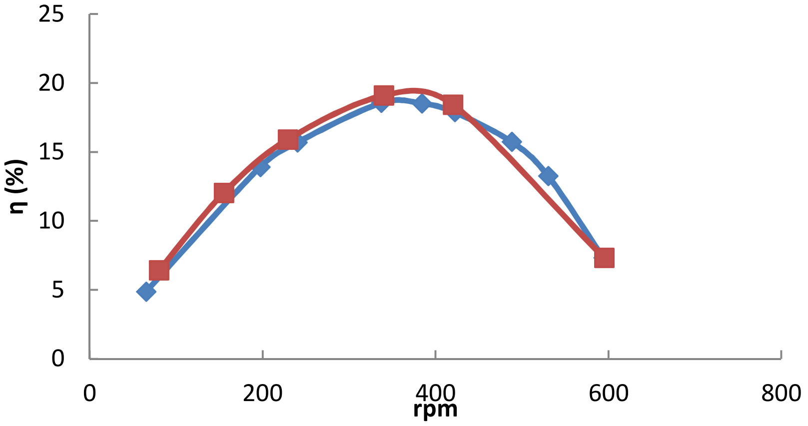

Fig 79: Efficiencies vs rpm for θ = 20° and v_f = 9 m/s, ♦ smooth blades, ■ structured blades

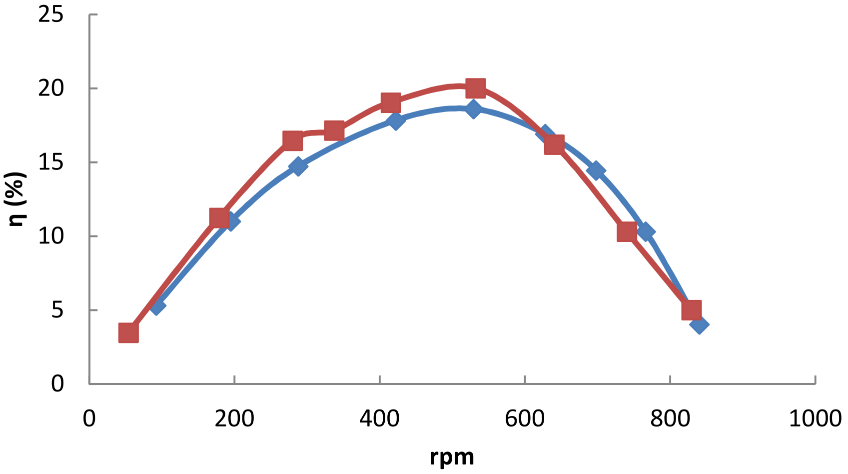

Fig 80: Efficiencies vs rpm for θ = 20° and v_f = 12 m/s, ♦ smooth blades, ■ structured blades

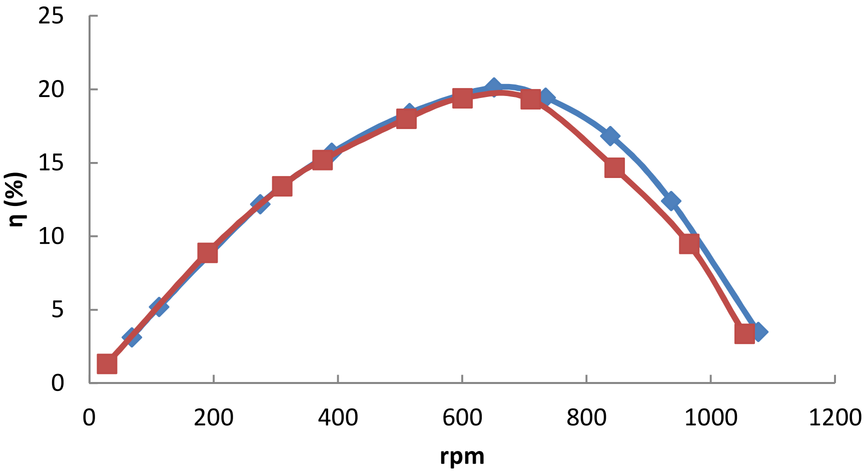

Fig 81: Efficiencies vs rpm for θ = 20° and v_f = 15 m/s, ♦ smooth blades, ■ structured blades

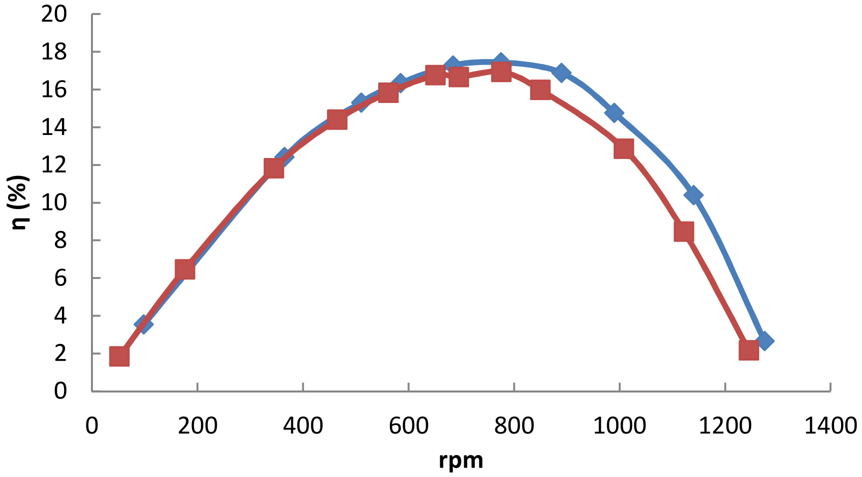

Fig 82: Efficiencies vs rpm for θ = 20° and v_f = 18 m/s, ♦ smooth blades, ■ structured blades

Finally, efficiencies of both the configurations of the turbine with θ = 10° were determined for a set of angular speeds as shown in Fig. 83-86. The behavior observed in the following figures is not much different from the last curves. The maximum efficiency achieved by these configurations is about 19% which is slightly less than that of the configurations with θ = 20°. The operation point is also shifted a bit towards right. However, the turbine with structured blades seems to be less efficient than the smooth one especially at higher flow velocities and angular speeds.

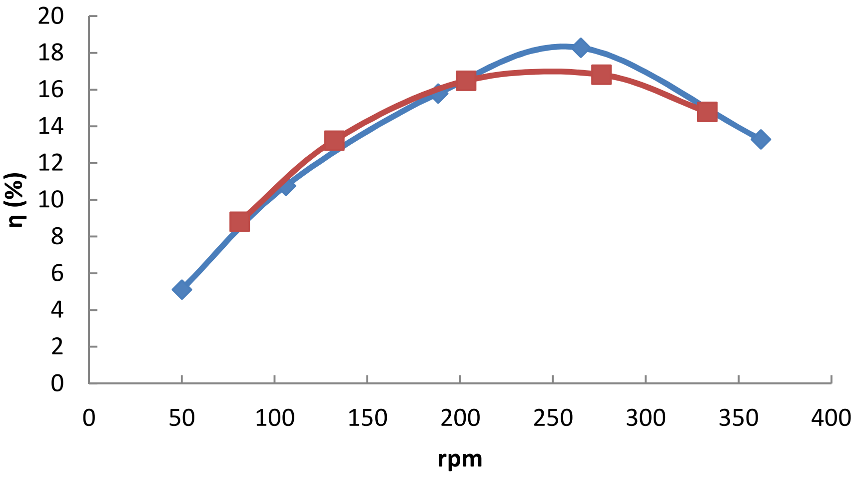

Fig 83: Efficiencies vs rpm for θ = 10° and v_f = 6 m/s, ♦ smooth blades, ■ structured blades

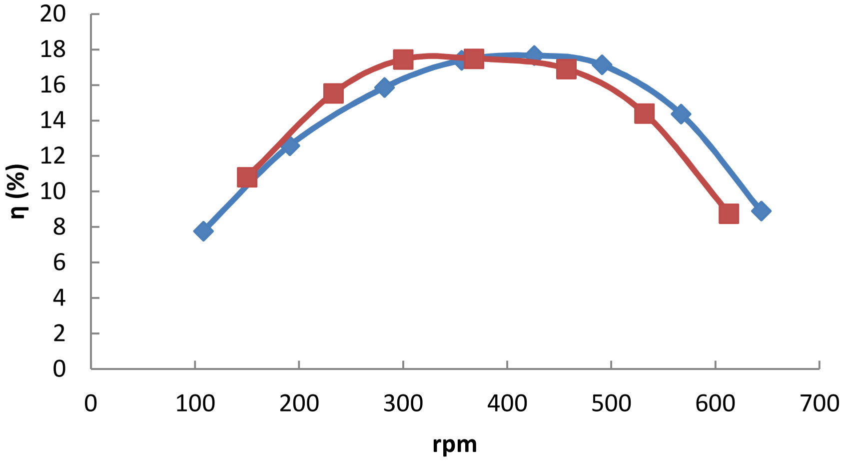

Fig 84: Efficiencies vs rpm for θ = 10° and v_f = 9 m/s, ♦ smooth blades, ■ structured blades

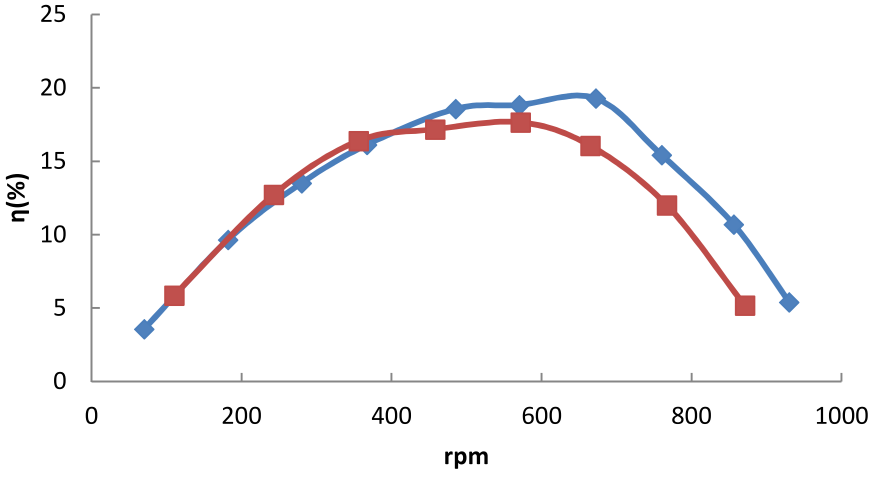

Fig 85: Efficiencies vs rpm for θ = 10° and v_f = 12 m/s, ♦ smooth blades, ■ structured blades

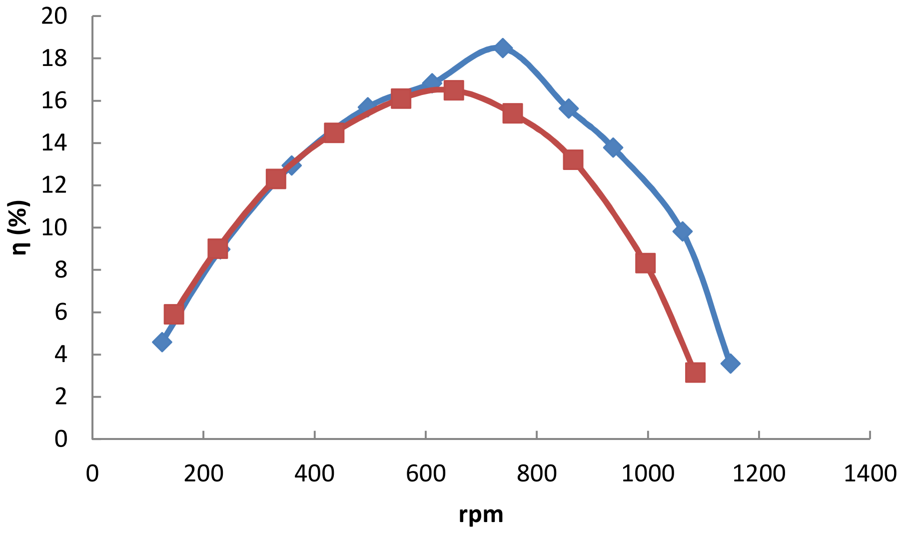

Fig 86: Efficiencies vs rpm for θ = 10° and v_f = 15 m/s, ♦ smooth blades, ■ structured blades

It can be concluded from the above results that despite having a positive effect on the drag of structured cylinders, the hexagonal structures contribute no significance in delaying the stall of turbine blades and hence the output power as well as its efficiency. The phenomenon of flow separation above a smooth surfaced airfoil has been explained by Z. Yang et al. [69]. By increasing the angle of attack of a smooth surface blade, the flow above the surface undergoes a transition from laminar to turbulent boundary layer induced by partial separation. As the turbulent boundary layer possesses higher energy and is able to withstand pressure gradients, it reattaches to the surface leaving a separation bubble behind it. By further increasing the angle of attack, the adverse pressure gradient becomes so high that the shear layer is unable to reattach to the surface of airfoil. There are mainly two ways in which the hexagonal structures could affect the flow positively. i) they delay the main separation by energizing the separated shear layer ii) they avoid large laminar separation bubble by creating turbulence in the boundary layer ahead of natural transition. Let’s consider the mechanism of the flow separation above a cylinder shortly. The flow over cylinder undergoes a laminar separation till the critical Reynolds number where the drag-crisis occurs. The hexagonal structures induce a transition by disturbing the boundary layer above the surface of a cylinder and hence shift the drag-crisis to lower Reynolds numbers (Pre-critical regime). Whereas, the flow over a smooth surfaced airfoil has already experienced a transition in flow while increasing the angle of attack. A full separation of the flow above the surface of investigated turbine blades must be taking place somewhere between θ = 10°-20° as the maximum efficiencies start falling from θ = 10°. It seems that the hexagonal structures are unable to energize the separated shear layer to an extent that it reattaches or avoid any larger laminar separation bubble which arises during the natural transition of the flow. Secondly, the size of hexagonal structures is much larger than the thickness of the boundary layer which possibly causes an additional drag, affecting the flow over blade badly. In any case, these structures or at least the current size of these structures have proven not be useful in enhancing the efficiency of the turbine.

7. Conclusions & Future work

7.1 Conclusions

Experiments were performed to investigate the flow over structured surfaces (structured cylinders and plates) taking into consideration the aerodynamic quantities like pressure drag, momentum thickness, shear stress and moments in the wake regions. Investigations of the flow over patterned or structured cylinders with patterns of $k/D = 1.98 \times 10^{-2}$ were conducted for Reynolds numbers ranging from 3.14×10^4 to 2.77×10^5. The drag coefficient of the cylinder with patterns pressed outwards at 90° to the flow was found to be the lowest of all, i.e. 0.65 times of S and remains nearly unchanged for a wider range of Reynolds numbers, whereas the drag coefficient of the configuration I0 has a value very close to the one of smooth cylinder. It was shown with the help of velocity profiles in the wake region and flow visualization techniques that the boundary layer separation is much more delayed for patterned cylinder with the lowest drag coefficient and occurs between 110° and 115°. A hexagonal bump (outwardly curved structure) disturbs the incoming flow in such a way that an early partial separation takes place. This partial separation initiates instability along the separating shear layer and increase the turbulent intensity of the flow near the surface. The flow reattaches to the surface with higher momentum and leaves a separation bubble behind it. The reattached flow is able to overcome the adverse pressure gradient delaying the main separation significantly. On the other hand, the configurations with patterns pressed inwards possess a drag coefficient closer to the one of smooth cylinder. The higher drag coefficient suggests that the separation is not that much delayed as in case of the outwardly curved structures. Oil flow patterns and velocity profiles above the surface confirmed the earlier separation of flow. Hence, it is evident that inwardly curved structures do not behave exactly in a way as the dimples do, although they resemble dimples much more in form and shape than the above mentioned hexagonal bumps. Furthermore, it was revealed that the separation of flow over patterned cylinders cannot be specified by a single line at a particular angle, but a wave with its crests and troughs indicating the points of main separations along the length of the cylinder. On the basis of these results, it can confidently be established that the delayed boundary layer separation induced by a separation bubble is mainly responsible for the drag reduction of patterned cylinders.

In the second phase of the dissertation, investigations are performed on patterned or structured plates by placing them in a flow of mean velocities ranging from 19 m/s to 28 m/s. The investigations included measuring local and global drag of the structured plates, Momentum thicknesses at front and rear of the plates and pressure distribution over individual hexagonal structures. Clauser-chart and oil film interferometry were used to determine the shear stress coefficients. It has been confirmed that Clauser-chart produces artificially high values of shear stress coefficients. The values obtained by the Clauser-chart method are about 13% higher than the values produced by oil film interferometry. On the other hand, Clauser-chart method failed to predict the skin drag coefficients above individual hexagonal structures due to the presence of high pressure gradients. Measurements using both the techniques revealed that the skin drag coefficient behind the structured plates drops significantly. The maximum reduction in shear stress coefficient was recorded for I0, which amounts to about 19%. Besides that, an increase in momentum thickness, which is a measure of total drag, is observed. Global drag C_F coefficient was obtained by using the law of conservation of momentum. The largest increase in drag coefficient is produced by the configurations with inwardly curved structures. Shear stress measurements using oil film interferometry and pressure measurements over individual hexagonal structures were also performed to comprehend the phenomenon responsible for a dramatic increase in drag of the structured plates. Shear stress coefficients were found to be very high at the rising edges of inwardly curved structures, whereas nearly no signs of shear stress for I0 and very small value for I90 were recorded at the middle of the hexagons. The growth of fringe patterns in multi directions indicates the presence of multidimensional circulating structures. Circulation regions forming a sphere similar to the arrangement of slices in an orange are thought to form the dark circular bands on the downstream (rising) edge of the hexagon of I0 and falling (leading) edge of I90. Outwardly curved structures show a very high shear stress coefficient at the rising (leading) edge and an extremely low or nearly zero at the falling (downstream) edge. Pressure measurements also exhibit some expected results i.e. high pressure region in the middle of inwardly curved structures and a very low pressure region at the middle of outwardly curved structures. The uneven pressure distribution on the wavy surface contributes to the pressure drag, which in turn together with increased shear stresses is responsible for the dramatic increase in the drag of the inwardly curved structured plate.

Finally, a wind turbine made of structured blades was tested and the results were compared with the turbine made of smooth surface blades under similar conditions. No significant change in the efficiency of the turbine made of structured blade was observed.

7.2 Future work

It has been proven that the shear stress behind a structured plate is significantly reduced at the expanse of global drag of the plate. Based on the current findings it can be hypothesized that larger hexagonal structures will further increase the drag of the structured plates by thickening the turbulent boundary layers above them. Additionally, the structures having a size larger than the thickness of the boundary layer would cause extra pressure drag. The influence of the hexagonal structures on form drag is much similar to that of dimples, which is, that the main separation of flow is delayed resulting in a lower drag coefficient at desired Reynolds numbers. Due to certain limitations, the effect of the variation in size of the hexagonal structures has not been addressed in the dissertation. It would be interesting to investigate smaller hexagonal structures for cylinders as well as plates. Choosing smaller hexagonal structures, smaller in depth and size is crucial. As the k/D ratio of a structured cylinder can be changed by varying the diameter of the cylinder but this will also shift the investigated Reynolds number range to an undesired region, i.e. post critical region of a smooth cylinder where drag-crisis is not visible anymore. A smaller depth and size of the hexagons must be chosen mainly due to two reasons. i) the investigated Reynolds number region include the critical regime of a smooth cylinder, ii) the cylinders do not lose their circular form. Structured plates with smaller hexagonal structures can either be realized by developing a new matrix (mold, in which the patterns are created on plates), or by prototyping. The size of the structures can determined by reviewing the results of investigations on present sizes and the sizes of other structures used as passive flow control methods in literature. Smaller hexagonal structures, with sizes comparable to the thickness of the boundary layer above the surface of the blade, are much likely to bring a positive change in the aerodynamic properties of an airfoil or a blade and hence in the efficiency of a wind turbine.

Another aspect, which needs to be addressed, is their influence on pipe flow. The investigations on structured plates were performed in a zero pressure gradient. Based on the results presented in this dissertation, it cannot be deduced how these structures and their orientation would influence the turbulent boundary layer quantities like shear stress coefficients, drag coefficients, displacement- und momentum thicknesses under a pressure gradient such as in a pipe. A large pipe flow facility is present at the institute of aerodynamics and fluid dynamics. Velocities up to 60 m/s can be achieved through the facility. A small portion, somewhere at the midway of the pipe, where the flow has reached its fully developed equilibrium state, can be replaced by the structured pipes made of structured plates to investigate the effect of hexagonal structures on the main pipe flow.

8. Literature

[1] J.M. Davies, ‘The Aerodynamics of Golf balls’, *Journal of Applied Physics*, Vol. 20, Nr. 9, 1949, pp 822-828

[2] S. Jeon, J. Choi, W. Pyung, J. Choi†, J. Park, ‘Active control of flow over a sphere for drag reduction at a subcritical Reynolds number,’ *J. Fluid Mech*, Vol. 517, 2004, pp 113-129

[3] Y. Triyogi, D. Suprayogi, E. Spirda, ‘Reducing the drag on a circular cylinder by upstream installation of an I-type bluff body as passive control,’*Proc. IMechE J. Mechanical Engineering Science,* Vol. 223, 2009, pp- 2291-2296.

[4] J. Panga, K, Choi, Turbulent drag reduction by Lorentz force oscillation, *PHYSICS OF FLUIDS*, Vol. 16, Nr. 5, 2004, pp 35-38

[5] S. Malekzadeh, A. Sohankar, ‘Reduction of fluid forces and heat transfer on a square cylinder in a laminar flow regime using a control plate’, Int. Journal of Heat and Fluid Flow, Vol. 34, 2012, pp 15-27.

[6] I.Korkischko, J.R. Meneghini, ‘Supression of vortex-induced vibration using moving surface boundary-layer control.’, *J. Fluid and Structures*, Vol. 34, 2012, pp 259-270.

[7] E. Achenbach, ‘Influence of Surface Roughness on the Cross-Flow around a Circular Cylinder, ’ *J. Fluid Mech*. Vol. 46, Pt. 2, 1971, pp. 321-335

[8] P. W. Bearman and J. K. Harvey, ‘Control of Circular Cylinder Flow by the Use of Dimples,’ *AIAA Journal*, Vol. 31, No. 10, 1993, pp- 1753-1756

[9] Y. Yamagishi, M. Oki, ‘Effect of the Number of Grooves on Flow Characteristics around a Circular Cylinder with Triangular Grooves,’ *Journal of Visualization*, Vol. 8, No. 1, 2005, pp 57-64

[10] V. Oruc, ‘Passive control of flow structures around a circular cylinder by using screen,’ *Journal of fluid structures*, 2012, Vol. 33, 229-242

[11] Mashud, Islam, ‚Reduction of drag force of a cylinder by attaching cylindrical rings,‘’13th Asian Congress of Fluid Mechanics, 2010

[12] Kramer, M. O., "Boundary layer stabilization by distributed damping' *J. Aerospace Sci*. Vol. 24, 1957,pp 459

[13] Squire, L.C. ; Savill, A. (1987), 'Some experiences of riblets at transonic speeds"Proc. of the Int. Conf. on turbulent drag reduction by passive means Royal Aeroneutical Society, London', 392—407

[14] Boiko, Kornilov, ‘Flat plate turbulent boundary layer control using vertical LEBU’s’ *Thermophysics and Aeromechanics*, Vol 16, Nr 4, 2009

[15] C.Lee, G. Hong, Q.P. Ha, S.G. Mallinson, ‘A piezoelectrically actuated micro synthetic jet for active flow control’, Sensors and Actuators, Vol. 108, 2003, pp 168-174

[16] M. Ito, S. Tamano, K. Yokota, S. Taniguschi, ‘Drag reduction in a turbulent boundary layer on a flexible sheet undergoing a spanwise traveling wave motion’, ‘*Journal of Turbulence*, Vol. 7, 2006

[17] D.P. Hwang, ‘Skin-friction reduction by a micro blowing technique’, ‘AIAA Journal, Vol. 36, N0. 3, 1997, pp 480-481

[18] C.M. Ho, Y.c. Tai, ‘Micro-electro-mechanical-systems and fluid flows’, *Annu. Rev. Fluid Mechanics*, Vol. 30, 1998, pp 579-601

[19] K. Kim, H.Sung, ‘Effects of periodic blowingfrom spanwise slot on a turbulent boundary layer’, *AIAA Journal*, Vol. 41, No. 10, 2003, pp-1916-1924

[20] A.E. Alving, P. Freeberg, ‘The effect of riblets on sails. In: Experiments in Fluids 19 1995, S. 397—404

[21] M. Keck, ‘Experimentelle Untersuchungen zur Wirksamkeit von Riblets in verzögerten Grenzschichten‘, Doctoral Thesis, 2008

[22] C, Wüst, ‚Dellen im Dach‘ *Der Spiegel* 14, S. 170-172; 2004

[23] Lienhardt, H., Breuer, M., Köcksoy C, ‘Drag reduction by dimples? – a complementary experimental / numerical investigation’ *Int. J. Heat and Fluid Flow*, 2008

[24] F. H. Clauser, 'Turbulent boundary layers in adverse pressure gradients', *Journal of Aeronautical Sciences* **21**, 1955, pp 91–108.

[25] E. Achenbach, ‘The Effects of Surface Roughness and Tunnel Blockage on the Flow Past Spheres,’ *J. Fluid Mech*, Vol. 65, Pt. 1, 1974, pp. 113-125

[26] E. Achenbach, ‘Experiments on the flow past spheres at very high Reynolds numbers,’ *J. Fluid Mech*. Vol. 54, 1972, 565-575

[27] J. Choi, W. Jeon, and H. Choi, ‘ Mechanism of drag reduction by dimples on a sphere,’ *Physics of Fluids* 18, 041702, 2006

[28] C. Wieselberger, ‘Neuere Feststellungen über die Gesetze des Flüssigkeits- und Luftwiderstands ,‘ Physikalische Zeitschrift, Vol. 22, 1921, pp. 321-328

[29] P.W. Bearman, J.K. Harvey,’ Golf ball aerodynamics,’ *Aeronaut Quarterly* 27, 1976, pp-112-122

[30] S. Takayama, K. Aoki, ‘Flow Characteristics around a Rotating Grooved Circular Cylinder with Grooved of Different Depths,’ *Journal of Visualization*, Vol. 8, No. 4, 2005, pp- 295-303

[31] P. W. Bearman and J. K. Harvey, ‘Control of Circular Cylinder Flow by the Use of Dimples,’ *AIAA Journal*, Vol. 31, No. 10, 1993, pp- 1753-1756

[32] K. Son, J. Choi, W. Jeon, H. Choi, ‘Mechanism of drag reduction by a surface trip wire on a sphere,’ J. Fluid Mechanics, Vol. 672, 2011, pp-411-427

[33] M.J. Walsh, L.M. Weinstein, ‘Drag and Heat Transfer on Surfaces with Small Longitudinal Fins’, AIAA Paper 78-1161 (1978)

[34] Reif, W.E. ; Dinkelacker, A.: Hydrodynamics of the Squamation in fast swimming sharks. In: Neues Jahrbuch für Geologie und Paläontologie, Abhandlungen, Schweizerbartsch Verlagsbuchhandlung, Stuttgart Vol. 164, 1982, S. 184—187

[35] L.C. Squire, A. Savill, 'Some experiences of riblets at transonic speeds"Proc. of the Int. Conf. on turbulent drag reduction by passive means Royal Aeroneutical Society, London', 1987, pp 392—407.

[36] D.W. Bechert, M.W. Bruse, 'Experiments on drag-reducing surfaces and their optimization with an adjustable geometry', *J. Fluid Mech* Vol. **338**,1997, pp 59—87.

[37] W. Haage, D.W. Bechert, M. Bruse, ‘Yaw Angle Effects on Optimized Riblets’, In: European Drag Reduction Conference. Potsdam, 2000

[38] J.R. Debisschop, F. Nieuwstadt, 'Turbulent Boundary Layer in an Adverse Pressure Gradient: Effectiveness of Riblets', *AIAA* Vol. **34**, No. 5,1996, pp 932—937.

[39] S. Sundaram, P. Viswanath, 'Viscous Drag Reduction Using Riblets on NACA 0012 Airfoil to Moderate Incidence', *AIAA Journal* Vol. **34, No.** 4, 1996

[40] N.K. Burgess, M.M. Oliveira, P.M. Ligrani ‘Nusselt number behavior on deep dimpled surfaces within a channel’, J. Heat Transfer, Vol. 125, 2003, pp 11–18.

[41] V.V. Alekseev, I.A. Gachechiladze, G.I. Kiknadze, V.G. Oleinikov, 1998. Tornado-like energy transfer on three-dimensional concavities of reliefs-structure of self-organizing flow, their visualisation, and surface streamlining mechanisms. In: Transactions of the 2nd Russian Nat. Conf. of Heat Transfer, Heat Transfer Intensification Radiation and Complex Heat Transfer, vol. 6. Publishing House of Moscow Energy Institute (MEI), Moscow, pp. 33–42.

[42] V.I. Therekhov, S.V. Kalinina, ‘Flow structure and heat transfer on a surface with a unit hole depression’ J. Eng. Thermophys. Vol. 5, 1995, S. 11-34

[43] G. Kiknadze, I.A. Gachechiladze, V.G. Oleinikov, ‘Method and apparatus of controlling the boundary or wall layer of continous medium’, USPAT No. 6, 119987, 2000

[44] A.B. Shchukin, A.P. Kozlov, Y. Chudnovskii, R.S. Agachev, ‘Intensification of heat exchange by spherical depressions’, a survey; Applied Energy: Russian Journal of

Fuel, Power and Heat Systems 36/3, S. 45-62; 1998

[45] Yu-Lashkov, N.V. Samoilove N.V, ‘On the viscous drag of a plate with spherical recesses’ Fluid dynamics, 37/2, S. 231-236; 2002

[46] M.K. Chyu, H. Ding, J.P. Downs, F.O. Soechting, ‘Concavity enhancements heat transfer in an internal cooling passage’, ASME 97-GT-437; 1997

[47] H.K. Moon, T. O'Connel, B. Glezer, ‘Channel height effect on heat transfer and friction in a dimpled passage’ *Journal of Engineering for Gas Turbines and Power* Vol. 122, 2000S. 307-313

[48] G.I. Mahmood, M. Hill, D. Nelson, P.M. Ligrani, H.K. Moon, B. Gelzer, ‘Local heat transfer and flow structure on and above a dimpled surface in a channel’ ASME J. Turbomachinery Vol. 123, 2001, S. 115-123

[49] P.M. Ligrani, J.L. Harrison, G.I. Mahmod, C.M. Clayton, D.L. Nelson, ‘Flow structure and local nusselt number variations in a channel with dimples and protrusions on opposite walls’ *Int. J. Heat and Mass Transfer* Vol. 44, 2001, S. 4413-4425

[50] R.S. Bunker, K.F. Donnellan, ‘Heat transfer and friction factors for flows inside circular tubes with concavity surfaces’ ASME Paper GT 2003-38053, 2002

[51] M.E. McCormick, R. Bhattacharyya, ‘Drag reduction on a submersible hull by electrolysis’ *Nav. Eng. J.* 85, 1973, pp 11-16

[52] A. A. Fontaine, S. Deutsch, ‘The influence of the type of gas on the reduction of skin friction drag’, *Experiments in Fluids* Vol. 13, 1992, pp 128-136

[53] Y. Kodama, A. Kakugawa, T. Takahashi, H. Kawashima, ‘Experimental study on microbubbles and their applicability to ships for skin friction reduction’, *International Journal of Heat and Fluid Flow*, Vol. 21, 2000, pp 582-588,

[54] Y. Murai, H. Fukuda, Y. Oishi, Y. Kodama, F. Yamamoto, ‘Skin friction reduction by large air bubbles in a horizontal channel flow’, *International Journal of Multiphase Flow*, Vol. 33, Issue 2, 2007, pp 147–163

[55] J.Pang, K.Choi, ‘Turbulent drag reduction by Lorentz force oscillation’, Physics of Fluids, Vol. 16, No 5, 2004, pp 35-38

[56] V. Kornilov, ‘Flate plate turbulent boundary layer control using vertical LEBU’s’, Presentation at BTU Cottbus, 2011

[57] L.H. Tanner, L.G. Blows, 'A study of the motion of oil films on the surfaces in air flow, with application to the measurement of skin friction', *Journal of Physics E: Scientific Instruments* Vol. **9**, 1976, pp 194–202.

[58] L.S.G. Kovasasznay, V. Kibens, R.F. Blackwelder, .: Large-scale motion in the

intermittent region of a turbulent boundary layer. In: J. Fluid Mech. Vol. 41, 1970, pp 283-325

[59] E.S. Zanoun, H. Nagib, 'Evaluating the law of the wall in two-dimensional fully developed turbulent channel flows', *Physics of Fluids* Vol. **15**, 2003, pp 3079–3089.

[60] S.J. Kline, W.C. Reynolds, F.A. Schraub, P.W. Runstadler ‘The structure of turbulent boundary layers’. *J Fluid Mech* Vol. 30, 1967, pp741–773

[61] R. Blackwelder, J. Haritonidis, ‘Scaling of the bursting frequency in turbulent boundary layers’. *J Fluid Mech* Vol. 132, 1983, pp 87–103

[62] P. Spalart, ‘Direct simulation of a turbulent boundary layer up to Re_h = 1410. *J Fluid Mech* Vol. 187, 1988, pp 61–98

[63] T. Wei, R. Schmidt, P. McMurtry, ‘Comment on the Clauser chart method for determining the friction velocity’. *Exp in Fluids* Vol. 38, 2005, pp 695–699

[64] L.C. Squire, ‘The motion of a thin oil sheet under the steady boundary layer on a body’, *Journal of Fluid Mechanics*, Vol. 11, 1961, pp 161–179.

[65] H.H. Fernholz, G.S. Janke, 'New developments and applications of skin-friction measuring techniques', *Meas Sci Technol* **7**, 1996, pp1396–1409.

[66] H.C.H. Ng, I. Marusic, J.P. Monty, N. Hutchins, M.S. Chong, ‘Oil film Interferometry in high Reynolds numbers turbulent boundary layers’, 16th Australian Fluid mechanics Conference, 2007

[67] R. Örlü, H.M. Franson Alfredsson, , On near wall measurements of wall bounded flows—The necessity of an accurate determination of the wallposition’, Progress in Aerospace Sciences 46, 2010, pp 353-387,

[68] A. Sigalini, R. Örlü, , P. Henrik Alfredsson, ‚Uncertainity Analysis of von Ka’rma’n constant’, *Exp Fluids 54*, 2013, 1460

[69] Z. Yang, Fred L. Haan, Hu Hui, H. Ma, , An Experimental Investigation on the Flow Separation on a Low-Reynolds-Number Airfoil’, 45th AIAA Aerospace Sciences Meeting and Exhibit, 2007

[70] M.M. Zdravkovich, ‘Flow Around Circular Cylinders’, Oxford Press Volume 2, 2003

[71] H. Schlichting, K.Gersten, ‘Boundary layer theory’, Springer Press, Volume 8, 2003

[72] J. F. Douglas, J. M. Gasiorik, J. A. Swaffield, ‘Fluid Mechanics’, Oxford University Press, Fourth Edition, 2000

[73] J. M. Östurlund, A V Johansson, H M Nagib, M H Hites, ‘A note on the overlap region in turbulent boundary layers’, Phys. Fluids 12, Vol 1, 2000

[74] D J Monson, G GMateer, F R Menter, ‘Boundary layer transition and global skin friction measurements with an oil fringe imaging technique’ , Paper No. 932550, SAE Aerotech, NASA Ames Research Center, 1993